ACS NANO

www.acsnano.org

REVIEW

Chemiresistive Hydrogen Sensors: Fundamentals, Recent Advances, and Challenges

Won-Tae Koo, Hee-Jin Cho, Dong-Ha Kim, Yoon Hwa Kim, Hamin Shin, Reginald M. Penner,* and Il-Doo Kim*

Cite This: *ACS Nano* 2020, 14, 14284−14322

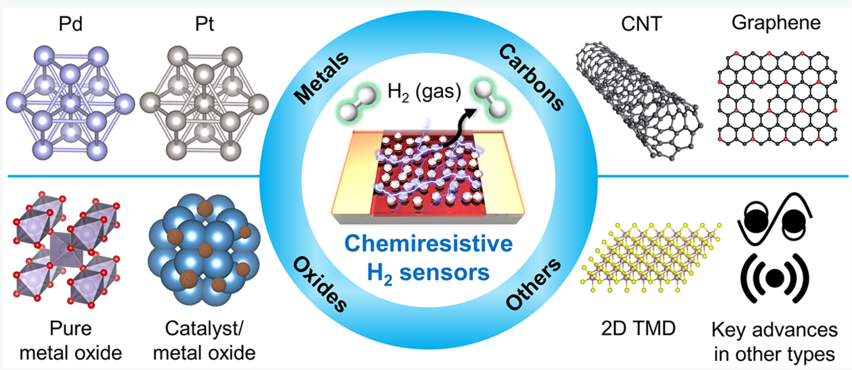

ABSTRACT: Hydrogen (H_2) is one of the next-generation energy sources because it is abundant in nature and has a high combustion efficiency that produces environmentally benign products (H_2O). However, H_2/air mixtures are explosive at H_2 concentrations above 4%, thus any leakage of H_2 must be rapidly and reliably detected at much lower concentrations to ensure safety. Among the various types of H_2 sensors, chemiresistive sensors are one of the most promising sensing systems due to their simplicity and low cost. This review highlights the advances in H_2 chemiresistors, including metal-, semiconducting metal oxide-, carbon-based materials, and other materials. The underlying sensing mechanisms for different types of materials are discussed, and the correlation of sensing performances with nanostructures, surface chemistry, and electronic properties is presented. In addition, the discussion of each material emphasizes key advances and strategies to develop superior H_2 sensors. Furthermore, recent key advances in other types of H_2 sensors are briefly discussed. Finally, the review concludes with a brief outlook, perspective, and future directions.

KEYWORDS: *hydrogen, sensors, nanomaterials, palladium, platinum, metal oxides, carbon nanotubes, graphene, transition dichalcogenides, two-dimensional materials*

Hydrogen gas (H_2) has been regarded as one of the promising next-generation energy sources because H_2 is abundant in nature and its combustion reaction only produces water (H_2O) as a byproduct.[1−3] Therefore, with the depletion of fossil fuels, the field of H_2-powered fuel cells has emerged rapidly.[4,5] However, H_2 is not only a flammable gas with a lower flammability limit of 4%, but it is also colorless, odorless, and buoyant in air. These properties require that any leakage of H_2 must be detected as quickly as possible for safety. Therefore, H_2 sensors are needed in various fields wherever it is used, such as hydrogen fuel cells, H_2 storage systems, and infrastructure/industry having or using H_2.[6] The United States Department of Energy (DOE) has set targets for H_2 sensors, in terms of concentration range (0.1−10%), operating temperature (−30 to 80 °C), response time (<1.0 s), gas environment (ambient air; 10−98% humidity), and

Received: June 26, 2020
Accepted: October 7, 2020
Published: October 30, 2020

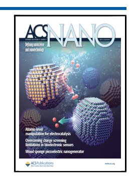

https://dx.doi.org/10.1021/acsnano.0c05307
ACS Nano 2020, 14, 14284−14322

lifetime (>10 years).[7] In addition to these metrics, H_2 sensors should be inexpensive (<$40 per unit), miniaturized, and power-efficient, to maximize their effectiveness in various applications where H_2 is used. Up to now, there have been huge efforts to develop high-performance and efficient H_2 sensors,[8] however, it is extremely challenging to meet the target metrics.

In general, the operation of H_2 sensors relies upon H_2 reactions with sensing materials. These reactions are transduced to produce a sensing signal using optical, electrochemical, mechanical, or electrical measurements.[8−11] Among them, both electrochemical and chemiresistive H_2 sensors are commercially available and regarded as a current state-of-the-art H_2 sensor technology.[12] Electrochemical H_2 sensors are operated by the transduction of redox reactions of H_2 on sensors into electrical signals.[9] Electrochemical sensors display sensitive and selective H_2 sensing properties with low detection limits, but they are highly susceptible to ambient conditions (oxygen and humidity levels) and have rather complicated systems that require high fabrication costs. On the other hand, chemiresistive sensors, which are operated by the transduction of chemical reactions into electrical signals (resistances or conductances), offer several benefits, such as efficient sensing performances, low-cost fabrication, and portable applications.[10,13,14] In particular, the detection of resistance (or conductance) changes in sensors can be efficiently interfaced with electronic readouts with minimal processing, while other transduction mechanisms require more complex signal processing.

Because of these advantages, chemiresistive H_2 sensor technology and performance have dramatically advanced in recent years. Palladium (Pd)-based resistor-type sensors are widely regarded as the current state-of-the-art H_2 sensing systems due to their simplicity, efficient sensing properties with high selectivity, and room-temperature operation.[10] Pd can react with H_2 reversibly, even at room temperature (RT), resulting in the formation of palladium hydride (PdH_x) with a higher resistivity than Pd.[15] Thus, H_2 can be easily and efficiently sensed in real-time by tracking the resistances of Pd-based sensors at RT. However, the H_2 reactions with Pd are impeded by oxygen molecules (O_2) in air. Thus, Pd-based sensors usually show degraded performance with reduced sensitivities and sluggish sensing speeds in ambient air.[16]

Semiconducting metal oxide (SMO)-based chemiresistive sensors are also one of the promising sensor technologies,[17−20] and some SMO-based sensors have been successfully commercialized due to their high compatibility with semiconductor technologies. The SMO-based chemiresistors are mainly operated by the reaction of analytes with chemisorbed oxygen species on SMOs at elevated operating temperatures (200−400 °C).[21] The chemisorbed oxygen species, such as O^- and O_2^-, trap electrons in SMOs due to their high electron affinity, generating electron depletion layers (for n-type SMOs) or hole accumulation layers (for p-type SMOs) at the surface of SMOs.[21] Then, the reaction of H_2 with chemisorbed oxygen species produces water (H_2O) and gives electrons back to the SMOs, thereby resulting in huge resistance changes even to low levels of H_2. However, the requirement for an elevated operating temperature not only increases the power consumption of these devices, but elevated temperatures also induce reactivity for some off-target gases. In addition, vulnerability to humidity hampers the reliability of SMO-based sensors.[22,23] Thus, in spite of significant advances in both Pd- and SMO-based H_2 sensors, their performances, particularly in terms of sensing speed and stability/reliability in ambient air, have not yet demonstrated the aforementioned performance metrics for H_2 sensors.

To address these issues in H_2 sensors, various interesting strategies have been developed. The acceleration of H_2 reactions and the minimization of O_2 interference with sensing have been achieved by the fabrication of nanoscopic Pd, Pd-based bimetals, and Pd-based composites.[10,24] In addition, the rational design of heterogeneous SMOs at the nanoscale with the functionalization of catalysts has resulted in improved sensing properties for selective H_2 detection.[25] Emerging materials, such as carbon nanotubes (CNTs),[26] graphenes,[27] two-dimensional (2D) transition dichalcogenides (TMDs),[28] and so on, also exhibit an interesting and efficient H_2 sensing performance at low operating temperatures. These intriguing approaches have solved some issues in H_2 sensors and have demonstrated that chemiresistive H_2 sensors are one of the most promising H_2 sensing platforms for practical applications.

In this review, we present a comprehensive overview of underlying mechanisms, recent advances, and remaining challenges in chemiresistive H_2 sensors. In each part, we cover the different H_2 sensing mechanisms depending on sensing materials, which are categorized into metal-, semiconducting metal oxide-, and carbon-based materials, and other materials (Figure 1). Then, we highlight the recent key advances and strategies for the development of superior H_2 sensors. Various synthetic methods and interesting approaches are discussed, and the correlation of sensing performances with structures, surface modification, and chemical and electrical properties is emphasized. In addition, we briefly discuss recent significant advances in other types of H_2 sensors, including macroscopic visual sensing and plasmonic sensing. Finally, the review provides a brief summary and remaining issues of H_2 sensors and the perspectives for future research. We hope that

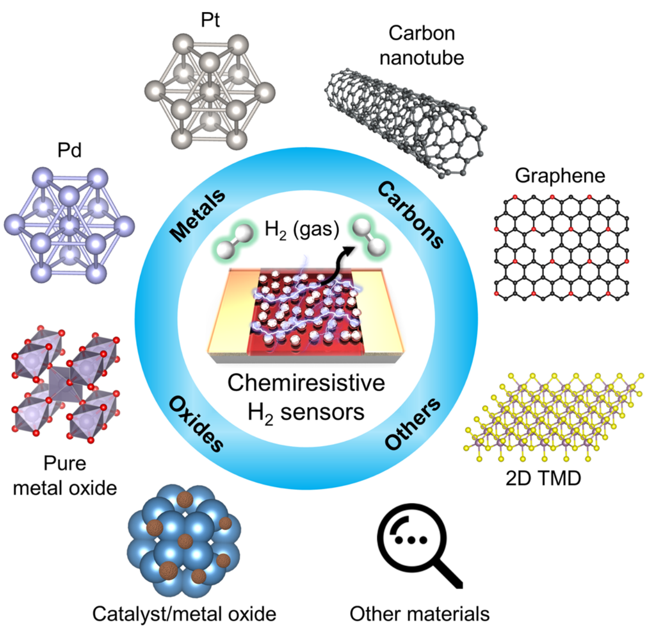

Figure 1. Schematic illustration of representative materials for chemiresistive H_2 sensors. The representative materials are categorized into metals, metal oxides, carbons, and other materials (2D TMDs: two-dimensional transition metal chalcogenides).

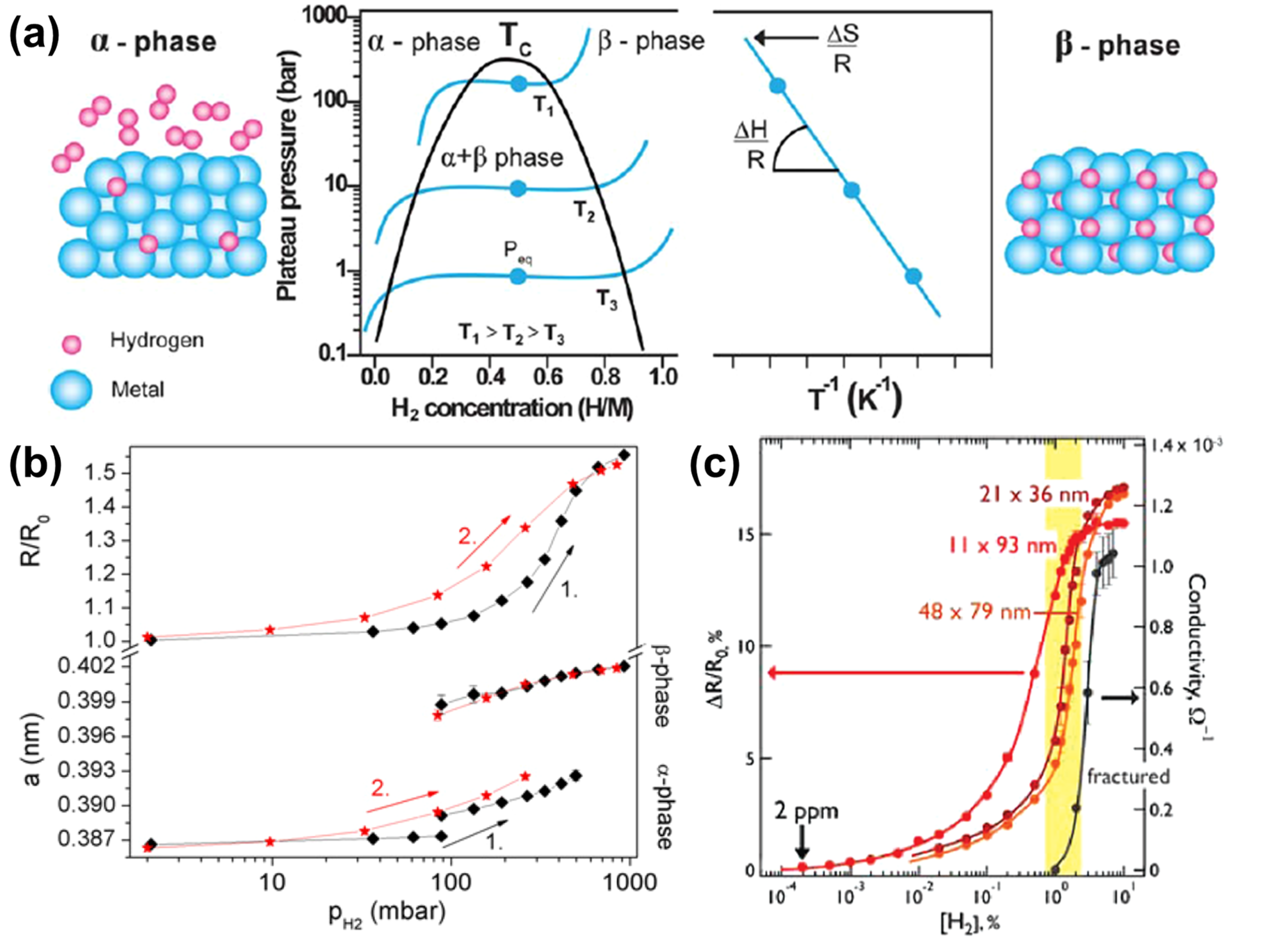

Figure 2. (a) The crystal structure of *α*-phase metal hydride (left) and *β*-phase metal hydride (right), and partial pressure−composition isotherm plot of metal hydride phase (center). By using a Van't Hoff plot, the enthalpy (Δ*H*) and entropy (Δ*S*) of metal hydride can be obtained from the slope and intercept, respectively. Reprinted with permission from ref 39. Copyright 2011 The Royal Society of Chemistry. (b) Changes of the lattice parameter and the resistances of the Pd thin films (22.5 nm) on a sapphire. The black line and dots for the first scan and the red for the second scan. Reprinted with permission from ref 42. Copyright 2011 Elsevier. (c) Response curves for Pd nanowires in response to [H_2]. Reprinted with permission from ref 41. Copyright 2009 American Chemical Society. The height and thickness of Pd nanowires are presented in the graph.

this review can guide and stimulate diverse interesting ideas that can lead to the evolution and revolution of H_2 sensors.

METAL-BASED MATERIALS

Among various metals, Pd is a particularly important resistor constiuent for H_2 sensing because the product of the reaction of Pd and H_2, PdH_x, is more resistive than Pd.[15] This reaction not only promotes selective H_2 detection at RT but also simplifies the overall sensing system. Therefore, there have been significant advances in Pd-based H_2 sensors. So far, numerous Pd-based sensors, including Pd nanostructures,[24] Pd-based bimetals,[29,30] Pd-based composites,[31] and Pd-based chemical field-effect transistors (C-FETs),[32,33] have been developed. In addition, other metallic elements, such as Pt, have recently demonstrated a H_2 sensing ability by using the surface scattering model that is attributed to the modulation of electron scattering by adsorbed gas molecules.[34,35] In this section, we discuss the detailed sensing mechanisms and the recent key advances in metallic resistors for H_2 sensors, by dividing into two sections: Pd-based materials and other metals.

Pd-Based Materials. *Basic Sensing Mechanisms for Pd-Based Sensors.* In general, the sensing mechanisms of Pd-based H_2 sensors are attributed to the formation of PdH_x. The adsorption of H_2 on the surface of Pd induces the dissociation of H_2 molecules into hydrogen atoms (eqs 1 and 2).[36] Then, the adsorbed hydrogen atoms diffuse into the interstitial octahedral sites in face-centered cubic (fcc) Pd crystals (α-PdH_x for $[H_2] \leq 1\%$, eq 3) and interrupt the transport of free electrons in Pd.[37] The further occupancy of hydrogen atoms in the octahedral interstitial sites induces internal stress in the Pd crystals, causing the huge volume expansions of the Pd lattice (β-PdH_x, eq 4) at the threshold ($[H_2] \approx 2\%$).[38,39] Therefore, exposure of the Pd sensing element to H_2 at concentrations above 1% induces the $\alpha-\beta$ phase transition ($1\% \leq [H_2] \leq 2\%$) and results in the formation of β-PdH_x ($[H_2] \geq 2\%$). It is noted that the lattice distances of Pd, α-$PdH_{0.015}$, and β-$PdH_{0.607}$ are 389.0, 389.4, and 402.5 pm, respectively.[40] In other words, α-PdH_x is related to the solid solution reaction of hydrogen atoms in fcc Pd crystals, and β-PdH_x is the formation of the rock salt structure of Pd and hydrogen (Figure 2a).[39] In addition, the formation enthalpy (the strength of Pd−H bonding) and entropy for PdH_x can be calculated by using the Van't Hoff equation (Figure 2a and eq 5),[39] where *P* is partial pressure, *H* is enthalpy, *R* is the ideal gas constant, *T* is temperature, and *S* is entropy.

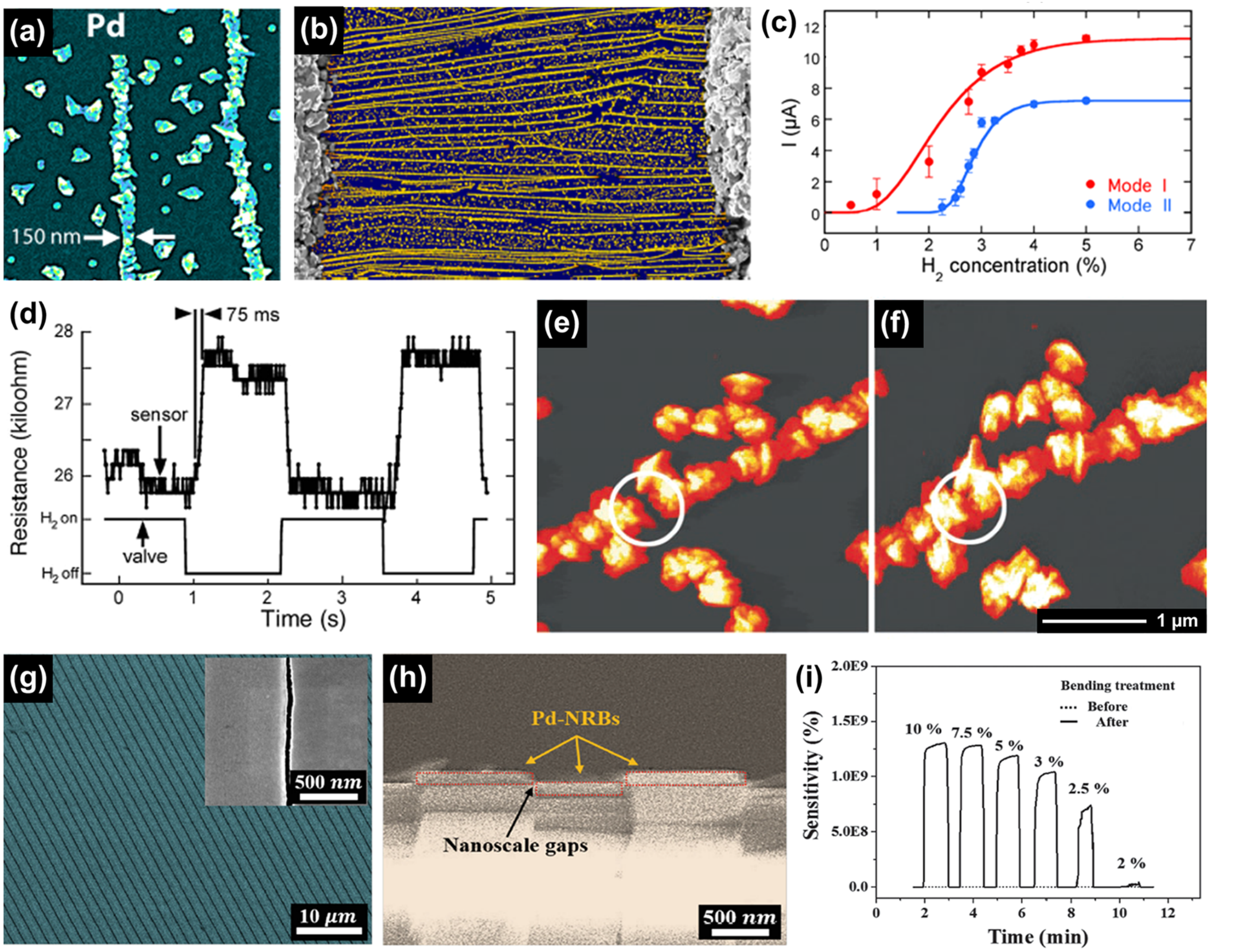

Figure 3. SEM images of (a) Pd mesowires and (b) Pd mesowire array (PMA). (c) Current values of the PMA sensors (modes 1 and 2) depending on H_2 concentrations. (d) Resistance traces of the PMA-based H_2 sensors to H_2 5%. *Ex situ* AFM analysis of the PMA (e) before and (f) after an exposure of H_2 5%. Reprinted with permission from ref 15. Copyright 2001 American Association for the Advancement of Science. (g) SEM image of the Pd nanoribbon array. Inset shows the magnified view of a nanogap. (h) Cross-sectional SEM image of Pd nanoribbon array (Pd-NRBs: Pd nanoribbons). (i) Sensitivity (response) traces of the Pd nanoribbon-based sensors in response to exposures of 2−10% of H_2. Sensitivity was defined as $\Delta I/I_0$ (%). The bending treatment was conducted to increase the nanogap effect. Reprinted with permission from ref 43. Copyright 2015 Wiley-VCH.

$$H_2(\text{gas}) \rightarrow H_2(\text{ads}) \quad (1)$$

$$H_2(\text{gas}) \rightarrow 2H(\text{ads})\ \text{on Pd} \quad (2)$$

$$\text{Pd(s)} + \text{H(ads)} \rightarrow \alpha\text{-PdH}_x\text{(s)} \quad (x \leq 0.015,\ [H_2] \leq 1\%) \quad (3)$$

$$\text{Pd(s)} + \text{H(ads)} \rightarrow \beta\text{-PdH}_x\text{(s)} \quad (x \geq 0.607,\ [H_2] \geq 2\%) \quad (4)$$

$$\ln(P_{eq}/P_0) = \Delta H/RT - \Delta S/R \quad (5)$$

In terms of resistivity, both α-PdH$_x$ and β-PdH$_x$ have a higher resistivity than Pd because the absorbed hydrogen atoms act as scattering sites impeding the movement of free electrons in PdHx crystals. Therefore, the resistivity of β-PdH$_{0.07}$, which is the maximum capacity of hydrogen in octahedral interstitial sites of Pd, is 2-fold higher than that of Pd. In general, these resistance increases of Pd upon H_2 exposures are the major sensing mechanism for most of the Pd-based H_2 sensors. The typical H_2 responses of Pd thin films and Pd nanowires are shown in Figure 2b,c, respectively.[41,42] The resistances of the sensors were increased in response to H_2 exposures, resulting in sigmoidal signal *versus* [H_2] responses. This type of Pd-based H_2 sensor enables the simple and selective detection of H_2 even at RT, however, low sensitivity and slow response and recovery speed remain as unmet challenges.

A second and related sensing mechanism exploits the volume expansion of β-PdH$_x$ relative to Pd. In sensor elements composed of Pd where gaps in the transducer have been intentionally engineered, the swelling associated with the formation of β-PdH$_x$ mechanically closes some gaps, increasing the conductivity of the Pd sensing element. The Penner group demonstrated that the volume expansion of β-PdH$_x$ induces an ultrafast H_2 sensing speed (<75 ms for over H_2 2%) by connecting break junctions in Pd nanostructures.[15] They fabricated a Pd mesowire array (PMA) using (1) the electrodeposition of Pd onto step edges on a graphite electrode and (2) the subsequent transfer onto a cyanoacrylate film. The PMA consists of numerous Pd mesowires with a dimension of ∼150 nm (Figure 3a,b). They found that the PMA-based sensors showed a resistance decrease when exposed to H_2 (Figure 3c), and some of the sensors exhibited

https://dx.doi.org/10.1021/acsnano.0c05307
ACS Nano 2020, 14, 14284−14322

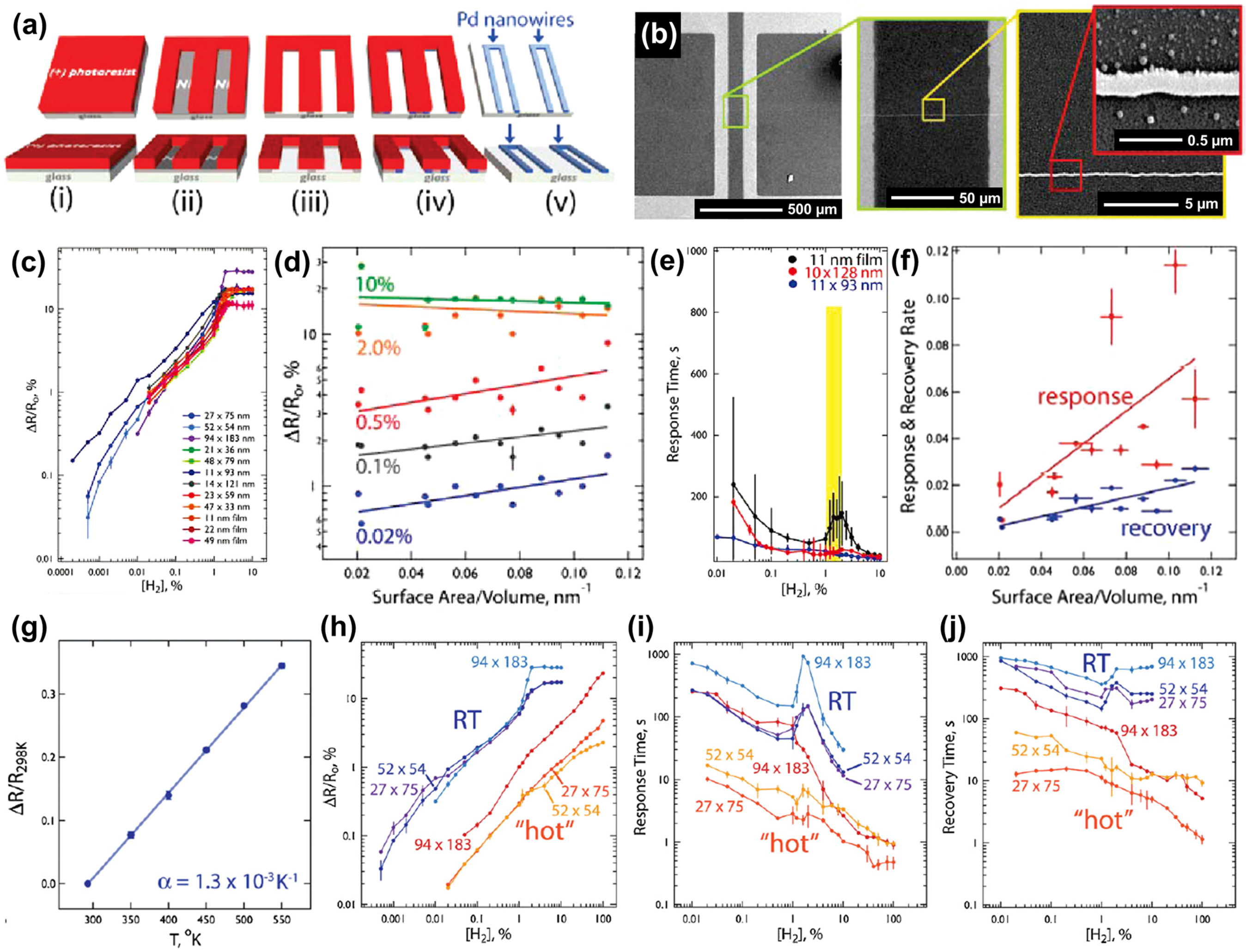

Figure 4. (a) Schematic illustration of LPNE. (b) SEM images of single Pd nanowires fabricated using the LPNE method. Sensing properties of single Pd nanowire libraries: (c) responses of various single Pd nanowires, (d) responses *versus* surface area to volume ratios, (e) response times of various single Pd nanowires, and (f) response/recovery rates *versus* surface area to volume ratios. The response/recovery rates were calculated by the plot of response/recovery time to low levels of H_2 ($[H_2] < 1.0\%$). The height and thickness of single Pd nanowires are presented in the graph. Reprinted with permission from ref 16. Copyright 2010 American Chemical Society. (g) Baseline resistances of single Pd nanowires depending on operating temperatures. Sensing performances of single Pd nanowires at RT (298 K) and "hot" (384 K): (h) response, (i) response time, and (j) recovery time. The height and thickness of single Pd nanowires are presented in the graph. Reprinted with permission from ref 54. Copyright 2010 Wiley-VCH.

on/off states depending on H_2 exposures (mode 2 in Figure 3c). Both PMA sensors were able to detect H_2 over 0.5% for mode 1 and 2% for mode 2, with ultrafast sensing speed (~75 ms to H_2 5% in N_2) (Figure 3d). The reason for the resistance decrease is attributed to the connection of the break junction in the Pd mesowires (the white circle in Figure 3e) by the volume expansion of β-PdH_x. The *ex situ* atomic force microscopy (AFM) analysis confirmed that this break junction was connected after an exposure to 5% H_2 (the white circle in Figure 3f). Inspired by this inverse sensing mechanism (resistance decrease), nanogap-controlled Pd-based sensors have been reported.[43−46] In particular, Pak *et al.*[43] developed a Pd nanoribbon array with nanoscale gaps *via* a direct metal-transfer method (Figure 3g,h). The controlled nanogap between Pd nanoribbons exhibited ultrahigh response ($\Delta I_{gas}/I_0 \approx 10^9\%$ for $[H_2] \geq 3\%$) with ultrafast sensing speed (t_{80} = 3.6 s to H_2 10%) (Figure 3i), where I_{gas} is the current of sensors when exposed to H_2, I_0 is the baseline resistance, and t_{80} is the time taken for the response increase from the baseline to 80% of the maximum response. It is noted that response times and recovery times of sensors are generally defined as a 90% rise (t_{90}) or fall (t_{10}) of signals. However, because the volume expansion of Pd is mostly contributed by the phase transition from Pd to β-PdH_x, Pd-based sensors operated by the break junction mechanism were unable to detect H_2 concentrations below 1% and often exhibited poor stability of their responses for long-term endurance due to the huge volume expansion.

Effect of Nanosize on Pd-Based H_2 Sensors. With the significant advances in nanoscience, numerous Pd nanostructures, including Pd thin films,[47,48] Pd nanowires,[16,41,49] Pd nanotubes,[50,51] and Pd networks,[52] have been developed for H_2 sensors. The rational design of Pd nanostructures improved H_2 sensing properties due to their high surface area-to-volume ratio and nanosize effect. Interestingly, Yang *et al.*[16] investigated the influence of Pd nanowire size on H_2 sensing and concluded that the smaller nanowires were both more sensitive and faster. They fabricated Pd nanowire libraries with

https://dx.doi.org/10.1021/acsnano.0c05307
ACS Nano 2020, 14, 14284−14322

different height and thickness, by using lithographically patterned nanowire electrodeposition (LPNE) (Figure 4a).[53] In brief, the LPNE method involves (1) deposition of nickel (Ni) films onto a substrate, (2) ultraviolet (UV) lithography to generate desired patterns, (3) wet etching of Ni to create not only Ni patterns but also a horizontal trench underneath a photoresistor (PR) layer, (4) electrodeposition of Pd within this trench, and (5) removal of PR layer and remaining Ni. This method enables the simple control of the height and thickness of Pd nanowires by modulating the thickness of Ni (height control) and etching/electrodeposition time (thickness control). Thus, they fabricated single Pd nanowires *via* LPNE (Figure 2b) and controlled the height and thickness of single Pd nanowires. The sensing results of single Pd nanowire libraries showed that smaller nanowires were both faster and more sensitive in the range of α-PdH_x ($[H_2] \leq 0.5\%$) (Figure 4c−f). The surface area to volume ratio of single Pd nanowires led to the enhancement of the responses and response times for H_2 detection, particularly for low levels of H_2. The origin of these phenomena is not understood clearly. But the most plausible explanation is that the high surface area to volume ratio of Pd nanowires does not only offer a number of active sites for H_2 adsorption but also lowers the activation energy for solid solution formation reactions of H_2.[16]

Effect of Temperature on Pd-Based H_2 Sensors. Operating temperature of the transducer is also one of the important parameters because surface reactions are hugely affected by temperatures. Yang and co-workers demonstrated the temperature effect on Pd-based H_2 sensors by using the Joule-heating of single Pd nanowires.[54] It is well-known that current flow in metals dissipates heat generated by the scattering of free electrons in metals.[55,56] Thus, the control of an applied voltage on Pd nanowires allowed the simple modulation of the operating temperatures of sensors (Figure 4g). Increasing the operating temperature from RT to 384 K caused the amplitude of the resistance modulation induced by H_2 to decrease by a factor of 38, but the response and recovery times were improved by a factor of 50 (Figure 4h−j). Because the higher operating temperature induces more phonon electron scattering in Pd crystals, the baseline resistances of Pd crystals are increased. Therefore, the additional resistance increase (response) of Pd nanowires upon H_2 exposures was not as high as RT operation (Figure 4h). In terms of response and recovery speed, the high-temperature facilitates H_2 adsorption on Pd nanowires for $[H_2] < 1\%$ and lowers the kinetic barrier for the phase transition of PdH_x from α to β (Figure 4i,j). In short, as the operating temperature of Pd-based H_2 sensors increases, the sensitivity of the sensor is sacrificed for a more rapid response and recovery speed. However, high-temperature operation of the sensor is achieved at the cost of elevated power consumption, a demerit for commercialization.

Negative Effect of Oxygen Molecules on Pd-Based H_2 Sensing. Although a number of Pd-based H_2 sensors have been reported, many have been characterized in backgrounds of nitrogen $[N_2]$ or argon [Ar] or at H_2 partial pressures below the α to β phase transition (≈2%).[24] However, for commercialization, it is crucial that sensors function in ambient air and at high $[H_2]$ concentrations without incurring damage, in order to simplify sensing systems and improve the stability and reliability of sensors. The operation of Pd-based sensors in ambient air has challenges due to the negative effect of oxygen molecules (O_2) that readily adsorbs on the active surface sites of Pd, thereby blocking the reaction sites for H_2 adsorption.[57] In addition, adsorbed oxygen species can react with H_2 and produce water at the Pd surface, reducing the hydrogen available for chemisorption on the Pd surface (Figure 5a and eqs 6 and 7).[29,57]

$$Pd{-}O + 3/2H_2(ads) \rightarrow Pd{-}H + H_2O(ads) \quad (6)$$

$$H_2O(ads) \rightarrow H_2O(gas) \quad (7)$$

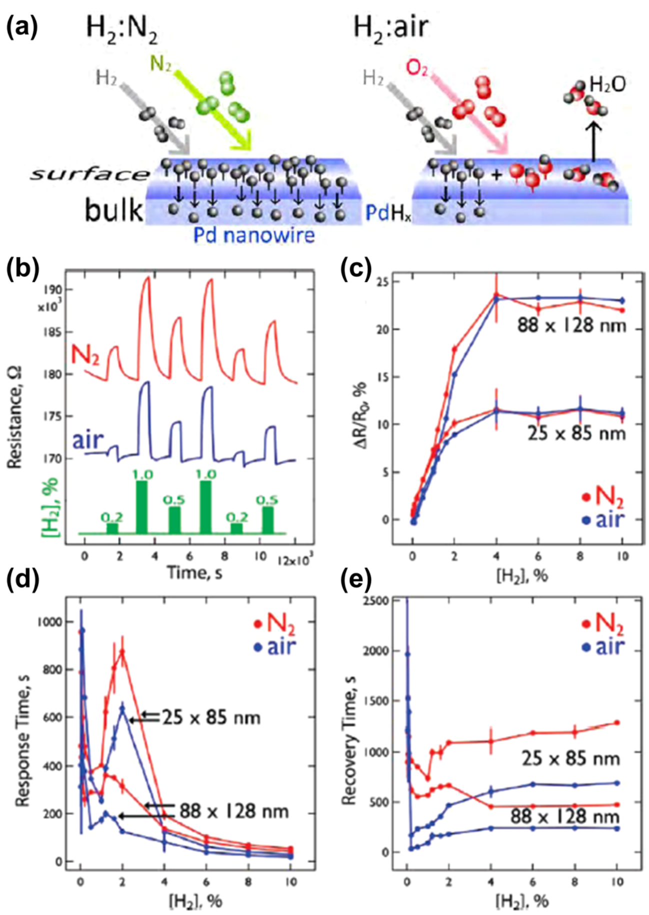

Figure 5. (a) Schematic illustration of the negative effect of oxygen molecules in air on Pd-based H_2 sensors. Reprinted with permission from ref 29. Copyright 2015 American Chemical Society. (b) Resistance trances of Pd nanowires at RT in N_2 and ambient air and their corresponding sensing properties: (c) response, (d) response time, and (e) recovery time. The height and thickness of single Pd nanowires are presented in the graph. Reprinted with permission from ref 16. Copyright 2010 American Chemical Society.

Figure 5b−e shows the influence of oxygen on H_2 sensing properties of Pd nanowires. The responses of Pd nanowires in ambient air were slightly decreased compared to those in N_2 (Figure 5c). However, the detection limits of the sensors were increased from 2−5 ppm in N_2 to 1000−2000 ppm in air. In addition, the response and recovery times of the sensors in air were extended (slowed) by a factor of 2 as compared with those measured in N_2 (Figure 5d,e). Therefore, it is important to minimize the strong influence of oxygen on Pd-based H_2 sensors.

In addition to the oxygen molecules, water molecules in air are also able to deteriorate sensing properties of Pd-based sensors. Water molecules in air readily adsorb on the surface of

https://dx.doi.org/10.1021/acsnano.0c05307
ACS Nano 2020, 14, 14284−14322

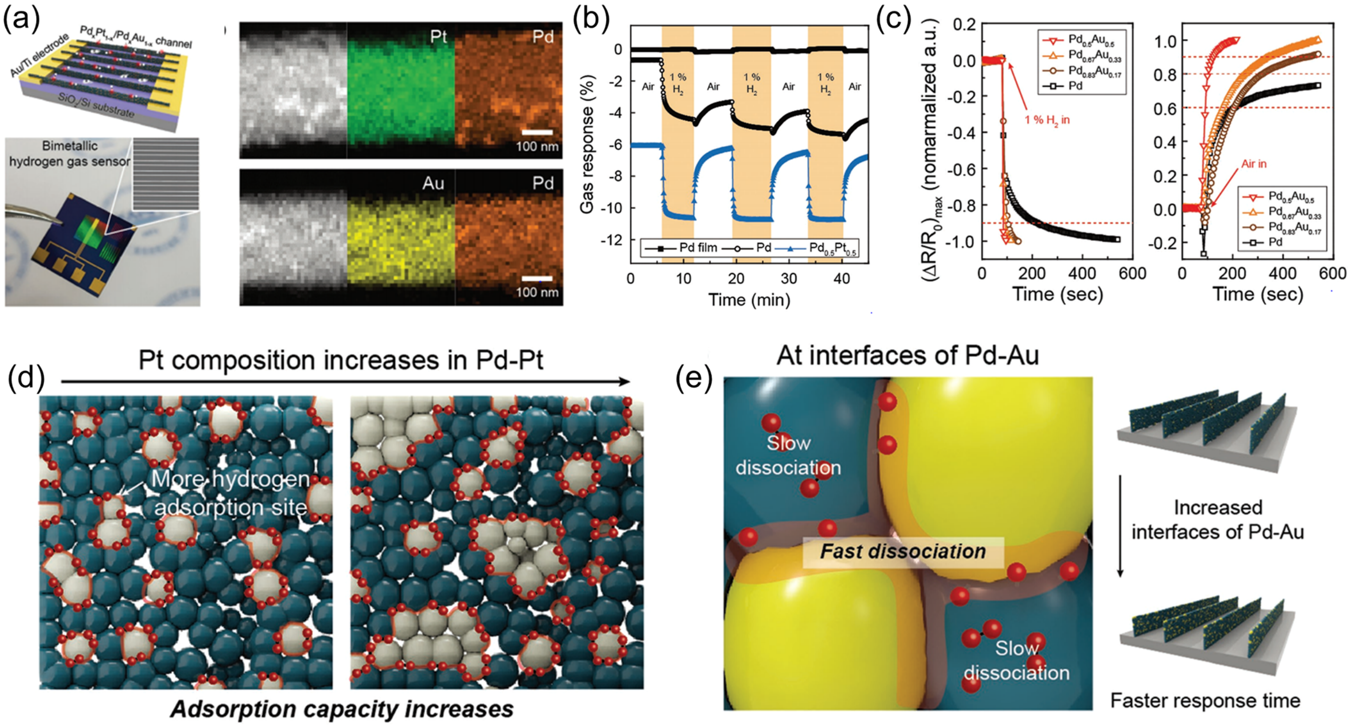

Figure 6. (a) Schematic illustration and photograph of a Pd-based bimetal (Pd/Pt and Pd/Au) sensing device and the EDS mapping images. (b) Normalized responses of Pd film, Pd, and Pd/Pt sensors toward 1% H_2. Response was defined as $\Delta R/R_0$ (%). (c) Normalized curves of response and recovery behavior of Pd/Au sensors with various composition ratios toward 1% H_2. Schematic illustrations showing the sensing mechanisms in terms of (d) enhanced response of the Pd/Pt sensor and (e) response time of the Pd/Au sensor. Reprinted with permission from ref 30. Copyright 2018 Wiley-VCH.

Pd sensing layers, which decreases the active sites. Thus, responses and sensing speed of Pd-based sensors are degraded in highly humid atmospheres. For example, Gao *et al.*[58] reported that the response of Pd/Si-based C-FET sensors was decreased from 27% in dry air to 22% in humid air (80% relative humidity) upon exposure to 0.8% H_2. In addition, when the relative humidity was increased from 12% to 71%, the response and recovery times of Pd/Si-based sensors were increased from 23 to 27 s (1.2-fold increased value) and from 17 to 54 s (3.2-fold increased value), respectively.[59] Therefore, the reliability of H_2 sensors should be proven in various humidity levels for practical applications of Pd-based H_2 sensors.

Pd-Based Bimetals. Previously, it was demonstrated that Pd-based alloys with silver (Ag)[60,61] or Ni[48] improved the stability of Pd-based sensors, because alloying Pd with other elements suppressed the α-to-β phase transition of PdH_x.[62,63] However, despite these interesting results, the sensors had some challenges, such as low response amplitudes, sluggish sensing speed, and poor detection limits. To address these issues, some interesting approaches using Pd-bimetals for H_2 sensors have recently been reported.

One recent advance in Pd-bimetals is the demonstration of platinum (Pt)-modified Pd nanowires (Pd@Pt nanowires) reported by Li *et al.*[29] Inspired by the fact that Pt is a better catalyst for catalytic water formation than Pd (eqs 6 and 7),[64−66] they hypothesized that the response and recovery speeds of Pd-based sensors are accelerated by removing adsorbed oxygen on the surface of Pd@Pt nanowires. To demonstrate the catalytic effect of Pt layers, they fabricated Pd@Pt nanowires using sequential electrodeposition of Pd and Pt. Although the responses of Pd@Pt nanowires were decreased relative to pristine Pd nanowires due to the coverage of non-active Pt, the response and recovery times of Pd@Pt nanowires were significantly improved compared to Pd nanowires. The response times to 1% $[H_2]$ in air at RT were accelerated from 450 s for pristine Pd nanowires to 250 s for Pd@Pt nanowires, while recovery times were accelerated from 480 to 15 s. At a higher operating temperature (376 K), Pd@Pt nanowires exhibited an ultrafast response time (2 s to H_2 4%) and recovery time (2.5 s to H_2 4%) for H_2 sensing, although the responses and detection limits were decreased compared to those of the values obtained at RT.

In addition, various Pd-based multimetallic nanostructures can improve H_2 sensing performances by reducing the adsorption and dissociation energy of H_2 due to their synergistic effect in geometry and chemical/physical properties. In this regard, Jung *et al.*[30] developed Pd/Pt and Pd/Au bimetallic nanopattern arrays, which were prepared by the nanolithography *via* plasma ion bombardment,[67] for H_2 sensors (Figure 6a). Compared to reference Pd nanofilm, Pd nanopattern and $Pd_{0.5}Pt_{0.5}$ nanopattern sensors exhibited 14-fold and 45.5-fold higher responses to H_2 1%, respectively (Figure 6b). In addition, $Pd_{0.5}Au_{0.5}$ nanopattern sensors showed about a 73-fold and 4.6-fold enhancement in response and recovery speeds compared to those of pristine Pd nanopattern (Figure 6c). The enhancement in responses and/or response/recovery speeds is synergistically boosted by (1) the structural effect, such as high surface-to-volume ratio of nanopattern, ultrasmall grain size (<5 nm), and ultrathin (<15 nm) nanostructure and (2) the synergistic effect of bimetals (Pd/Pt or Pd/Au) on H_2 sensing. Pd/Pt bimetals provide more active sites for H_2 adsorption than unary Pd metals, in order to reduce the internal stress originated from the lattice

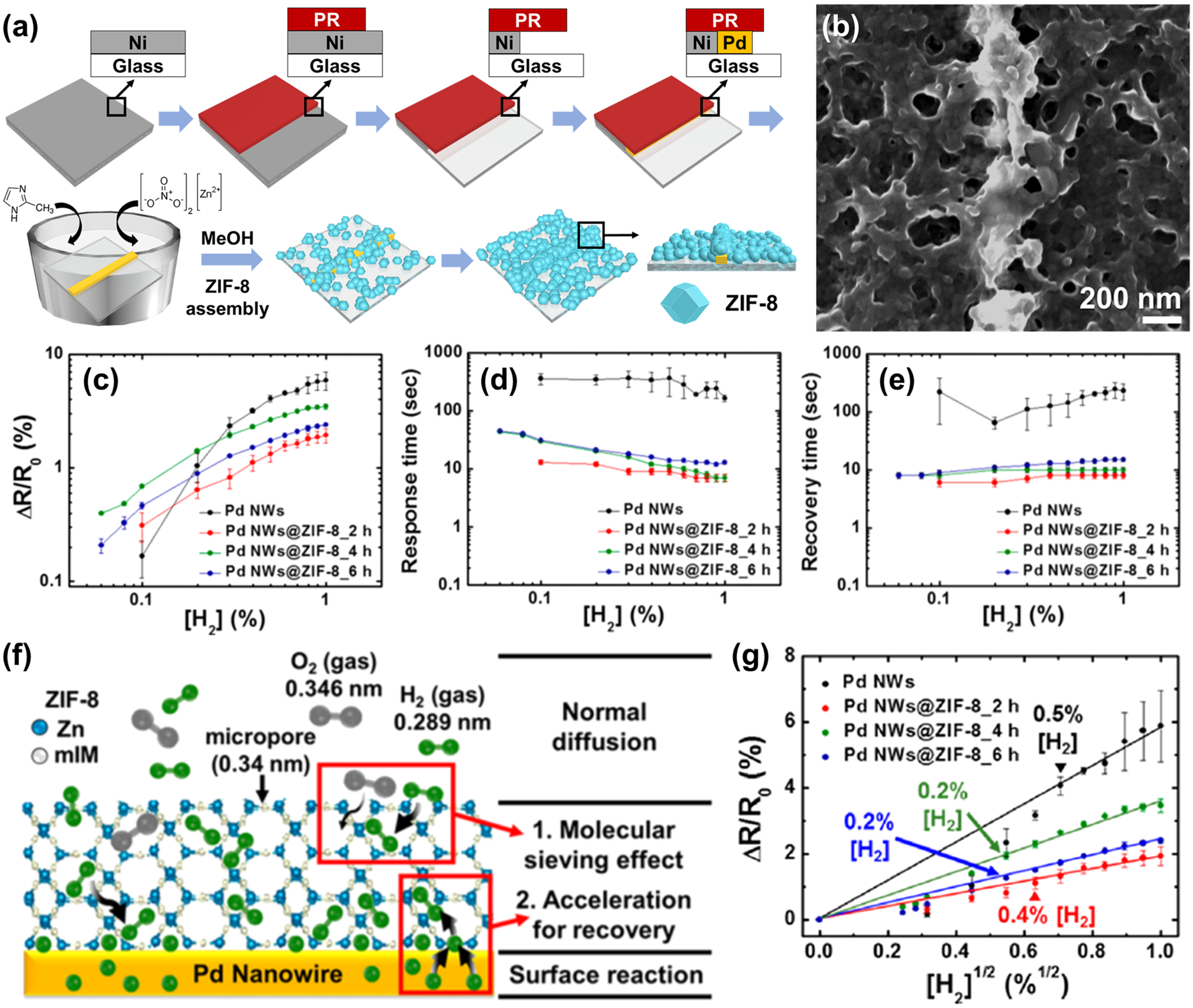

Figure 7. (a) Schematic illustration of the fabrication of Pd nanowires coated by ZIF-8 (Pd NWs@ZIF-8_X h, X h indicates the deposition times for ZIF-8. (b) SEM image of Pd NWs@ZIF-8. Sensing properties of pristine Pd nanowires and Pd NWs@ZIF-8: (c) responses, (d) response times, and (e) recovery times. (f) Schematic illustration of the sensing mechanisms. (g) Responses of the sensors *versus* $[H_2]^{1/2}$. Reprinted with permission from ref 31 (ZIF-8: Zn-based zeolite imidazole framework). Copyright 2017 American Chemical Society.

mismatch of the interfaces of Pd/Pt grains (Figure 6d).[68] Meanwhile, Pd/Au bimetals featured faster H_2 dissociation properties than pristine Pd metals, owing to the higher degrees of freedom caused by the formation of heteroatom bonds between Pd and Au (Figure 6e). In this sense, the adsorbed H_2 is likely to be dissociated to form PdH_x with extremely fast response time. This study demonstrated the potential feasibility of multicomponent metals for use in H_2 sensors.

Pd-Based Composites. The combination of Pd with other materials induces synergistic effects, thus we can solve remaining challenges in Pd-based sensors by using Pd-based composites. In this section, we introduce the representative recent advances in Pd-based composites for H_2 sensors and elucidate their underlying mechanisms.

In order to minimize the negative effect of oxygen on Pd-based sensors, Koo *et al.*[31] developed a zinc (Zn)-based zeolite imidazole framework (ZIF-8)-coated Pd nanowire array. Because ZIF-8 allows a highly selective penetration of H_2 compared to other large gas molecules due to small pore size (0.34 nm) of ZIF-8,[69,70] a ZIF-8 layer effectively minimizes the negative effect of oxygen on Pd-based H_2 sensors. They first synthesized a Pd nanowire array using LPNE,[53] and then, ZIF-8 was overcoated on the Pd nanowire array (Pd NWs@ZIF-8_X h, X h indicates the deposition time for the self-assembly of the ZIF-8 layer) by the *in situ* self-assembly of ZIF-8 (Figure 7a,b) in methanol. The Pd NWs@ZIF-8 showed lower responses at high H_2 concentrations than pristine Pd NWs because the surface of Pd NWs was covered by ZIF-8 (Figure 7c). Very surprisingly, the response and recovery times of Pd NWs@ZIF-8 were significantly accelerated from 164 to 7 s for the response and from 229 to 10 s for the recovery, compared to pristine Pd nanowires (Figure 7d,e). This acceleration is attributed to the molecular sieving effect of ZIF-8. Because the pore size of ZIF-8 is 0.34 nm, the diffusion of H_2 with kinetic diameter of 0.289 nm in ZIF-8 is much easier compared to that of O_2 (0.345 nm) (Figure 7f). The theoretical calculations using Sievert's law also confirmed the molecular sieving effect of ZIF-8 on Pd nanowires. From the Sievert's law, the

https://dx.doi.org/10.1021/acsnano.0c05307
ACS Nano 2020, 14, 14284−14322

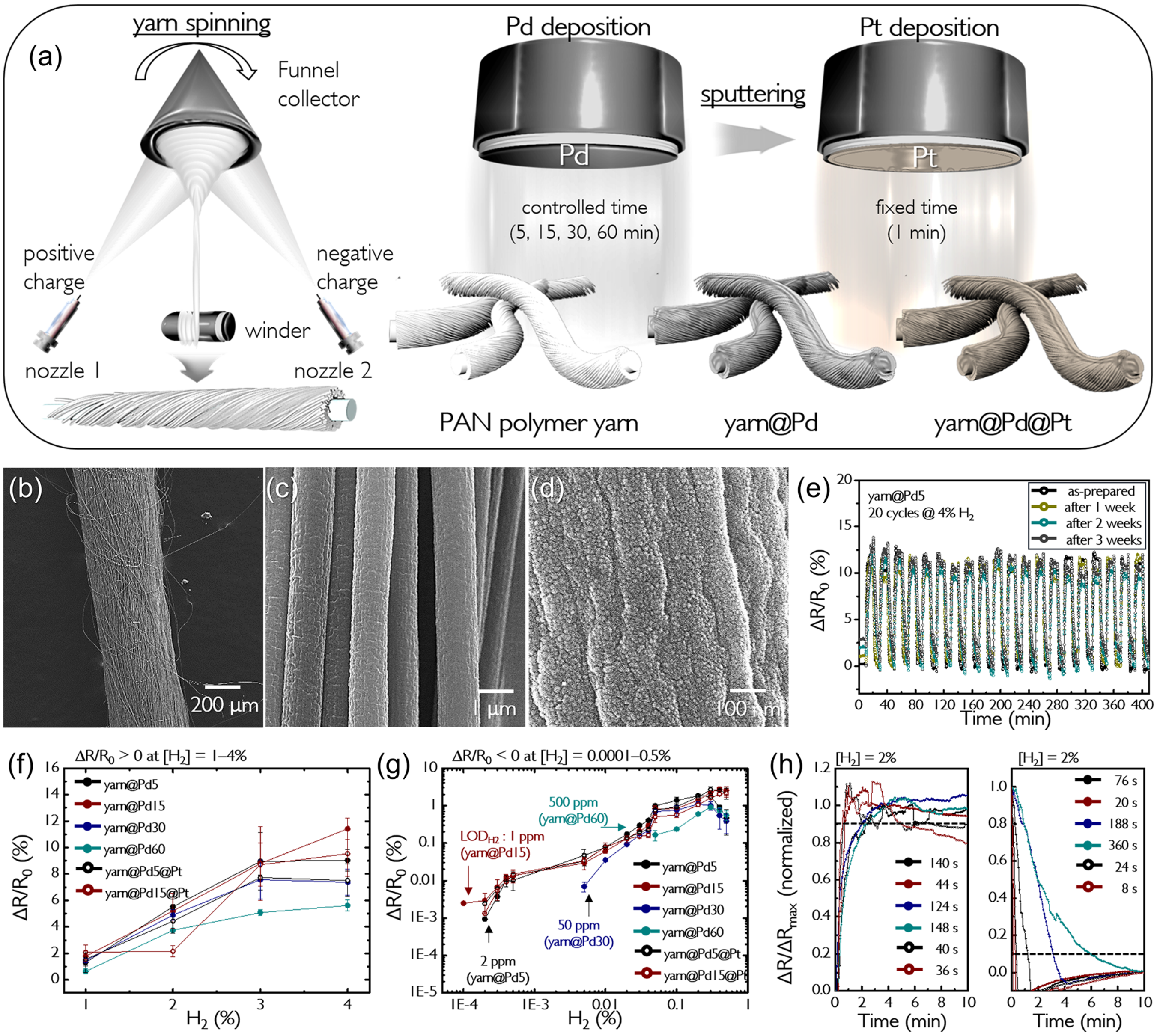

Figure 8. (a) Schematic illustration of the synthesis of the yarn@Pd and yarn@Pd@Pt using yarn-spinning and subsequent sputter deposition of Pd and Pt (PAN: polyacrylonitrile). (b–d) SEM images of yarn@Pd15. (e) Long-cycling stability tests to H_2 4% for 20 cycles using yarn@Pd5. Normalized responses *versus* $[H_2]$ at H_2 concentrations of (f) 1–4% and (g) 0.0001–0.5%. (h) Normalized curves of response and recovery to H_2 2%. Reprinted with permission from ref 71. Copyright 2019 American Chemical Society.

resistance changes of Pd NWs will be linearly proportional to $[H_2]^{1/2}$ ($\Delta R/R_0 \propto [H_2]^{1/2}$) in an ideal case, but the negative effect of oxygen induces non-ideal H_2 sensing behaviors. In their calculations, the non-ideal behaviors of Pd NWs were minimized by the use of ZIF-8 layers (Figure 7g). Therefore, the disturbance of oxygen on Pd-based H_2 sensors is effectively reduced by using the molecular sieving layer, accelerating the response/recovery speed even in ambient air.

In addition, as discussed above, Pd-based H_2 senors possess inherent limitations in terms of long-cycling stability owing to the repeated volume expansion and relaxation upon the formation of the β-PdH$_x$ ($[H_2] \geq 2\%$).[41,45] To address this issue, Kim *et al.*[71] developed a flexible H_2 sensing platform based on a single-strand nanofiber yarn which consists of high-density electrospun nanofibers, on which nanogranular Pd or Pd@Pt was coated *via* sputtering (Figure 8a). The method for nanofiber yarn fabrication is an advanced electrospinning technique that requires two individual nozzle systems at which polymer nanofibers are ejected to the rotating funnel collector to form core-support wire/shell-electrospun nanofibers of the yarn scaffold.[72] Pd-deposited nanofiber yarn (yarn@Pd) and Pt-sensitized yarn@Pd (yarn@Pd@Pt) were prepared by consecutive Pd and Pt sputter deposition. The SEM images displayed that the yarn with a diameter of 600 μm consists of several hundreds of well-aligned Pd-coated nanofibers with the yarn direction (Figure 8b,c). The high-resolution SEM image of the yarn@Pd showed the rough surface with ultrasmall Pd grains (<10 nm) (Figure 8d). Since Pd sensing layers were mechanically coupled with a flexible polymeric nanofiber, the yarn@Pd-based sensors endured severe stress during repeated volume expansion/relaxation. To demonstrate the long-term stability, the sensors were exposed to H_2 4% for 20 cycles, and

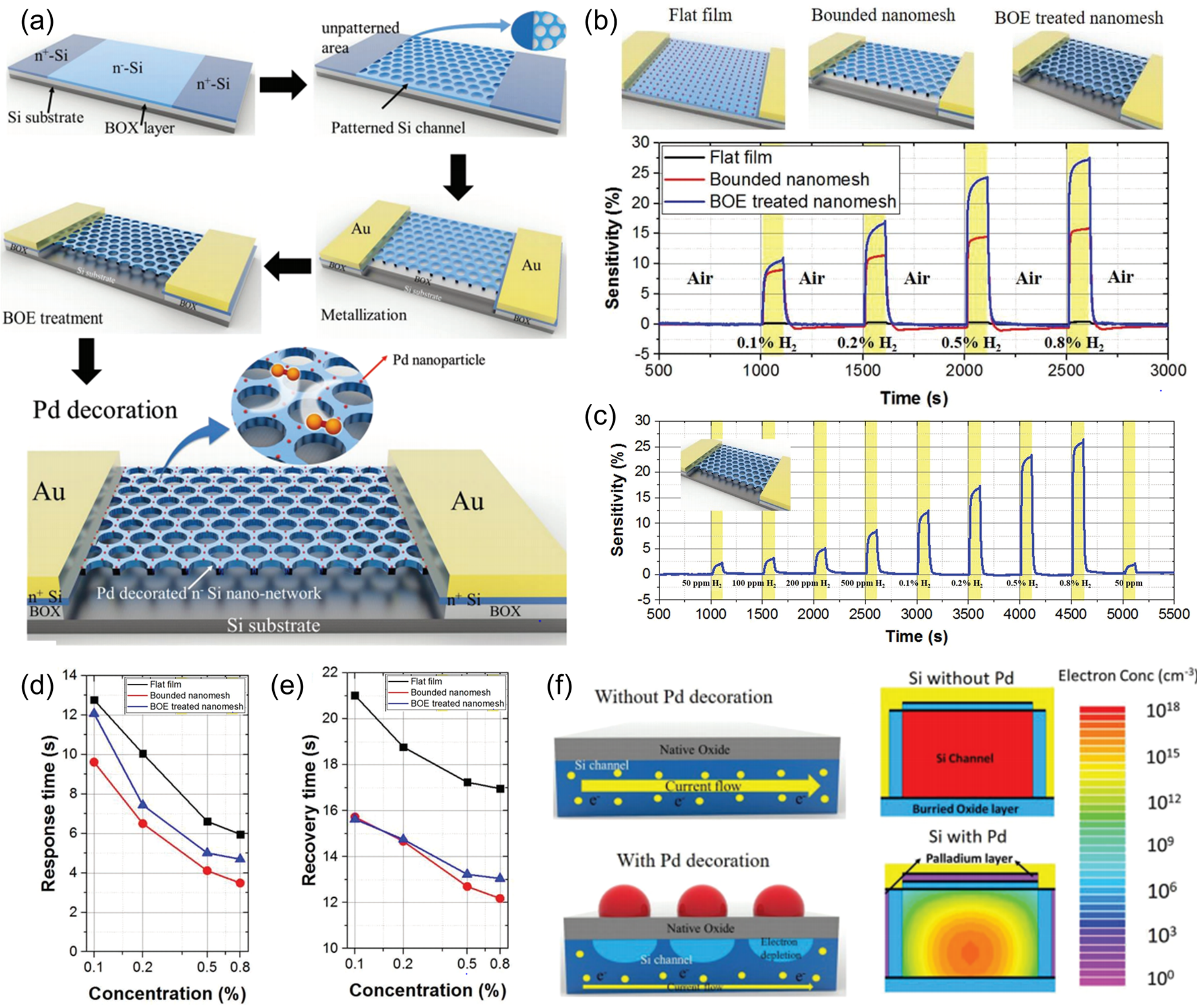

Figure 9. (a) Schematic illustration of the fabrication process for the Pd-deposited Si nanomesh H_2 sensors (BOX: buried oxide and BOE: buffered oxide etchant). Real-time sensing signals of (b) flat film, bounded nanomesh, and BOE-treated nanomesh sensors to 0.1, 0.2, 0.5, and 0.8% H_2 and (c) BOE-treated nanomesh sensor to H_2 with concentrations of 50 ppm to 0.8%. (d) Response and (e) recovery times for three different types of sensors toward 0.1, 0.2, 0.5, and 0.8% H_2. (f) Schematic illustration of the resistance change and electron concentration profiles in a Si channel with and without Pd deposition. Sensitivity in (b) and (c) was defined as $\Delta I/I_0$ (%). Reprinted with permission from ref 58. Copyright 2018 Wiley-VCH.

the cycle tests were repeated after 1, 2, and 3 weeks. As a result, the yarn@Pd-based sensors showed good reliability and long-term stability without a degradation in response (Figure 8e). In addition, the nanofiber yarn-based H_2 sensors exhibited a wide range for H_2 sensing from 0.0001 to 4% (Figure 8f,g). Moreover, yarn@Pd@Pt showed about 2−3-fold faster response (40 s) and recovery speeds (24 s) to H_2 2% than those (140 s for response and 76 s for recovery) of yarn@Pd (Figure 8h). The yarn@Pd-based H_2 sensing platform offers the development of single-strand wearable chemiresistors that possess a high surface-to-volume ratio and open porosity to facilitate target gas diffusion and reaction.

Pd/Si-Based Chemical Field-Effect Transistors. Pd/Si-based C-FETs also have attracted much attention because of their high compatibility with conventional complementary metal-oxide-semiconductor (CMOS) technology. The sensing mechanisms of Pd/Si-based devices rely on the phase transition from metallic Pd to resistive PdH_x upon H_2 sensing. This phase transition of Pd can modulate the charge carrier concentrations in the semiconductor layer underneath, effectively.[32] In this regard, Gao *et al.*[58] reported a H_2 sensor based on a Pd-deposited Si nanomesh nanostructure patterned using the polystyrene (PS) nanosphere lithography (Figure 9a). Following the consecutive heavy and low-level doping processes to obtain n^+−n^-−n^+ junction (source, channel, and drain) structure by ion implantation, PS nanosphere templating route-derived lithography and top-down fabrication process were performed to obtain Pd-deposited Si nanomesh structure. In particular, buffered oxide etchant (BOE) treatment was introduced to induce a rough surface of the Pd/Si sensing layers. Compared to the flat film sensor, nanomesh or BOE-treated nanomesh sensors showed dramatically enhanced H_2 sensing response (Figure 9b). The BOE-treated nanomesh sensors exhibited ultralow detection limits

https://dx.doi.org/10.1021/acsnano.0c05307
ACS Nano 2020, 14, 14284−14322

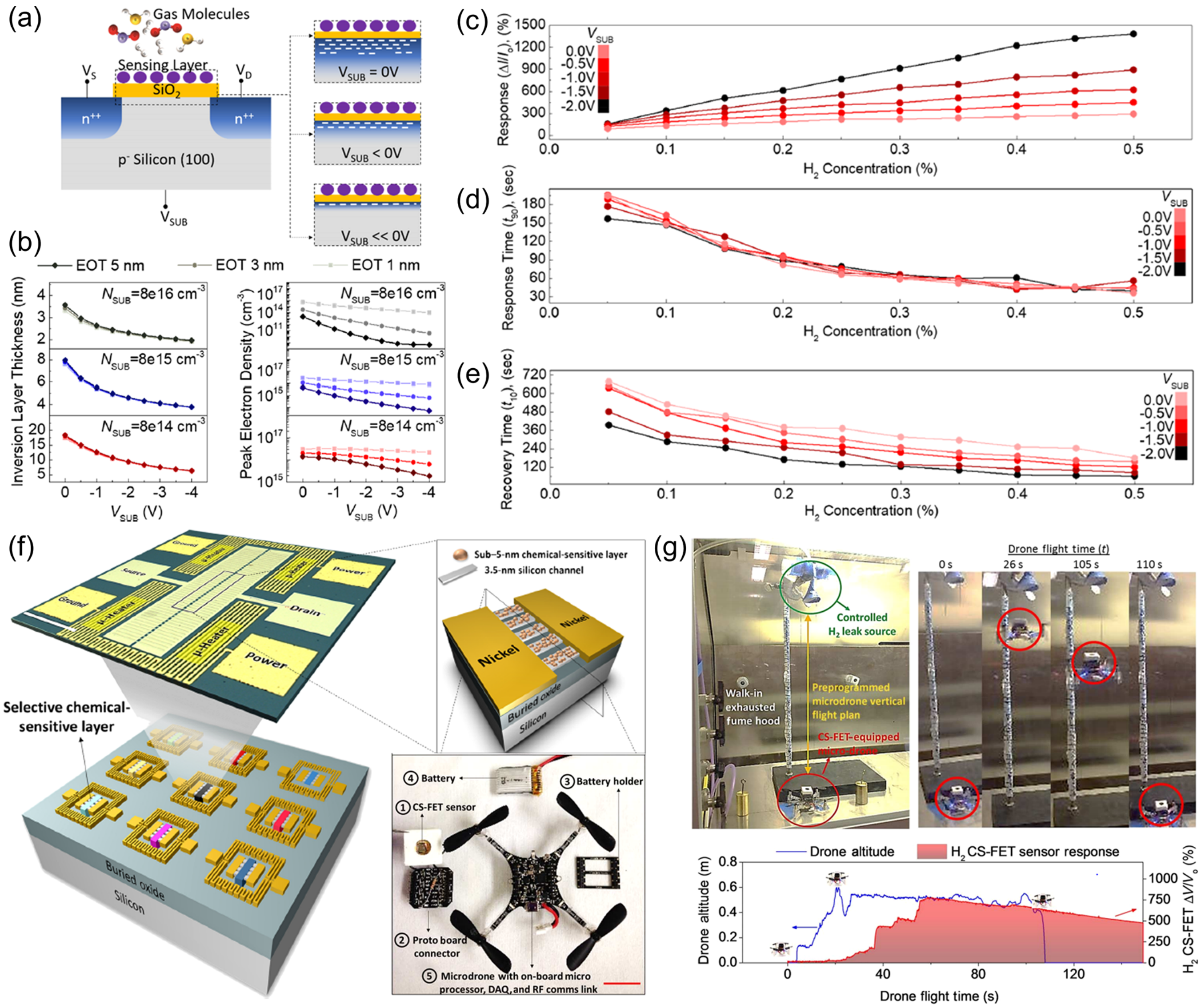

Figure 10. (a) Schematic illustration of the fabrication of a bulk silicon C-FET with the electronic confinement of the charge inversion layer. (b) Inversion layer thickness and peak electron density profiles at different body biases. (c) Sensor response, (d) response time, and (e) recovery time *versus* [H_2] at different V_{sub}. Reprinted with permission from ref 32. Copyright 2018 American Chemical Society. (f) Schematic illustrations and detailed image of a C-FET chip and a camera image showing a microdrone equipped with a Ni−Pd-based C-FET sensor. (g) Real-time H_2 sensing experiment using the C-FET-equipped microdrone. Reproduced with permission under a Creative Commons CC-BY license from ref 33. Copyright 2017 American Association for Advancement of Science.

(50 ppm) with high responses (2.5%) and fast response/recovery kinetics (5 s for response and 13 for recovery) to H_2 1% (Figure 9c). In addition, Pd-deposited Si nanomesh-based sensors displayed about 10 and 16 s of fast response and recovery speeds in response to H_2 0.1% (Figure 9d,e). The formation of PdH_x to H_2 exposure induced the formation of an electron depletion region on the underneath Si channel, modulating its current flow (Figure 9f). The Pd/Si-based H_2 sensors demonstrated a high-performance, low-cost, and facile fabrication process technology that is highly compatible with mobile and wearable devices supported by the CMOS integration.

For other cases of C-FET-based H_2 sensors, Fahad *et al.*[32] demonstrated highly sensitive Pd/Ni-deposited C-FET H_2 sensors with sub-5 nm thin charge inversion layers. Figure 10a illustrates the conceptual sensing device and sensing mechanisms of the bulk silicon FETs where the sensing layer features large surface area and ultrathin characteristics. It is noted that 0.3 nm of Ni and 1 nm of Pd are deposited on the Si-channel to form Ni/Pd-deposited C-FET H_2 sensors. The thickness and peak electron density of inversion layers in the C-FET decreased as the reverse body bias (V_{sub}) increased (Figure 10b). To investigate the effect of the V_{sub} on Pd/Ni-based C-FET H_2 sensors, the H_2 sensing properties of Ni−Pd FETs sensors were measured to 0.05−0.5% H_2 as a function of the V_{sub} values ranging from 0 V to −2 V. Interestingly, the H_2 sensing properties of the Pd/Ni-based C-FETs sensors were highly dependent on the threshold voltage of the transistors (Figure 10c−e). The sensor response dramatically increased from 291% to 1393% to 0.5% H_2 by increasing the V_{sub} from 0 V to −2 V (Figure 10c). The response and recovery kinetics of the sensors depending on the applied V_{sub} were also investigated (Figure 10d,e). It was demonstrated that the V_{sub} has no effect on the response times of the Pd/Si-based C-

https://dx.doi.org/10.1021/acsnano.0c05307
ACS Nano 2020, 14, 14284−14322

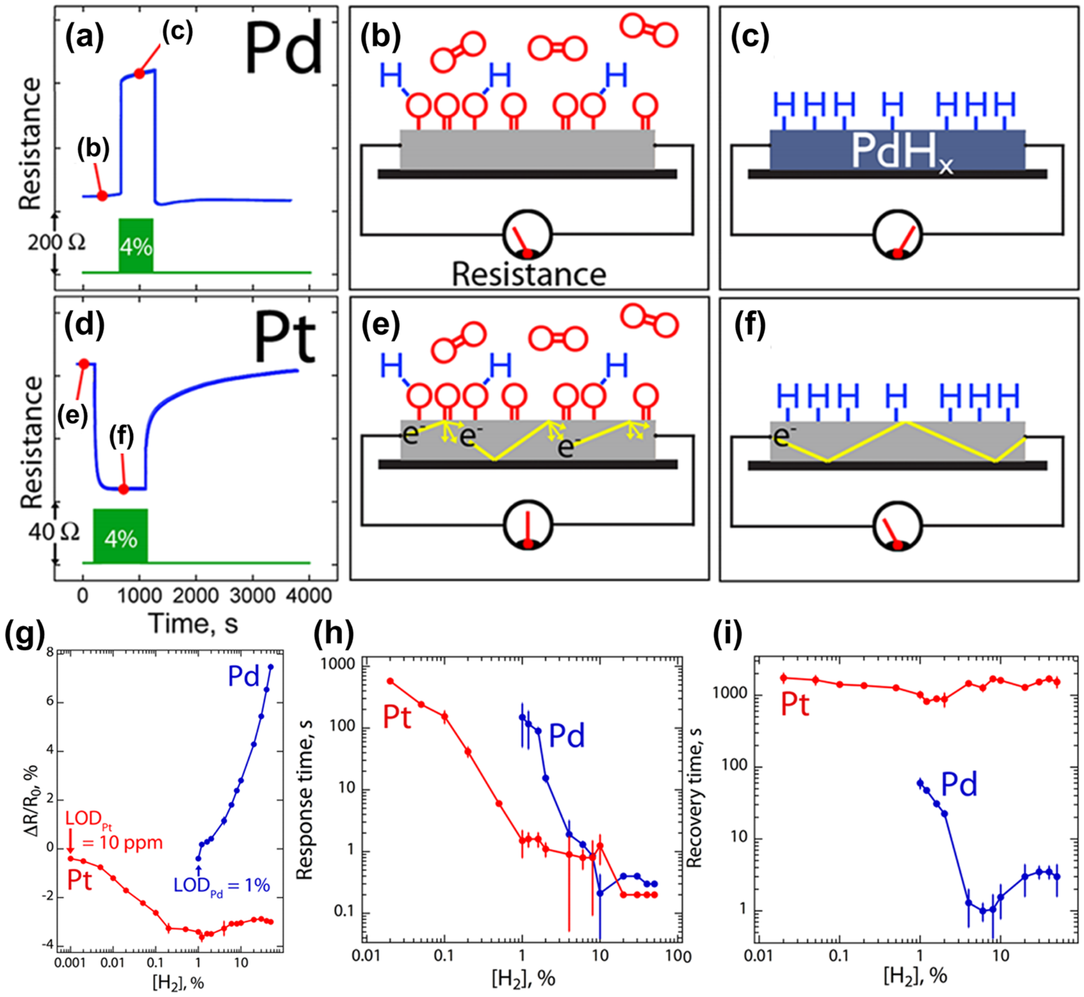

Figure 11. (a) Resistance traces of a Pd nanowire for an exposure of H_2 4%, showing an increase in resistance. Schematic illustration of Pd metal surface (b) in air and (c) in flowing H_2. (d) Resistance traces of a Pt nanowire in response to H_2 4%. (e) Schematic illustration of Pt metal surface in air. The electrons are scattered at the oxygen-terminated surface that exists in dry air. (f) Schematic illustration of Pt metal surface in flowing H_2. The electron scattering is less prominent for the H-terminated wire surface. (g) $\Delta R/R_0$ *versus* $[H_2]$ plot for a Pt and Pd nanowire. (h) Response time *versus* $[H_2]$ for Pt and Pd nanowires. (i) Recovery time *versus* $[H_2]$ for Pt and Pd nanowires. Reprinted with permission from ref 34. Copyright 2012 American Chemical Society.

FET H_2 sensors, because the response times are mainly dependent on the rate of H_2 diffusion and adsorption on the sensing layers. Meanwhile, the recovery times were dramatically reduced under larger reverse biases, due to the different $I-V$ characteristics (the inversion layer thickness and peak electron density). The Fahad group also developed C-FET sensor arrays based on an ultrathin (<5 nm) chemiresistive sensing layer coupled to the 3.5 nm-thin silicon channel transistors.[33] By introducing multiple processing steps, $Pd_{0.3\ nm}Au_{1\ nm}$, $Ni_{0.3\ nm}Pd_{1\ nm}$, and $Ni_{1\ nm}$ deposited 3.5 nm-thin silicon transistors were prepared as low-power, sensitive, and selective multiplexed chemiresistors for H_2S, H_2, and NO_2 sensing, respectively (Figure 10f). Based on the multiplexed gas sensors platform integrated onto a single chip, consecutive exposure to three different target gas molecules can be detected with good sensing performance, that is, 10 ppm of H_2S, 0.5% H_2, and 100 ppm of NO_2 as well as the mixed gas can be detected, respectively. The low-power consumption of the multiplexed chemiresistor platform enables the integration with mobile wireless electronics, thus Pd/Ni-deposited C-FET H_2 sensors were integrated onto a wireless drone as a proof-of-concept (Figure 10g). The successful real-time H_2 sensing data were collected along with the vertical sensors-integrated drone flight path from takeoff and climb at a steady rate to the upper regions, where the controlled leak of pure H_2 was carried out. These studies demonstrated that the Pd/Si-based C-FET H_2 sensors are sensitive, selective, and low-power sensing platforms with high compatibility to conventional CMOS technology.

Other Metal-Based Materials. Compared to metallic Pd-based H_2 sensors that have the transduction mechanism of forming a stable PdH_x upon H_2 exposure, not many metals have been investigated for their hydrogen sensing properties, owing to their incapability to form hydride phases under H_2 exposure. Interestingly, it has recently been demonstrated that Pt-based sensors are able to detect H_2 by using catalytic water formation reactions.[34] However, the speed of water formation reactions at the surface of other metals is significantly slow compared to that of Pt surfaces,[65,66] hence, those other metals are difficult to exploit the surface electron scattering mechanism.

Basic Sensing Mechanisms for Pt-Based Sensors. The sensing mechanism for Pt-based H_2 sensors depends on removal of adsorbed oxygen species (water formation) on Pt

https://dx.doi.org/10.1021/acsnano.0c05307
ACS Nano 2020, 14, 14284−14322

Table 1. Summary of Sensing Properties of Metal-Based H_2 Sensors Operated at Room Temperature in Air[a]

sensing material	response $[H_2]$ 0.1%	t_{resp}^b/t_{rec}^c $[H_2]$ 0.1%	response $[H_2]$ 1%	t_{resp}/t_{rec} $[H_2]$ 1%	LOD[d] ($[H_2]$)	measurement range[e]	ref
Pd nanofiber yarn	1.37%	236 s/388 s	2%	n.r.	1 ppm	1 ppm to 4%	71
yarn@Pd@Pt	0.93%	88 s/378 s	1.2%	n.r.	1 ppm	1 ppm to 4%	71
Pd nanopattern	0.8%	230 s/680 s	1.5%	12 s/30 s	2.5 ppm	2.5 ppm to 4%	75
Pd nanotube array	1000%	180 s/n.r.	3750%	200 s/n.r.	100 ppm	100 ppm to 1%	51
Pd/Pt nanopattern ($Pd_{0.5}Pt_{0.5}$)	n.r.	7 s/35 s	2%	20 s/40 s	10 ppm	10 ppm to 1%	30
Pd/Au nanopattern	n.r.	8 s/30 s	n.r.	2 s/70 s	10 ppm	10 ppm to 1%	30
PdPt nanoparticles ($Pd_{0.5}Pt_{0.5}$)	1.2%	350 s/458 s	7.56%	92 s/304 s	0.4 ppm	0.4 ppm to 4%	77
Pd-coated SiO_2 nanorods	160%	38 s/n.r.	145.5%	60 s/n.r.	10 ppm	10 ppm to 2%	46
Pd/Ag hollow nanowires	n.a.	n.a.	n.r.	n.r.	100 ppm	100−900 ppm	61
Pd@Pt nanowires	0.7%	500 s/450 s	5.5%	75 s/35 s	500 ppm	500 ppm to 4%	29
Pd nanowires @ZIF-8	0.8%	8 s/30 s	3.47%	7 s/10 s	600 ppm	600 ppm to 1%	31
Pd/Mg film	1.6%	n.r.	3%	6 s/32 s	1 ppm	1 ppm to 4%	76
Pd−Ni/Si C-FET	300%	150 s/300 s	n.r.	n.r.	0.05%	0.05−0.5%	32
Pd−Si nanomesh (C-FET)	~10% (C-FET)	12 s/16 s	n.r.	n.r.	50 ppm	50 ppm to 0.8%	58
Ni−Pd/Si C-FET	n.r. (C-FET)	n.r.	~600% (C-FET)	30 s/32 s	n.r.	0.3−2%	33
Pt nanopattern	4.1%	n.r.	n.r.	n.r.	1 ppm	1−1000 ppm	35

[a]n.r. and n.a. indicate not reported and not applicable. C-FET is the chemical field-effect transistor. [b]t_{resp} is the response time. [c]t_{rec} is the recovery time. [d]LOD is the limit of detection verified by experimental measurements. [e]Measurement range is the range of H_2 concentrations at which the sensors displayed noticeable responses. It does not mean an actual detection range.

surface and consequential hydrogen adsorption. In detail, oxygen molecules (O_2) in ambient air are readily dissociated and adsorbed on the surface of Pt, increasing the resistance of Pt nanostructures due to the surface electron scattering by adsorbed oxygen species.[73] Then, when Pt-based sensors are subsequently exposed to H_2, adsorbed oxygen species are reacted and removed by the catalytic water formation reactions (eqs 7 and 8).[64,65] Inelastic scattering of conduction electrons is significantly lower at the hydrogen-terminated Pt surface than the oxygen-terminated Pt surface, hence upon H_2 exposure, the electrical resistance of Pt is noticeably reduced as compared to in the air atmosphere.

$$Pt-O + 3/2H_2(ads) \rightarrow Pt-H + H_2O(ads) \quad (8)$$

Pt-Based Nanostructures. The attempt to employ metallic Pt as H_2 gas sensors was demonstrated by Yang *et al.*[34] They tested the H_2 sensing properties of Pt nanowires at RT in dry air and compared the results with Pd nanowires of same dimensions. Unlike Pd-based H_2 sensors (Figure 11a), which form PdH_x upon H_2 exposure (Figure 11b,c), Pt-based H_2 sensors showed a decrease in the resistance upon H_2 exposure at all concentrations of H_2 (Figure 11d). These resistance decreases are consistent with the aforementioned sensing mechanism that depends on electron scattering (Figures 11e,f). To further demonstrate the effect of reduced electron scattering, the same H_2 sensing tests were carried out in dry N_2. As a result, Pt nanowires did not show any response to H_2 under dry N_2 atmosphere, indicating that surface-adsorbed oxygen species are the key factor for the H_2 sensing mechanism of Pt-based sensors. Surprisingly, Pt nanowires displayed an ultralow limit of detection (LOD) of 10 ppm (Figure 11g) at 550 K, which is 1000 times lower than that of Pd nanowires having the same dimensions (LOD = 1%) at the same operation temperature. In addition, the response times of Pt nanowires at 550 K were much shorter (~2 s), as compared to those of Pd nanowires (~200 s) to H_2 1% (Figure 11h). However, Pt-based sensors showed a long recovery time (>1000 s to 0.02−50% of H_2 at 550 K) (Figure 11i), due to the slow unimolecular kinetics for the desorption of water from the surface.

Yang *et al.* also demonstrated the effect of dimensions of Pt-based sensors on H_2 sensing by using nanowires with heights of 20, 40, and 80 nm. In theory, tuning the dimension of the metal structures to the nanometer scale can maximize the sensitivity of metal-based gas sensors. According to eq 9:[74]

$$\Delta\rho/\rho_0 = 3/16\lambda/d \quad (9)$$

where $\Delta\rho$ is the increase in the resistivity upon gas exposure, ρ_0 is the resistivity of bulk metal, λ is the mean free path of electrons, and d is the critical dimension of the metal structure. Therefore, the dimension control of Pt-based materials in nanometer-scales can maximize the sensitivity of Pt-based H_2 sensors. For the aforementioned 20, 40, and 80 nm-high nanowires, both responses and response times were markedly enhanced with decreasing the height of Pt nanowires, although all dimensions showed extremely long recovery times due to the previously mentioned slow kinetics.

Since the mean-free path (λ_{pt}) of free electrons in Pt metals is known as ~5 nm, the surface scattering of electrons occurs significantly when the size of Pt is close to 5 nm. Therefore, Pt-based H_2 sensors are expected to show the highest performance when its dimension is near 5 nm. In this regard, Yoo *et al.*[35] developed ultrathin Pt nanowire arrays using secondary sputtering lithography, which allows the large-scale synthesis of Pt-based H_2 gas sensors. The ultrathin (10 nm) Pt nanowire arrays showed very low H_2 LOD (1 ppm). They also found that the response of Pt nanowires was increased by a factor of ~10 as the cross-sectional dimension decreased from 40 to 10 nm, which is consistent with the above studies.

Challenges of Metal-Based H_2 Sensors. So far, there have been huge efforts to develop efficient H_2 sensors using metal-based materials. Table 1 summarizes the recent and representative metal-based H_2 sensors, particularly operated at RT in air.[29−33,35,46,51,58,61,71,75−77] The sensors exhibited high H_2 sensing performances, in terms of detection range, response, and sensing speed. However, despite these significant advances in metal-based nanomaterials for H_2 sensors, there

https://dx.doi.org/10.1021/acsnano.0c05307
ACS Nano 2020, 14, 14284−14322

still remain several unresolved challenges. First, response and recovery times for over 1% of H_2 should be further enhanced below 1 s, which is the criteria for H_2 sensors designated by the United States DOE. This fast speed is needed to prevent explosions induced by H_2, which is the fastest and lightest gas. Second, most of the metal-based H_2 sensors exhibited poor sensing properties to low levels of H_2 because they depend on hydride formation for Pd-based sensors and catalytic water formation for Pt-based sensors. In particular, the response and recovery times of metal-based sensors are very slow (over hundreds of seconds to $[H_2] < 0.1\%$). Third, the phase transition of α-to-β PdH_x induces large volume expansions, thereby causing the structural instability to Pd-based sensors during long-term operations. Lastly, reliability of sensors when they are operated in ambient air should be demonstrated because numerous gas molecules in ambient air can influence the sensing performance of metal-based sensors. Even though Pd-based sensors have the obvious sensing mechanisms for H_2 sensing, the surface reaction of H_2 on Pd and the formation of PdH_x can be retarded by other interfering gas species. In the case of Pt-based sensors, surface adsorbed oxygen species can react with other gases, thus the environmental influence on water formation reactions is inevitable. These challenges limit the practical use of metal-based sensors in various applications and industries. Hence, further exploration for developing enhanced metal-based hydrogen sensors is required.

METAL OXIDE-BASED MATERIALS

Semiconducting metal oxides (SMOs) have attracted much attention as chemical sensing layers for the detection of various analytes, due to their high stability, high sensitivity, fast response/recovery speed, low-cost, and facile manufacturing processes.[23] Thus, SMO-based gas sensors have high potential from a market perspective. However, the remaining challenges such as high operating temperature, low selectivity, and vulnerability to humidity need to be solved. In principle, in order to enhance sensing properties of SMO-based sensors, careful control of nanostructures to achieve a large surface area and high degree of porosity is essential, since chemical reactions occur on the surface of SMOs.[78] In particular, several strategies, such as functionalization of catalytic noble metal nanoparticles (NPs),[79] formation of heterojunctions with different SMO/graphene derivations,[23] or employing molecular sieving layer,[80] have been suggested to improve the H_2 sensing characteristics of SMOs. In this section, we describe the basic sensing mechanisms of SMO-based sensors and present recent studies on the development of highly sensitive and selective SMO-based H_2 sensors, in terms of pure SMO-based materials, catalyst/SMO-based materials, and SMO-based composites materials.

Basic Sensing Mechanisms for SMO-Based H_2 Sensors. In general, the working principle of SMO-based chemiresistors is a change of electrical signals (current or resistance) from interaction between H_2 molecules and adsorption oxygen species on a surface of SMOs. The SMOs for gas sensing materials are divided into n-type and p-type materials depending on major carriers as electrons and holes, respectively. In n-type SMOs, such as SnO_2, In_2O_3, and ZnO, physisorbed or chemisorbed oxygen species (O_2^-, O^-, and O^{2-}) are formed by the adsorption of O_2 in the air, and they trap electrons from the conduction band of SMOs. For instance, reactions of oxygen species on SnO_2 depend on operating temperatures (T) and generate chemisorbed oxygen species (eqs 10−13):[21,81]

$$O_2\,(gas) \rightarrow O_2\,(ads) \quad (10)$$

$$O_2\,(ads) + e^- \rightarrow O_2^-\,(ads) \quad (T < 150\,°C) \quad (11)$$

$$O_2^-\,(ads) + e^- \rightarrow 2O^-\,(ads) \quad (150\,°C < T < 400\,°C) \quad (12)$$

$$O^-\,(ads) + e^- \rightarrow O^{2-}\,(ads) \quad (400\,°C < T) \quad (13)$$

Therefore, the adsorbed oxygen species on the surface of n-type SMOs act as a defect site and induce the Fermi level pinning effect on SMOs, thereby forming an electron depletion layer. This electron depletion layer increases the resistances of SMOs significantly, due to the decrement of net carrier density and the formation of potential barriers at the adsorption sites. Then, when SMOs are exposed to H_2, their resistances are decreased because the redox reactions of H_2 and adsorbed oxygen species generate water and free electrons, as in eqs 14 and 15:[82,83]

$$2H_2\,(gas) + O_2^-\,(ads) \rightarrow 2H_2O\,(gas) + e^- \quad (T < 100\,°C) \quad (14)$$

$$H_2\,(gas) + O^-\,(ads) \rightarrow H_2O\,(gas) + e^- \quad (100\,°C < T < 300\,°C) \quad (15)$$

When the SMO-based sensors are exposed to ambient air after the redox reactions with H_2, the adsorption of O_2 in air occurs again and generates chemisorbed oxygen species on the surface of SMOs. Therefore, the resistances of SMO-based sensors are recovered from the low resistance state (in H_2/air) to the high resistance state (in ambient air) (Figure 12a). On the other hand, p-type SMOs, such as Co_3O_4, NiO, and CuO, are operated by the modulation of hole accumulation layers. The adsorption of oxygen molecules on the surface of p-type

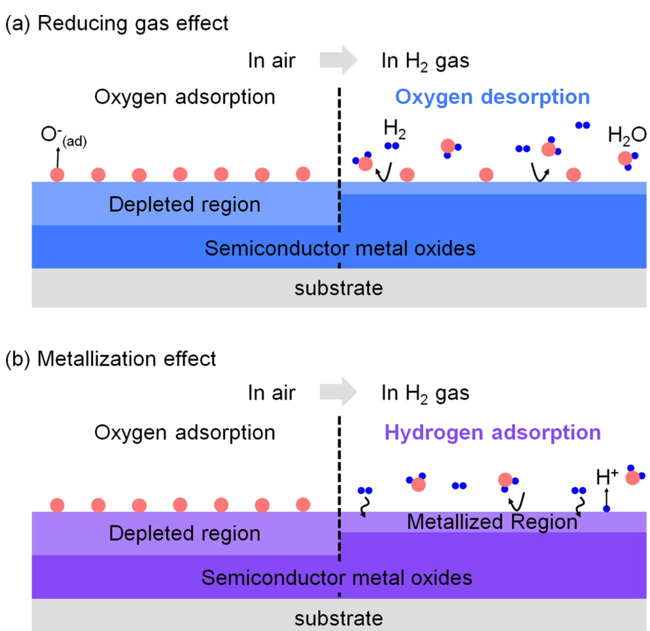

Figure 12. H_2 sensing mechanisms of metal oxide-based H_2 sensors. (a) Reducing gas effect. Reproduced with permission under a Creative Commons CC-BY license from ref 100. Copyright 2012 MPDI. (b) Metallization effect. Reproduced with permission from ref 283. Copyright 2015 Elsevier.

https://dx.doi.org/10.1021/acsnano.0c05307
ACS Nano 2020, 14, 14284−14322

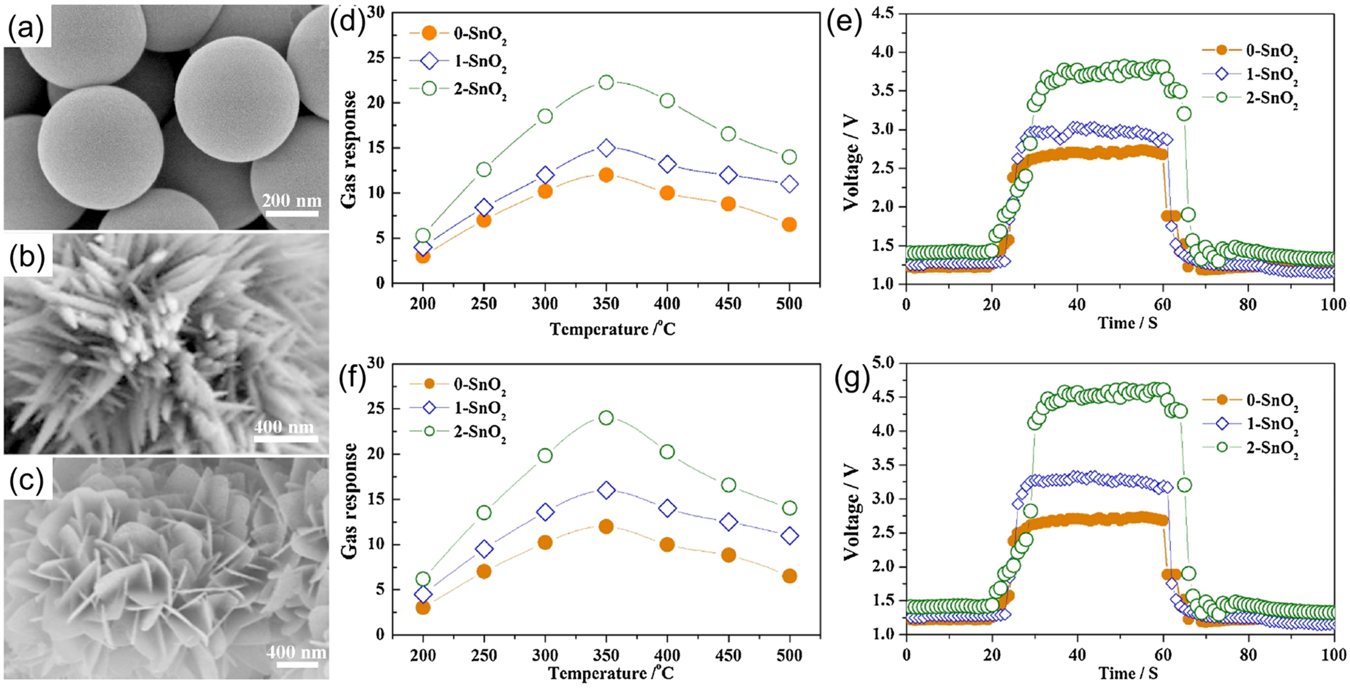

Figure 13. SEM images of the SnO_2 sample: (a) solid spheres, (b) nanoneedle-assembled nanourchins, and (c) nanosheet-assembled nanoflowers. Gas responses of the three sensors exposed to 400 ppm of H_2 at different temperatures (d) in air and (f) in vacuum. Response–recovery curve of the three sensors under H_2 400 ppm at 350 °C (e) in air and (g) in vacuum. Reproduced with permission from ref 106. Copyright 2019 Elsevier.

SMOs generates additional holes, producing hole accumulation layers on the surface of the materials. Then, the resistances of p-type SMO-based sensors are increased in response to H_2 (high resistance state) due to the removal of adsorbed oxygen species and consequent removal of holes in the hole accumulation layers and were recovered in ambient air (lower resistance state). Therefore, both n-type and p-type SMO-based materials should have large surface areas and high reactivity to analytes, in order to increase sensing properties.[84−96]

In addition to the reducing gas effect, in some SMOs, such as ZnO[97,98] and TiO_2,[99] H_2 molecules can be directly reacted with SMOs and induce the metallization of metal oxides (*e.g.*, eq 16). Thus, the metalized region is generated on the surface of SMOs, resulting in a resistance decrease upon H_2 exposures (Figure 12b). Then, when exposed to air again, the metalized region is oxidized to metal oxides, and the resistance of SMOs recovers its baseline resistance.[100]

$$ZnO(s) + H_2(gas) \rightarrow Zn(s) + 2H_2O(gas) \quad (16)$$

Pure SMO-Based Materials. *Effect of Nanosize on SMO-Based H_2 Sensors.* The rational design of SMO-based nanomaterials can enhance sensing properties dramatically. In this regard, Yamazoe *et al.*[101] demonstrated that the smaller grain size of SMOs induces better sensing performances due to the modulation of electron depletion layers (L) in SMOs. To investigate the grain size effect of SMOs on H_2 sensing, they prepared SnO_2 NPs with different sizes from 5 to 32 nm, using a conventional hydrothermal method. Then, the SnO_2 NPs were exposed to H_2 in dry air at 300 °C. The H_2 responses of SnO_2 NPs were significantly increased as grain sizes decreased, particularly for below 6 nm. Interestingly, this critical size (6 nm) is matched with the theoretical values for $2L$ ($L \approx 3$ nm) of SnO_2 at 300 °C.[101] Hence, controlling the depth of the L in SMOs is one of the key factors to improve gas sensing characteristics. In particular, the design of nanostructures, composition control, and the functionalization of catalysts are essential for effectively modulating the thickness of L in SMOs.[78]

Design of SMO-Based Nanostructures. SMO-based nanostructures possess intriguing chemical and physical properties compared to their bulk-scale counterparts, due to their high specific surface areas (high surface to volume ratio).[21,23,102] These properties are essential for the improvement of gas sensing properties because gas sensors highly rely on surface reactions of analytes.[19,103] Therefore, many researchers have focused on designing the SMO-based nanostructures with ultrasmall grains, in order to develop high-performance gas sensors. SMO-based nanostructures can be classified as zero-dimensional (0D) nanostructures, one-dimensional (1D) nanostructures, two-dimensional (2D) nanostructures, and three-dimensional (3D) nanostructures.[19]

0D SMO-Based Nanostructures. The 0D nanostructures include NPs and nanospheres[101,104] as well as their hollow structures.[105] The 0D structures have high surface to volume ratios, however, they can be easily agglomerated during the device fabrication, which can decrease the porosity and active sites of the sensing layers. Li *et al.*[106] investigated the structural effect of SnO_2 NPs on H_2 sensing performances. Figure 13a−c depicts that SnO_2 nanostructures as solid spheres (0-SnO_2), nanoneedle-assembled structures (1-SnO_2), and nanosheet-assembled nanoflowers (2-SnO_2) were prepared by a hydrothermal method. The SnO_2 nanostructure-based sensors were exposed to 400 ppm of H_2 at different operating temperatures from 200 to 500 °C in air. The highest responses for 0-SnO_2, 1-SnO_2, and 2-SnO_2 were verified to be 12, 15, and 22 at an optimized temperature of 350 °C, respectively (Figure 13d). Through the structural change of SnO_2 NPs, it was found that the nanosheet-assembled nanoflower structure, which is the easiest building block for adsorbing gas species, was most advantageous among the samples. In addition, they confirmed that the lower responses of 0-SnO_2, than those of 1-SnO_2 and 2-SnO_2, were attributed to the close-packed structures that were caused during the deposition of sensing materials on a sensor substrate. The responses of the samples in vacuum were also measured to elucidate the effect of adsorbed oxygen species on H_2 sensing. Interestingly, the H_2 responses of the samples in vacuum were higher than those in air (Figure 13f). The traces of sensors responses in air and vacuum are shown in Figure 13e,g, respectively. The first-principle calculations on both cases displayed that more electrons in the vacuum condition could be directly transferred from H_2 molecules to SnO_2 surfaces, without adsorbed oxygen species as a bridge for charge transfer. From these results, H_2 molecules can interact with not only adsorbed oxygen species from the air but also with the SnO_2 surfaces directly in the absence of oxygen.

1D SMO-Based Nanostructures. The 1D nanostructures, such as nanofibers,[107−109] nanowires,[110−113] and nanotubes,[114,115] have attracted attention due to their high surface to volume ratios and high porosity. In particular, 1D structures have numerous interpores between 1D structures in their percolation network, which can enhance surface reactions of gas molecules effectively. For instance, Ab Kadir *et al.*[107] investigated the morphology effect of 1D nanostructures on H_2 sensing. They synthesized SnO_2 nanofibers having different shapes by adjusting the amounts of polyacrylonitrile in electrospinning solutions. The sensing properties of SnO_2 nanofibers were evaluated to various H_2 concentrations at 150 °C. As a result, the highest sensing performances, in terms of responses and response times, were observed in the sensors using nanofibers having the smallest diameter and hollow tubular structures among the various 1D structures. This improvement was ascribed to the enhanced active surface area because both the inner and outer surfaces of the hollow nanofibers can participate in gas sensing reactions.

2D SMO-Based Nanostructures. The 2D nanostructures of SMOs, such as nanofilms[116−118] and nanosheets,[119] have been utilized for gas sensors because they provide a high surface area to volume ratio and numerous active sites for surface reactions due to their large lateral size with ultrathin thickness. For example, PdO nanoflakes were synthesized on a SiO_2 substrate by reactive sputtering deposition (Figure 14a),[84] and they displayed efficient H_2 sensing properties. The thickness of the PdO nanoflakes was verified to smaller than 15 nm. As shown in Figure 14b,c, the current levels of the sensors were quickly decreased upon H_2 exposure and were recovered in air. The sensing speed of the sensors at 150 °C was faster than that at 100 °C. Metallic Pd nanoislands were formed on the PdO nanoflakes under H_2 exposures at 100 °C, inducing the charge transfers between Pd nanoislands and PdO substrates (Figure 14d,e). The vertically grown 2D PdO nanoflake structures facilitate these reactions, exhibiting enhanced H_2 sensing properties.

3D and Hierarchical SMO-Based Nanostructures. The 3D nanostructures, including nanosponges,[120] nanoclusters (NCs),[83,121] and the hierarchical nanostructures assembled by the fusion of the 0D, 1D, and 2D structures, such as nanourchin,[122] nanoflower,[106,123] and nanopushpin,[124] have high specific surface areas and numerous micro/mesopores, which can enhance the response and response/recovery speed. For example, secondary NCs that consisted of indium oxide

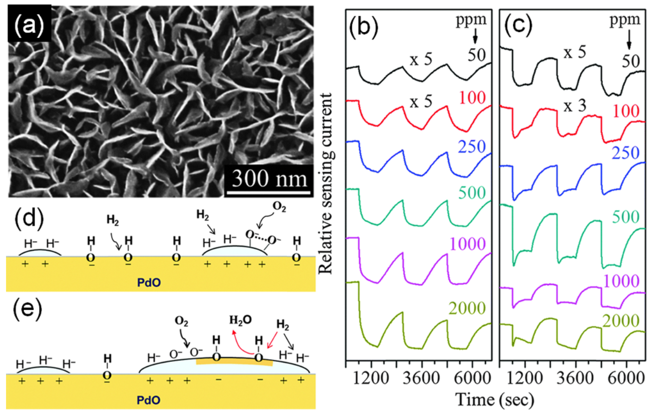

Figure 14. (a) SEM image of the PdO nanoflake thin film. The cyclic sensing response of the PdO thin film exposed to the H_2 gas mixture of different H_2 concentrations at (b) 100 °C and (c) 150 °C. Relative sensing current was defined as I/I_0. Schematic illustration of (d) hydrogen and oxygen adsorption on small Pd nanoislands formed on the PdO sensor during the H_2 exposure, and (e) reoxidation of a large Pd nanoisland as a result of dissociative oxygen adsorption. The dashed line between the two oxygen adatoms shown in (d) indicates that oxygen is molecularly adsorbed on the small Pd nanoisland. Reprinted with permission from ref 84. Copyright 2015 Royal Society of Chemistry.

(In_2O_3) nanopowders (In_2O_3 NCs) exhibited ultrafast H_2 sensing properties.[83] The In_2O_3 NCs were prepared by a two-step process: (1) the hydrothermal synthesis of indium hydroxide ($In[OH]_3$) nanopowders and (2) the subsequent calcination of $In(OH)_3$ nanopowders at 500 °C. The size of the In_2O_3 NCs consisting of ultrasmall nanopowders (∼30 nm) was verified to about 200 nm, and there were numerous mesopores in their structures. The sensors showed a high H_2 response (R_a/R_g = 18 to H_2 500 ppm) at 260 °C, with an ultralow H_2 detection limit of 100 ppb. In addition, the sensors exhibited a very fast response/recovery time (∼2 s) to 500 ppm of H_2. The large specific surface areas and high porosity of the 3D In_2O_3 not only promoted surface reactions but also prevented the agglomeration of nanopowders, leading to the significantly enhanced sensing properties.

In addition to 3D structures, the influence of hierarchical structures on H_2 sensing properties was investigated by Voranti *et al.*[94] They prepared three types of CuO nanostructures that resemble urchins, fibers, and nanorods. The gas responses of different CuO nanostructures were measured as a function of $[H_2]$ at an operating temperature of 200 °C, and the CuO urchins showed the highest H_2 responses among the samples. The urchin-like structure has a high surface to volume ratio than other structures (fibers and nanorods) as well as high porosity between interparticles, thereby showing the highest sensing responses among the samples.[94]

For the commercialization, the operating temperature of SMO-based H_2 sensors should be lowered to reduce power consumption. However, gas sensing properties of SMO-based H_2 sensors operated at low temperatures (<100 °C) are much lower compared to the sensors operated at high temperatures.[125,126] Because SMOs have a wide bandgap (>2.0 eV) generally, it is difficult to modulate electrons in SMOs at low operating temperatures. However, the modification of SMO structures can realize the low-temperature operation for H_2 sensing.[85,126−132] For example, ordered mesoporous TiO_2 structures exhibited H_2 sensing properties at RT.[129] The

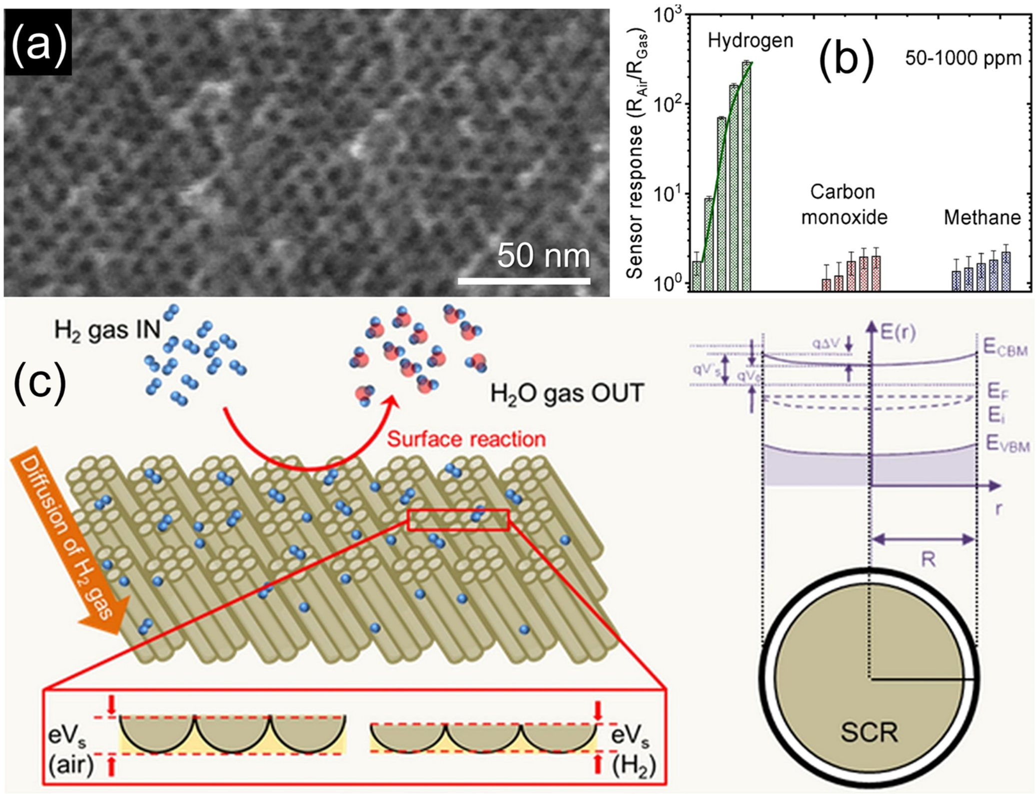

Figure 15. (a) TEM image of the surface of ordered mesoporous TiO_2 (OMT). (b) The selectivity of the OMT sensor to H_2 against carbon monoxide and methane gas. (c) The schematic illustration of the proposed sensing mechanism. (SCR: screen charge region) Reproduced with permission from ref 129. Copyright 2020 Elsevier.

evaporation-induced self-assembly method produced well-assembled TiO_2 with uniform mesopores with an average diameter of ~3 ± 0.5 nm (Figure 15a). Interestingly, ordered mesoporous TiO_2 exhibited sufficient resistances (~2 GΩ) at RT due to numerous defects on the TiO_2 surface and were able to detect H_2 at RT in air, with high response (R_a/R_g = 289 to 1000 ppm) and fast response (85 s) and recovery time (198 s). In addition, the sensors exhibited good selectivity against other interfering gases (carbon monoxide [CO] and methane [CH_4]) (Figure 15b). These interesting sensing properties can be explained by the small grain size, high surface area, and intergranular surface potential (Figure 15c). Highly ordered mesoporous TiO_2 not only provided abundant available active sites but also offered a multitude of channels (about 50,000 channels) for fast gas diffusion. When the material is exposed to H_2, the L (below 1 nm) is fully formed along the pore walls (thickness: 2 nm) due to the easy diffusion of H_2 into inner walls through nanochannels. Consequently, the H_2 reaction with preadsorbed oxygen significantly increases the surface density of electrons and lowers the surface potential barrier, thereby exhibiting low resistances at RT in air. From these results, they concluded that SMO-based H_2 sensors operated at RT can be designed by (1) controlling the morphology to facilitate H_2 diffusion, (2) increasing surface active sites for H_2 adsorption, and (3) reducing grain sizes of SMO for the effective modulation of potential barriers for charge transports.

In this section, we discuss the morphologies of pure SMOs based on the effect of (1) electron depletion layer/hole accumulation layers and (2) the grain boundary barriers on H_2 sensing. The gas sensing performance of pure SMO-based H_2 sensors can be improved by modifying the structure, which is meso- and microporous and has a large specific surface area, as a result of lowering the barrier and increasing the electron transfer speed. However, in spite of these advances, pure SMO-based H_2 sensors often displayed low H_2 response and poor selectivity against other interfering gas molecules. In particular, selectivity is one of the critical issues in SMO-based sensors due to their inherent sensing mechanisms. SMO-based sensors are operated by chemical reactions between chemisorbed oxygen species and analytes, inferring molecules can react with adsorbed oxygen instead of H_2. Hence, other methods such as the use of catalysts and the combination with other materials have been introduced to improve gas sensing properties of the SMO-based gas sensor, as discussed in the next section.

Catalyst/SMO-Based Materials. *Catalytic Effect of Metal NPs on SMO-Based Sensors.* The functionalization of catalytic noble metal NPs, such as Pd,[133,134] Pt,[135,136] Ag,[137] and Au,[138,139] on SMOs is the most powerful way to enhance the response and selectivity of chemical sensors. In general, the catalytic effect of metal NPs on SMO-based gas sensors can be explained by (1) chemical sensitization (*e.g.*, Pt, Au, and Ru) and (2) electronic sensitization (*e.g.*, Pd, Ag, and Cu).[140] The chemical sensitization is used to describe processes wherein gas molecules are dissociated by metal NPs and then spill over to the surface of SMOs. Therefore, H_2 reactions on the surface of SMOs are effectively promoted by catalytic metal NPs, thereby enhancing H_2 sensing properties. The electronic sensitization is related to the change in the oxidation state of catalytic metal NPs upon gas exposures. Electronic sensitizers on SMOs are partially oxidized when exposed to air, forming metal (or metal oxide)/SMO heterojunctions that induce electron depletion layers (for n-type SMOs). Then, they are reduced by the

https://dx.doi.org/10.1021/acsnano.0c05307
ACS Nano 2020, 14, 14284−14322

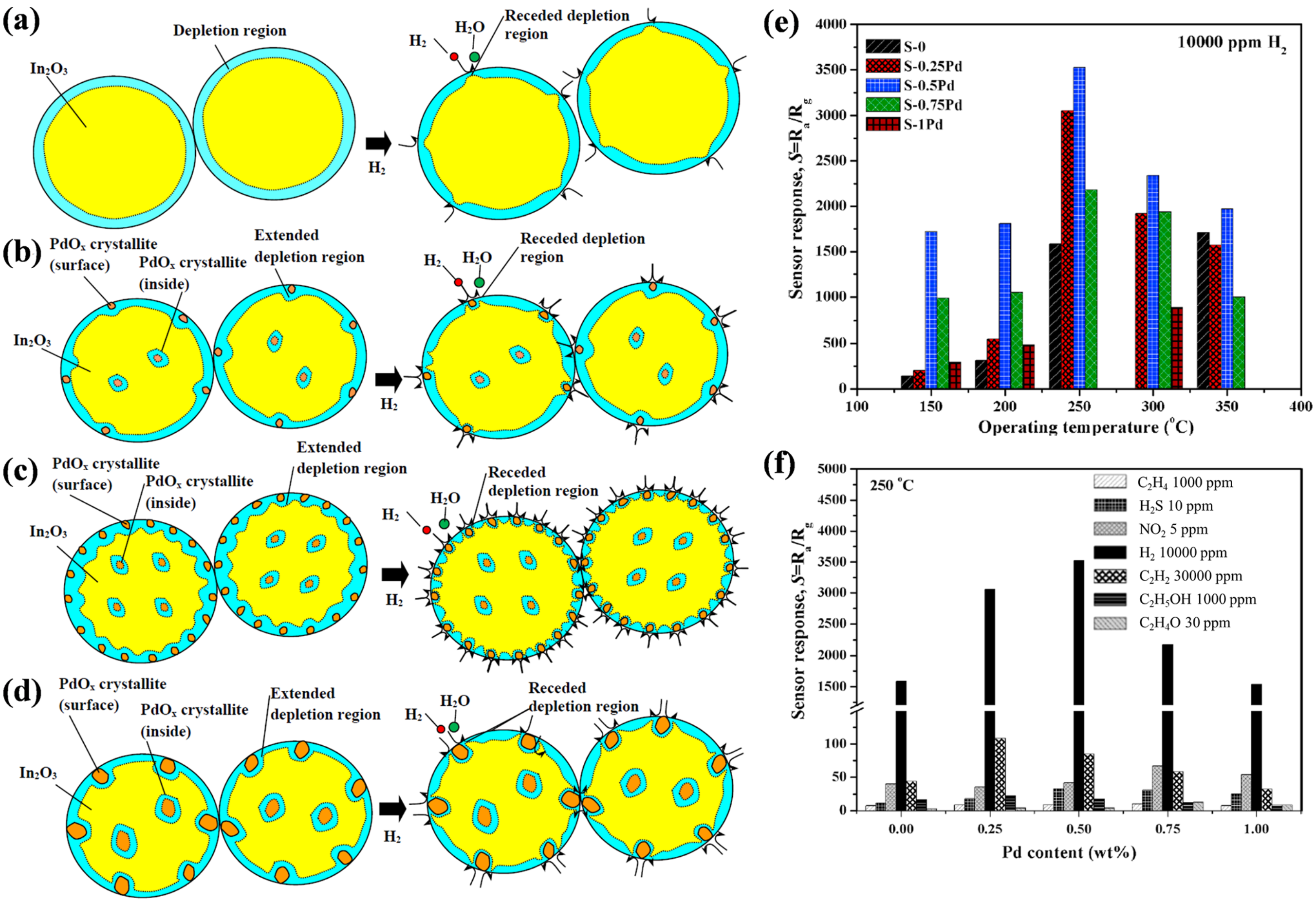

Figure 16. Schematic illustrations for H_2 sensing mechanisms of (a) pristine In_2O_3 NPs, and (b−d) In_2O_3 NPs with PdO_x doping at (b) low, (c) moderate, and (d) high PdO_x concentrations. (e) Responses of the sensors to H_2 1% with different PdO_x concentrations (0, 0.25, 0.50, 0.75, and 1 wt %) at various operating temperatures (150−350 °C). (f) Selectivity of PdO_x-doped In_2O_3 to 1000 ppm of C_2H_4, 10 ppm of H_2S, 5 ppm of NO_2, 1% H_2, 3% C_2H_2, 1000 ppm of C_2H_5OH, and 30 ppm of C_2H_4O at the operating temperatures of 250 °C. Reprinted with permission from ref 152. Copyright 2019 Elsevier.

reactions with reducing gases (*e.g.*, H_2) and give electrons back to SMOs. Therefore, upon gas exposures, the electron depletion layers of SMOs become thinner, resulting in significant changes in resistances.[140,141] From these reasons, catalytic NPs can effectively improve the performance of SMOs-based sensors.

For H_2 sensing, among various catalysts, Pt and Pd are well-known chemical sensitizers due to their excellent ability to induce the spillover effect of H_2 molecules onto supports.[82,142] PdO_x is also frequently utilized as an electronic sensitizer for SMO-based H_2 sensors owing to their high reactivity with H_2.[143] For instance, Wang *et al.*[144] demonstrated that Pt and Pd are more effective catalysts for SMO-based H_2 sensors than other metallic NPs. They synthesized various metal catalysts, including Pt, Pd, Au, Ag, Ti, and Ni, loaded on ZnO nanorods, and investigated their H_2 sensing properties. Among them, Pt-loaded ZnO nanorods and Pd-loaded ZnO nanorods showed highly sensitive and fast sensing properties to H_2 at RT. In addition, Li *et al.*[145] demonstrated the H_2 spillover over Pt/TiO_2 using temperature-programmed desorption and reduction, and Tsang *et al.*[146] observed that Pd NPs induced the spillover of H atoms onto the surface of SnO_2. Furthermore, Lupan *et al.*[143] reported that the functionalization of PdO/PdO_2 catalysts improved the H_2 sensing properties of ZnO film-based sensors at low operating temperatures, due to the formation of PdH_x upon H_2 exposures. Therefore, diverse SMOs, including SnO_2,[147] WO_3,[148] ZnO[149] and MnO_2,[134] functionalized by Pt, Pd, or PdO_x, have been reported for selective H_2 sensing layers so far.

Effects of Size and Distribution of Catalytic Metal NPs. The size and distribution of catalytic metal NPs on SMOs have influence on the H_2 sensing performances of SMO-based sensors.[150,151] For instance, Inyawilert *et al.*[152] investigated the effect of size and distribution of PdO_x on H_2 sensing properties of In_2O_3-based sensors. In the case of pristine In_2O_3 NPs, H_2 can only react with adsorbed oxygens at a limited number of active sites on In_2O_3 surface, showing low responses (Figure 16a). On the other hand, in the case of PdO_x-doped In_2O_3 NPs, PdO_x induces the spillover effect of H_2 and O_2 on In_2O_3, resulting in enhanced sensing properties. In addition, the heterojunction is formed between p-type PdO_x and n-type In_2O_3, leading to the formation of additional depletion regions (Figure 16b−d). However, when the loading amount of PdO_x was too high, the PdO_x particles were aggregated into larger crystallites, lowering the catalytic effect of PdO_x as well as response to H_2 (Figure 16d). Therefore, there were optimum loading amounts of PdO_x (0.5 wt % PdO_x-doped In_2O_3) for H_2 sensing properties (R_a/R_g = 3526 for 1% [H_2] 250 °C) (Figure 16e). In addition, PdO_x doping significantly enhanced H_2 responses against other interfering gases (Figure 16f). From

https://dx.doi.org/10.1021/acsnano.0c05307
ACS Nano 2020, 14, 14284−14322

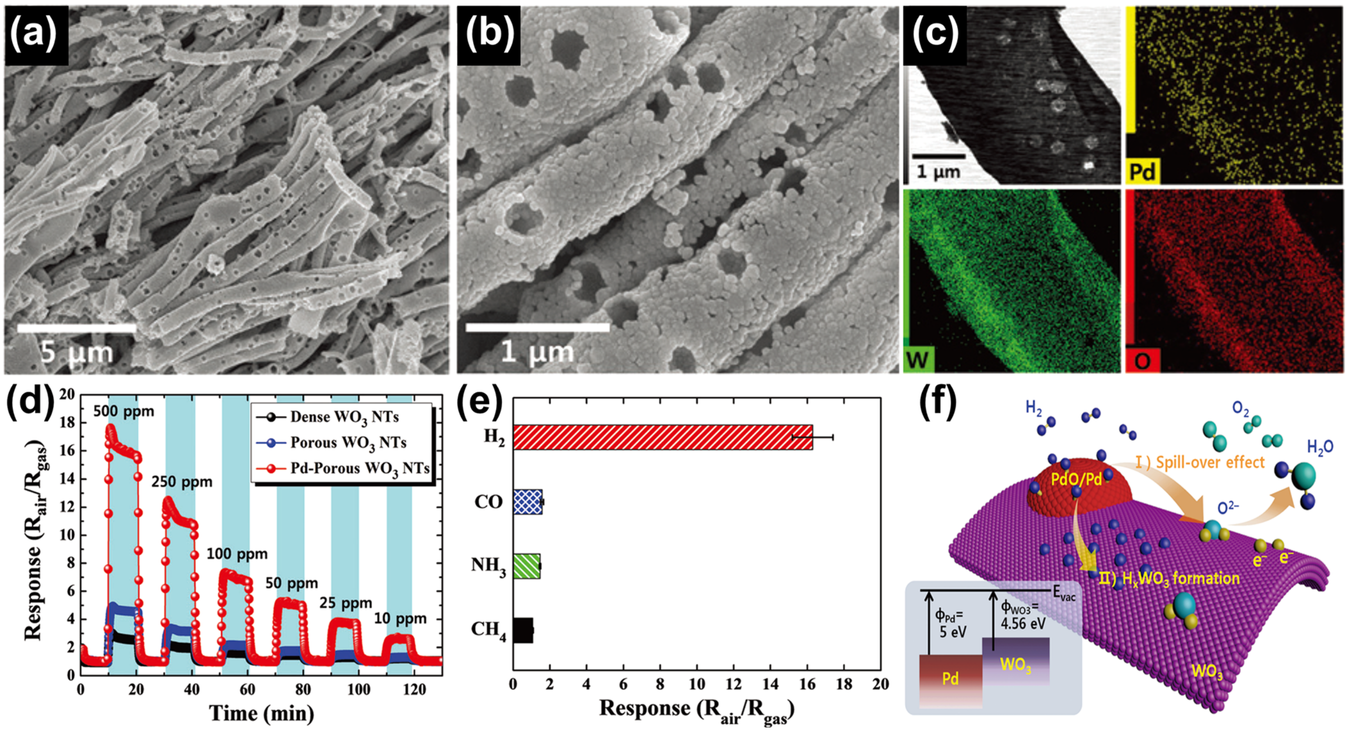

Figure 17. (a) SEM images of Pd-loaded macroporous WO_3 nanotubes (NTs) and (b) magnified SEM image of (a). (c) Scanning TEM image with energy dispersive X-ray spectroscopy (EDS) mapping images of Pd-loaded macroporous WO_3 NTs. (d) Dynamic signal responses of dense WO_3 NTs, porous WO_3 NTs, and Pd-loaded porous WO_3 NTs in the range of H_2 10−50 ppm. (e) Selectivity of Pd-loaded porous WO_3 NTs against other analytes (50 ppm). (f) Schematic illustration of H_2 sensing mechanism of Pd-loaded porous WO_3 NTs. Reprinted with permission from ref 154. Copyright 2016 The Royal Society of Chemistry.

these results, the use of catalysts for improved SMO-based H_2 sensors is essential in terms of two main factors:[133,153] (1) the functionalization of ultrasmall catalytic NPs and (2) the uniform distribution of catalytic NPs.

Design of Catalyst/SMO-Based Nanostructures. The improvement of H_2 sensing characteristics can be achieved by the design of nanostructures of catalyst-functionalized SMOs. For example, Choi *et al.*[154] demonstrated that macroporous tungsten trioxide (WO_3) nanotubes (NTs) functionalized by ultrasmall Pd NPs exhibited high H_2 sensing performances. The apoferritin template, which is a protein with a small cavity size (∼8 nm),[155−158] was used to synthesize ultrasmall (∼2 nm) Pd NPs. The macroporous WO_3 NTs were synthesized using a coaxial electrospinning technique (Figure 17a,b), and the ultrasmall Pd NPs were uniformly distributed to the macroporous WO_3 NTs (Figure 17c). The Pd-loaded macroporous WO_3 NTs exhibited a high response (R_{air}/R_{gas} = 17.6) to 500 ppm of H_2, which was a 5.9- and 3.6-fold enhanced response compared to dense WO_3 NTs and macroporous WO_3 NTs (Figure 17d)v and superior H_2 selectivity against other interfering analytes (Figure 17e). The improved sensing properties were attributed to the ultrasmall Pd NPs on the macroporous WO_3 NTs. The Pd NPs generate the Schottky barrier with WO_3 due to the difference in work function (5 eV for Pd NPs and 4.56 eV for WO_3)[159,160] and are partially oxidized to PdO (p-type SMO) that induces a p−n junction with WO_3 (Figure 17f). In addition, Pd NPs dissociate the H_2 molecules into H atoms (H_{ads}), and allow H_{ads} to diffuse into the surface of the WO_3. The diffused H_{ads} can react with chemisorbed oxygen species on WO_3, resulting in the production of H_2O molecules[29,161] or the formation of hydrogen tungsten bronzes (H_xWO_3).[162] The macroporous NT structures also offer numerous surface reaction sites, promoting the catalytic effect of Pd NPs. Therefore, the deposition of Pd NPs onto porous WO_3 improved the H_2 sensing performance. Similarly, Zhou *et al.*[163] reported Pd-loaded urchin-like $W_{18}O_{49}$ nanospheres as a highly sensitive H_2 sensing layer. The urchin-like $W_{18}O_{49}$ nanospheres which are assembled with numerous nanorods have large surface areas and plenty of oxygen vacancies. In addition, Pd NPs on urchin-like $W_{18}O_{49}$ nanospheres allow to exhibit high response and selectivity to H_2 at low temperatures. From this perspective, diverse catalytic NP/SMO-based nanostructures have been reported as highly sensitive and selective H_2 sensing layers.[134−136,149,162,164]

SMO-Based Composites. In addition to functionalization of catalytic NPs on SMOs, composites of (1) multicomponent SMOs,[23,165] (2) SMO and graphene/graphene derivatives,[166−169] and (3) SMOs and gas selective membranes[170] can improve H_2 sensing properties due to their synergistic effects. The formation of heterojunction interfaces by incorporating two or more SMOs and graphene/its derivatives can affect the sensing properties by changing physical or chemical properties of SMO-based composites, such as Fermi level equilibration, charge carrier separation, and depletion layer manipulation.[171−173] In addition, the presence of different SMOs suppresses the grain growth of host SMOs during high-temperature calcination, which are usually accompanied for synthetic methods, resulting in a smaller grain size with large surface area.[174−176] These effects significantly enhance sensing performances, in terms of response and selectivity.

Multicomponent SMO-Based Composites. To develop efficient H_2 sensors, various multicomponent SMOs, such as

https://dx.doi.org/10.1021/acsnano.0c05307
ACS Nano 2020, 14, 14284−14322

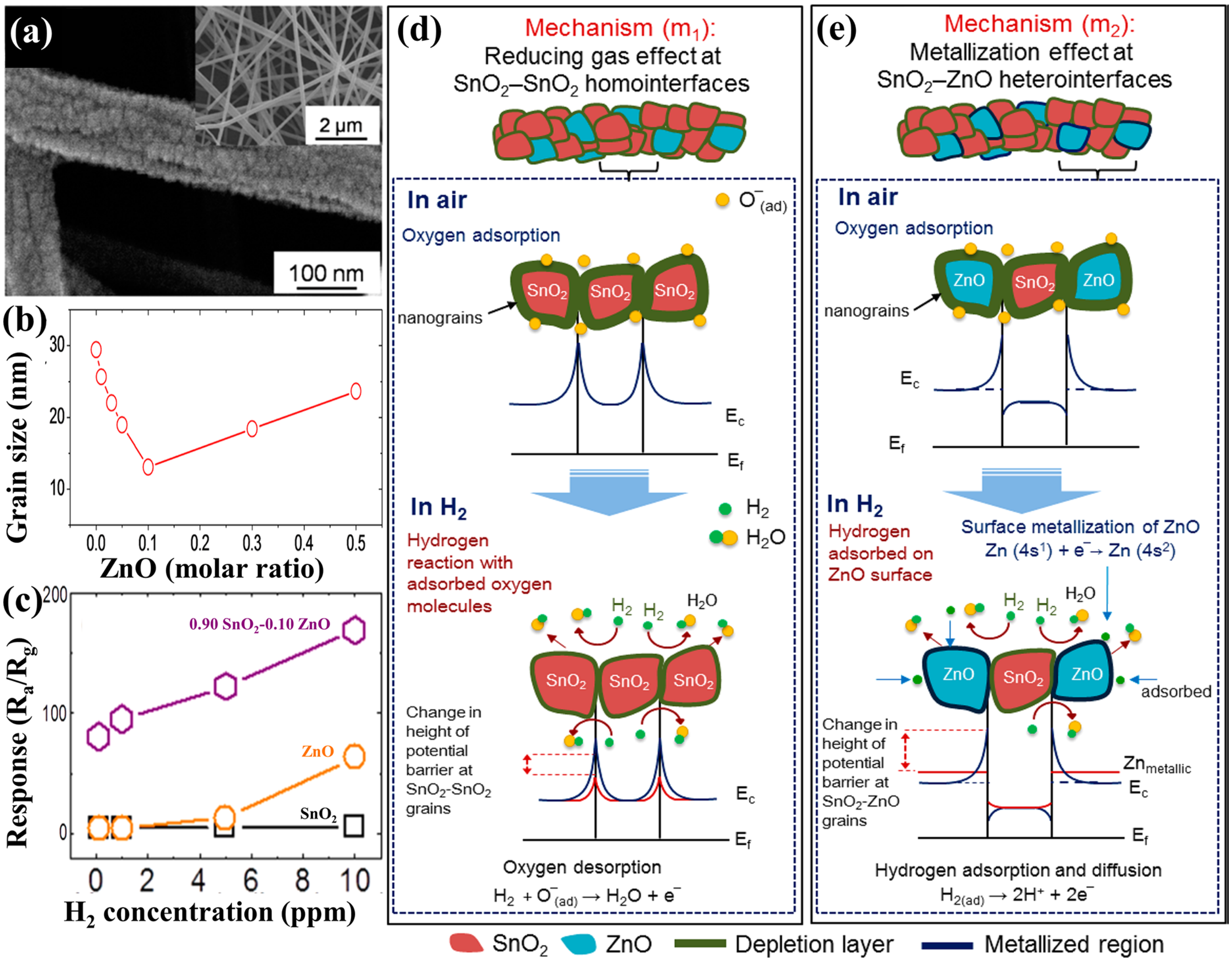

Figure 18. (a) SEM images of 0.90 SnO_2/0.10 ZnO composite nanofibers (NFs), (b) grain size of the different NFs, and (c) responses of the pristine ZnO, pristine SnO_2, and SnO_2/ZnO composite NFs with varying H_2 concentrations. Schematic diagram of the proposed bifunctional sensing mechanism, explaining the enhanced sensitivity of the SnO_2/ZnO composite NFs to H_2. (d) Mechanism (m_1): reducing gas effect at SnO_2−SnO_2 homointerfaces and (e) mechanism (m_2): metallization effect at SnO_2/ZnO heterointerfaces. Reprinted with permission from ref 184. Copyright 2015 American Chemical Society.

SnO_2/La_2O_3,[177] Pt-MoO_3/La_2O_3,[178] TiO_2/WO_3,[179] CuO/ZnO,[180] SnO_2/Co_3O_4,[181] SnO_2/TiO_2,[182] and SnO_2/ZnO,[183,184] were reported. For instance, Katoch *et al.*[184] demonstrated that the SnO_2/ZnO composite NFs exhibited much improved H_2 sensing characteristics than those of pristine SnO_2 NFs and ZnO NFs. The SnO_2/ZnO composite NFs were synthesized using electrospinning and subsequent calcination (Figure 18a). As the molar ratio of ZnO to SnO_2 was increased from 0 to 0.1 in the SnO_2/ZnO NFs, the grain size of the SnO_2/ZnO NFs was decreased from 30 to 13 nm. Although the grain size was increased when the moral ratio of ZnO to SnO_2 was over 0.1, the grain size (<25 nm) of the SnO_2/ZnO composite NFs is smaller than that (*ca.* 30 nm) of the pristine SnO_2 NFs (Figure 18b). This smaller grain size of the composite NFs is attributed to that the ZnO can act as a grain growth inhibitor to SnO_2/ZnO composite NFs. In terms of sensing properties, the 0.90SnO_2-0.10ZnO (the numbers indicate the molar ratio) composite NFs exhibited the highest response (R_{air}/R_{gas} = 168.6) to 10 ppm of H_2 (Figure 18c) compared to those of pristine SnO_2 NFs (R_{air}/R_{gas} = 4.2) and pristine ZnO NFs (R_{air}/R_{gas} = 63.8). The authors explained that the improved sensing properties were attributed to (1) the small grain size of the composite NFs and (2) the metallization effect of ZnO. The smaller grains of the SnO_2/ZnO NFs induce more potential barriers between the neighboring nanograins, resulting in huge resistance changes upon H_2 exposure (Figure 18d). In addition, the metallization of ZnO occurs by the adsorption of H atoms on O sites of ZnO by forming a strong hybridization between s-orbitals of H and p-orbitals of O.[98,185] The charge delocalization occurs between Zn and O−H bonds due to strong hybridization and causes the metallization of the surface Zn atoms, where the 4s and 3d orbitals of Zn contribute to the electrical conduction. In the case of SnO_2/ZnO composites, numerous heterojunctions between ZnO and SnO_2 grains were created due to the difference in work function (5.2 eV for ZnO and 4.9 eV for SnO_2)[186,187] in air. However, since semiconducting ZnO was transformed into metallic Zn by the metallization effect when exposed to H_2, the height of potential barriers between ZnO and SnO_2 was changed significantly (mechanism m2, Figure 18e). In addition, the metallization causes the electron transfer from metallic Zn to SnO_2, thereby reducing the resistance of

https://dx.doi.org/10.1021/acsnano.0c05307
ACS Nano 2020, 14, 14284−14322

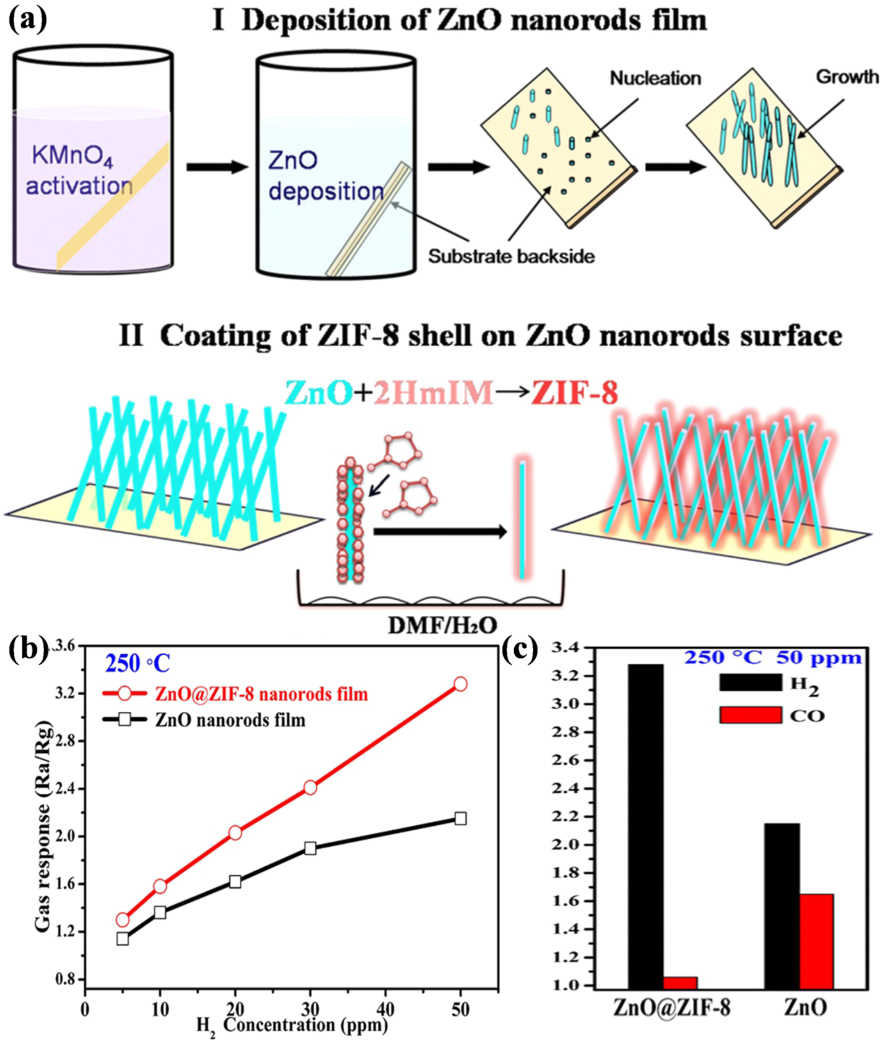

Figure 19. (a) Schematic illustration of the formation of ZnO@ZIF-8 core−shell nanorod (NR) films. (b) H_2 responses of ZnO NRs and ZnO@ZIF-8 NRs at 250 °C. (c) Comparison of responses of ZnO NRs and ZnO@ZIF-8 NRs to H_2 and CO at 250 °C. Reprinted with permission from ref 199. Copyright 2017 Wiley-VCH.

the composites. When the SnO_2/ZnO composite NFs were exposed to ambient air, the metallic Zn was transformed to semiconducting ZnO, and the resistances of the composites were recovered to their original value. Therefore, the formation of SnO_2/ZnO composites NFs effectively improved the H_2 response with high selectivity. Likewise, to achieve highly sensitive and selective sensing layers, the formation of composite with SMO and graphene/its derivation such as ZnO NTs/graphene,[188] TiO_2 NTs/rGO,[189] SnO_2 NPs/graphene,[161] and MoO_3 nanoribbon/graphene[190] were reported. The graphene/its derivation can construct the heterojunctions at the interface between SMOs and offer higher interactions with analytes due to the presence of defects and functional groups.[191−193]

SMO/Membrane-Based Composites. The introduction of selective sieving layers on SMOs is one of the most promising solutions to achieve high selectivity to H_2. As a typical sieving layer, metal−organic frameworks (MOFs), which consist of metal nodes and organic linkers, enable the selective penetration of H_2 molecules compared to other molecules, due to its highly porous structures and well-defined pore structures.[194,195] A notable example is utilizing the zeolitic imidazolate frameworks-8 (ZIF-8), where formula is $Zn(mim)_2$ (mim = 2-methylimidazolate). Since the pore size of ZIF-8 is about 3.4 Å, the ZIF-8 can separate H_2 molecules (kinetic diameter: ∼2.89 Å) from larger interfering molecules (>3.4 Å).[170,196] To utilize these properties, Drobek *et al.*[197] synthesized ZIF-8-coated ZnO nanowires (NWs) (ZnO@ZIF-8 NWs) for selective H_2 sensing layers. The pristine ZnO NWs without the ZIF-8 layer exhibited noticeable responses to H_2, toluene (C_7H_8), and benzene (C_6H_6). On the other hand, the ZnO@ZIF-8 NWs showed a highly selective response only to H_2 while showing negligible cross-responses to other interfering gases with large kinetic diameters [C_7H_8 (5.92 Å) and C_6H_6 (5.27 Å)]. Similarly, Ji *et al.*[198] reported selective H_2 sensors using a ZnO@ZIF-8 core−shell structure. In addition, Wu *et al.*[199] investigated the H_2 sensing characteristics of ZnO@ZIF-8 core−shell nanorods (NRs), which is the ZIF-8-deposited ZnO NRs (Figure 19a). ZnO NRs were partially dissolved in the mixed solvent of H_2O/DMF with Zn precursors and 2-methylimidazole, in order to fabricate the uniform and continuous ZIF-8 shells (thickness: 110 nm) on the ZnO NRs. In addition, the defect states of the ZnO@ZIF-8 NRs and pristine ZnO NRs were characterized by photoluminescence (PL) spectroscopy. The sharp emission at 378 nm was ascribed to the recombination of excitons in ZnO,[200]

Table 2. Summary of Sensing Properties of SMO-Based Composites for H_2 Sensors[a]

morphology	material	operating temperature	response @ $[H_2]$	τ_{resp}/τ_{rec}[b]	detection limit ($[H_2]$)	ref
honeycomb	SnO_2	340 °C	8.4 @1 ppm	4 s/10 s	0.05 ppm	121
nanohexagone	ZnO	175 °C	1.089 @10 ppm	11.5 s/14.5 s	200 ppb	119
film	TiO_2	RT	250 @4 ppm	55 s/n.r.	1 ppm	126
nanocluster	In_2O_3	400 °C	18 @500 ppm	1.7 s/1.5 s	10 ppb	83
nanourchin	WO_3	250 °C	~4 @50 ppm	n.r.	n.r.	122
hollow nanosphere	V_2O_5	RT	~2.8[d] @200 ppm	30 s/5 s	n.r.	131
nanoribbon	MoO_3	RT	~0.85 @500 ppm	21 s/69 s	500 ppb	132
nanotube	Fe_2O_3	200 °C	2.3 @50 ppm	n.r.	n.r.	115
nanoflake	PdO	200 °C	1.9 @250 ppm	n.r.	n.r.	84
nanosheet	NiO	250 °C	191 %[d] @150 ppm	150 s/n.r.	10 ppm	90
nanoflake	MnO_2	200 °C	12.3[e] @500 ppm	<10 s/n.r.	150 ppb	93
nanourchin	CuO	200 °C	9 @500 ppm	2.5 min/n.r.	n.r.	94
nanofibers	Pd-loaded SnO_2	160 °C	36.14 @1000 ppm	4 s/3 s	20 ppm	153
nanoplates	Pd-WO_3	80 °C	169.3 @0.1 vol%	42.8 s/48.5 s	0.05 vol%	162
nanowalls	Pd-MnO_2	100 °C	11.4 @100 ppm	4 s/n.r.	10 ppm	134
nanowires	Pt-PdO	RT	23%[d] @100 ppm	166 s/445 s @ 0.1%	10 ppm	135
nanorods	Pd-ZnO	135 °C	22.5 @250 ppm	1 s/52 s	50 ppm	149
nanowires	Pd-SnO_2	300 °C	27.84 @100 ppm	n.r.	1 ppm	133
nanofibers	Pd-WO_3	450 °C	16.3 @500 ppm	n.r.	10 ppm	154
urchin-like spheres	Pd−$W_{18}O_{49}$	100 °C	1600 @0.1 vol%	60 s/4 s @ 0.05 vol%	250 ppm	163
nanofibers	SnO_2/ZnO	300 °C	168.6 @10 ppm	n.r.	0.1 ppm	184
nanoparticles	Co_3O_4/SnO_2	300 °C	27%[d] @50 ppm	n.r.	5 ppm	206
nanorods	ZnO-modified SnO_2	350 °C	18.4 @100 ppm	n.r.	10 ppm	183
particles	Au-SnO_2/Co_3O_4	250 °C	9100 @1000 ppm	n.r.	n.r.	139
nanowires	ZnO@ZIF-8	300 °C	1.44 @50 ppm	n.r.	10 ppm	197
nanorods	ZnO@ZIF-8	250 °C	3.28 @50 ppm	n.r.	5 ppm	199

[a]n.r. indicates not reported, and RT is room temperature. [b]τ_{resp} is the time necessary for the resistance to increase from R_0 to the $0.9\Delta R_{max}$, and τ_{rec} is the time for the resistance to decrease from ΔR_{max} to $0.1R_0$. [c]Response is defined as R_{air}/R_{gas}. [d]Value means that response is defined as sensitivity $(R_{gas} - R_{air})/R_{air} \times 100\%$. [e]Value means that response is defined as I_g/I_a.

and the broad emission in the range of 470−650 nm was attributed to oxygen-related defects such as oxygen vacancy and interstitial oxygen.[201,202] In PL spectra, the ZnO@ZIF-8 NRs have more oxygen defects than pristine ZnO NRs, and these oxygen defects can promote the H_2 reactions. It is noted that the oxygen defects resulted from the etching of surface oxygen in ZnO NRs during the formation of the ZIF-8 shell. The ZnO@ZIF-8 NRs exhibited an enhanced H_2 response (R_{air}/R_{gas} = 3.28 to H_2 50 ppm), compared to that of pristine ZnO NRs (R_{air}/R_{gas} = 2.15) (Figure 19b). In addition, the ZnO@ZIF-8 NRs have a superior H_2 selectivity than the pristine ZnO NRs (Figure 19c) due to the molecular sieving effect of ZIF-8 layers.[203,204] Considering that MOFs have various structures and pore sizes with high tunability,[14,205] the use of MOFs as molecular sieving layers for SMO-based H_2 sensors is one of the most promising methods to improve H_2 selectivity.

Challenges of SMO-Based H_2 Sensors. So far, there were various approaches, such as the synthesis of nanostructures, the functionalization of catalysts on SMOs, and the composites with other materials, to improve SMO-based H_2 sensors. Table 2 summarizes the sensing characteristics of recently reported SMO-based H_2 sensors.[83,90,93,94,115,119,121,122,126,131−135,139,149,153,154,162,163,183,184,197,199,206] Definitely, SMO-based H_2 sensors have high response, fast response speed, and reasonably high stability, however, they still have some challenges. The H_2 selectivity of SMO-based sensors is poor due to their high-temperature operation. At high operating temperatures, other gas molecules are also able to react with SMOs and induce resistance changes. Therefore, the development of several SMO-based sensor arrays is needed to achieve excellent selectivity. In addition, the high operating temperature is accompanied by high-power consumption, which hinders the practical use of SMO-based sensors in various applications. Lastly, the sensing properties of SMO-based sensors are highly vulnerable to humidity. Therefore, they should be protected from humidity, or the reliability of the sensors should be proven for a wide range of humidity.

CARBON-BASED MATERIALS

Carbon-based materials, including CNTs and graphenes, have emerged as one of the most ideal chemiresistors due to their operation at ambient temperatures, tunable electrical properties, and chemical functionalization.[207] In particular, the operation of carbon-based materials at low temperatures enables the detection of gas molecules based on (1) their inherent reactivity with carbons and (2) molecular recognition by selectors.[208] Therefore, there have been significant advances in carbon-based chemical sensors, particularly for CNT- and graphene-based chemiresistors.[26,192,209−211] Unfortunately, most of the pure carbon-based materials have no appreciable interaction with H_2. Therefore, in order to develop carbon-based H_2 sensors, it is imperative to use catalysts (*e.g.*, metallic NPs) on carbon-based materials.[212] In addition, the tuning of the Schottky junction between electrodes and carbon materials can induce H_2 sensing properties.[213] In this section, we discuss recent advances in carbon-based H_2 sensors, by categorizing into CNTs and graphenes.

https://dx.doi.org/10.1021/acsnano.0c05307
ACS Nano 2020, 14, 14284−14322

CNT-Based Materials. *Catalyst/CNT Composites.* The majority of catalyst/CNT composites for H_2 sensors relies on the use of Pd NPs due to the distinctive reactivity of Pd to H_2, while there were a few reports on Pt/CNT composite-based H_2 sensors.[214−217] The deposition of Pd NPs on the CNT-network (Figure 20a) or individual CNT (Figure 20b) induces the chemiresistive H_2 sensing properties to CNT-based sensors. In 2001, the Dai group demonstrated Pd/CNT-based H_2 sensors.[212] They fabricated Pd-loaded single-walled CNTs (SWCNTs) by using an electron beam evaporator. The conductance of Pd/SWCNT composites was decreased in response to H_2 due to the formation of PdH_x. Because PdH_x has a lower electron affinity than Pd,[218] electrons are donated from PdH_x to CNT and lead to the compensation of electron−hole pairs in p-type SWCNTs. Since then, numerous studies on Pd/CNT-based composites for H_2 sensors were reported.[212,219−225] Various methods for Pd/CNT composites were developed to simplify the fabrication process and to improve the H_2 sensing properties. In particular, Sun *et al.*[219] demonstrated flexible H_2 sensing systems using Pd/SWCNT composites (Figure 20c−f). The transfer of the SWCNT network on polyethylene (PET) sheets and subsequent Pd clusters produced flexible H_2 sensors with efficient H_2 sensing properties. The sensors exhibited high responses (R_g/R_0 = ∼60% to 0.1% of H_2) and low detection limits (30 ppm) at RT in air (Figure 20c). They confirmed that the H_2 sensing mechanisms of the Pd/CNT composites were attributed to the formation of PdH_x (Figure 20d). The responses of the Pd/CNT composites were directly proportional to $[H_2]^{1/2}$, which is the same as the behaviors of Pd-based sensors explained by the Sievert law for the formation of α-PdH_x.[226] In addition, the sensors displayed a stable operation in bending states due to the high mechanical strength of CNTs (Figure 20e,f). The responses of the sensors to H_2 0.1% were maintained even after 1000 times of bending.

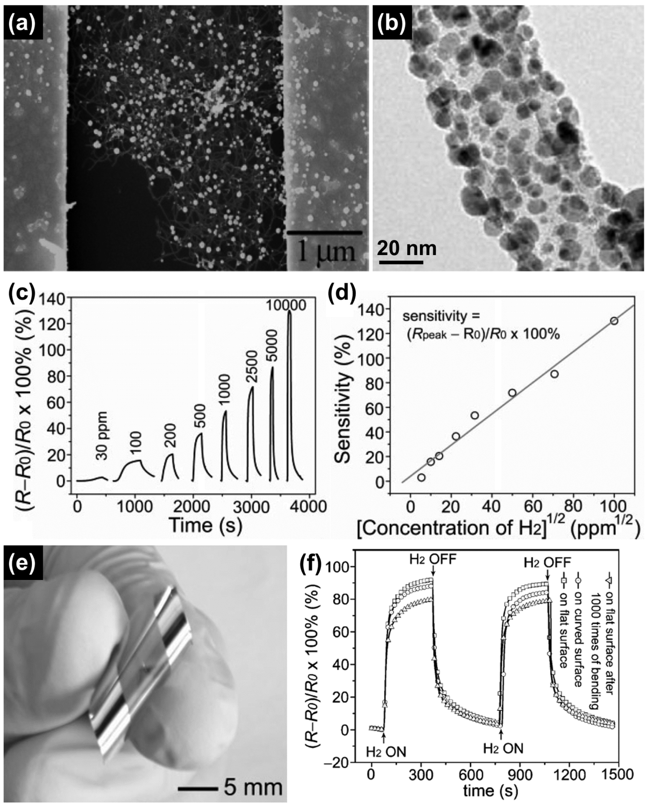

Figure 20. (a) SEM image of Pd/SWCNT composites prepared by electrodeposition. Reprinted with permission from ref 221. Copyright 2007 American Chemical Society. (b) TEM image of Pd NP-loaded CNT prepared by chemical reduction under UV light irradiation. Reprinted with permission from ref 284. Copyright 2019 Elsevier. (c) Response traces of Pd/CNT composites to H_2 exposures, ranging from 30 ppm to 1%. The sensors were operated at RT in air. (d) Sensitivity (response) of the sensors *versus* $[H_2]^{1/2}$. (e) Photograph of Pd/CNT composite-based flexible H_2 sensors. (f) The responses of the flexible H_2 sensors upon exposures of H_2 0.1% at the flat and bending states. Reprinted with permission from ref 219. Copyright 2007 Wiley-VCH.

Recently, Li *et al.*[223] investigated the size effect of Pd NPs on CNT-based H_2 sensors. They fabricated Pd-deposited CNT ropes by the dielectrophoretic deposition of CNTs (Figure 21a,b) and the subsequent electrodeposition of Pd on CNT ropes (Figure 21c,d). The pulsed electrodeposition effectively controlled the size of Pd NPs on CNTs from 4.5 to 5.8 nm with a narrow size distribution (Figure 21e). Compared to solid Pd nanowire-based H_2 sensors, the Pd/CNT composites exhibited a 30-fold higher H_2 response (20% to H_2 0.1%) at RT in air (Figure 21f), with a fast response (60 s) and recovery (72 s) speed and low detection limits (10 ppm). In addition, they revealed that there was a trade-off between responses and sensing speeds depending on the size of Pd NPs. The smaller Pd NPs deposited on CNTs are faster for H_2 sensing due to their high surface to volume ratio, but less sensitive due to the low coverage of Pd NPs on CNTs.

Schottky Contact-Based CNT Sensors. In CNT-based H_2 sensors, in addition to the charge transfer mechanisms relying on the formation of PdH_x, there are Schottky contact-based H_2 sensors. The Schottky contact-based CNT sensors rely upon the modulation of the potential barrier at the interfaces between electrodes and CNTs induced by gas exposure. In this regard, Javey *et al.*[213] demonstrated the Schottky contact-based H_2 sensors by using SWCNTs and Pd electrodes. Semiconducting SWCNTs were contacted with metallic Pd electrodes of back gate field-effect transistors (FETs) (Figure 22a), and they exhibited an ohmic contact behavior at the "on" state that is closed to ballistic transport. Then, upon H_2 exposure, Pd electrodes were transformed into PdH_x that has lower work functions than Pd,[218] leading to the formation of Schottky barriers (Figure 22b,c). Therefore, the current of the Pd-contact SWCNTs was significantly decreased as increasing H_2 concentrations. Recently, Choi *et al.*[227] investigated the sensing properties of Pd-contact CNT-based FETs H_2 sensors depending on the width and length of SWCNT-channels (Figure 22d). They pre-separated semiconducting SWCNTs to increase Schottky contact between SWCNTs and Pd electrodes (Figure 22d), and the sensors showed high responses to low levels of H_2 (down to 0.02%) (Figure 22e). The thinner channel induced a higher H_2 response due to the increased portion of the contact resistance of the total channel resistance (Figure 22f), while the width of the channel did not.

Graphene-Based Materials. *Catalyst/Graphene Composites.* Most of the graphene-based H_2 sensors highly depend on the usage of catalytic metal NPs due to the insensitivity of graphene to H_2. Pd and Pt are well-known catalysts for graphene-based H_2 sensors. Johnson *et al.*[228] developed a Pd-loaded multilayer graphene nanoribbon network using an electron-beam evaporator. Due to the phase transition of Pd to

https://dx.doi.org/10.1021/acsnano.0c05307
ACS Nano 2020, 14, 14284−14322

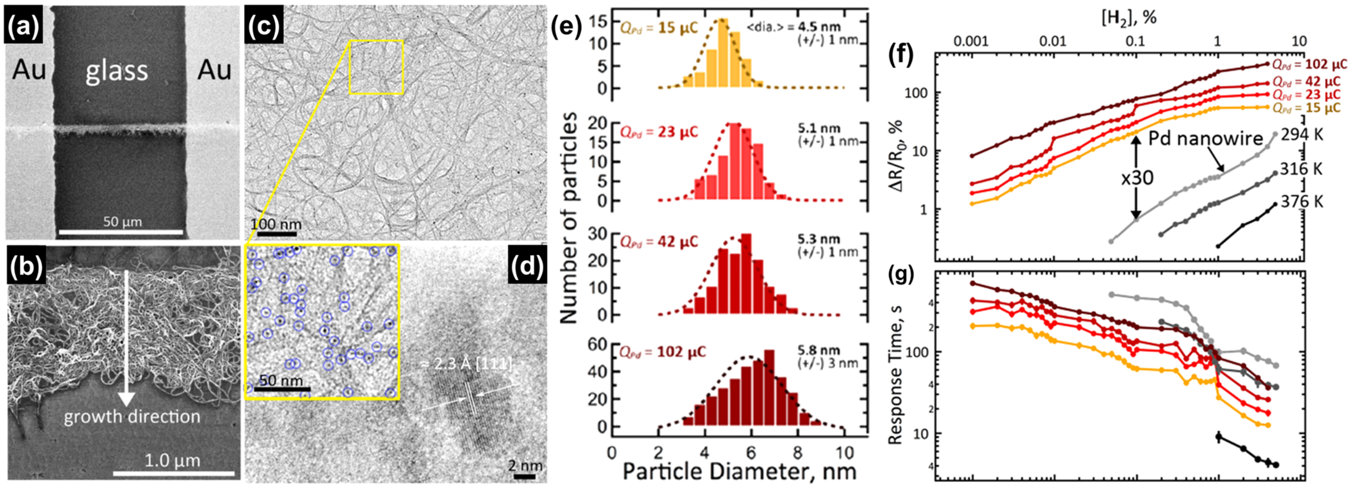

Figure 21. (a) SEM image of Pd/SWCNT composite-based H_2 sensors. (b) SEM image of SWCNT ropes. (c) TEM image and (d) high-resolution TEM image of Pd/SWCNT composites. (e) Particle size distribution of Pd NPs on SWCNTs in terms of the Coulombic loading (Q_{pd}). (f) Responses and (g) response times of the Pd/SWCNT composites and Pd nanowires from 10 ppm to 10% of H_2. Reprinted with permission from ref 223. Copyright 2017 American Chemical Society.

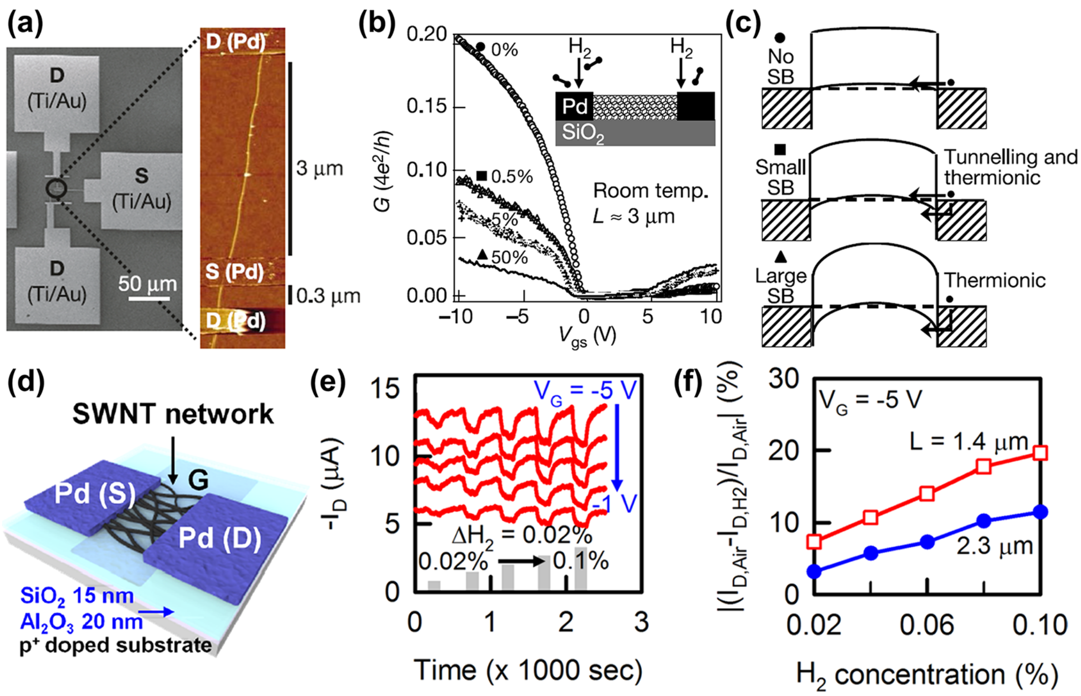

Figure 22. (a) SEM and AFM image of a Pd-contact SWCNT-based FETs. (b) Linear $G-V$ graphs for the Pd-contact SWCNT-based FET before and after the H_2 exposures. L is the channel length of the Pd-contact SWCNT-based FET. (c) Schematic illustration of the sensing mechanism of Schottky contact-based H_2 sensors (SB: Schottky barrier). Reprinted with permission from ref 213. Copyright 2003 Nature Publishing Group. (d) Schematic illustration of the Pd-contact SWCNT network for H_2 sensors. (e) Current (I_d) traces of the sensors in response to 0.02–0.1% of H_2. (f) Responses of the sensors *versus* H_2 concentration at different channel lengths (L). Reprinted with permission from ref 227. Copyright 2015 AIP Publishing.

PdH_x, the composites exhibited high H_2 response ($\Delta R_g/R_0$ = 55% to 40 ppm of H_2) at RT in N_2. Then, their resistances were recovered when exposed to air by the catalytic water formation reactions. In addition, Chung *et al.*[229] developed flexible H_2 sensors using Pd/graphene composites. The transfer of graphene layers to a PET substrate and the subsequent deposition of Pd using thermal evaporation produced Pd NPs on graphene layers on PET substrates. Due to the high mechanical strength of graphene layers and the catalytic effect of Pd NPs, the flexible sensors showed efficient H_2 sensing properties ($\Delta R_g/R_0$ = 22.5% to H_2 0.1%) at RT in N_2. More recently, Hong *et al.*[230] reported highly selective Pd/graphene composite-based H_2 sensors. They optimized the loading amounts of Pd NPs on graphene layers (Figure 23a,b), and the optimum conditions realized the detection of H_2 ranging from 0.025–2% (Figure 23c). Importantly, the use of a poly(methyl methacrylate) (PMMA) membrane improved the selectivity of Pd/graphene composites (Figure 23d). Without the use of the PMMA membrane, the Pd/graphene composites exhibited sensing responses to various analytes, including H_2

https://dx.doi.org/10.1021/acsnano.0c05307
ACS Nano 2020, 14, 14284–14322

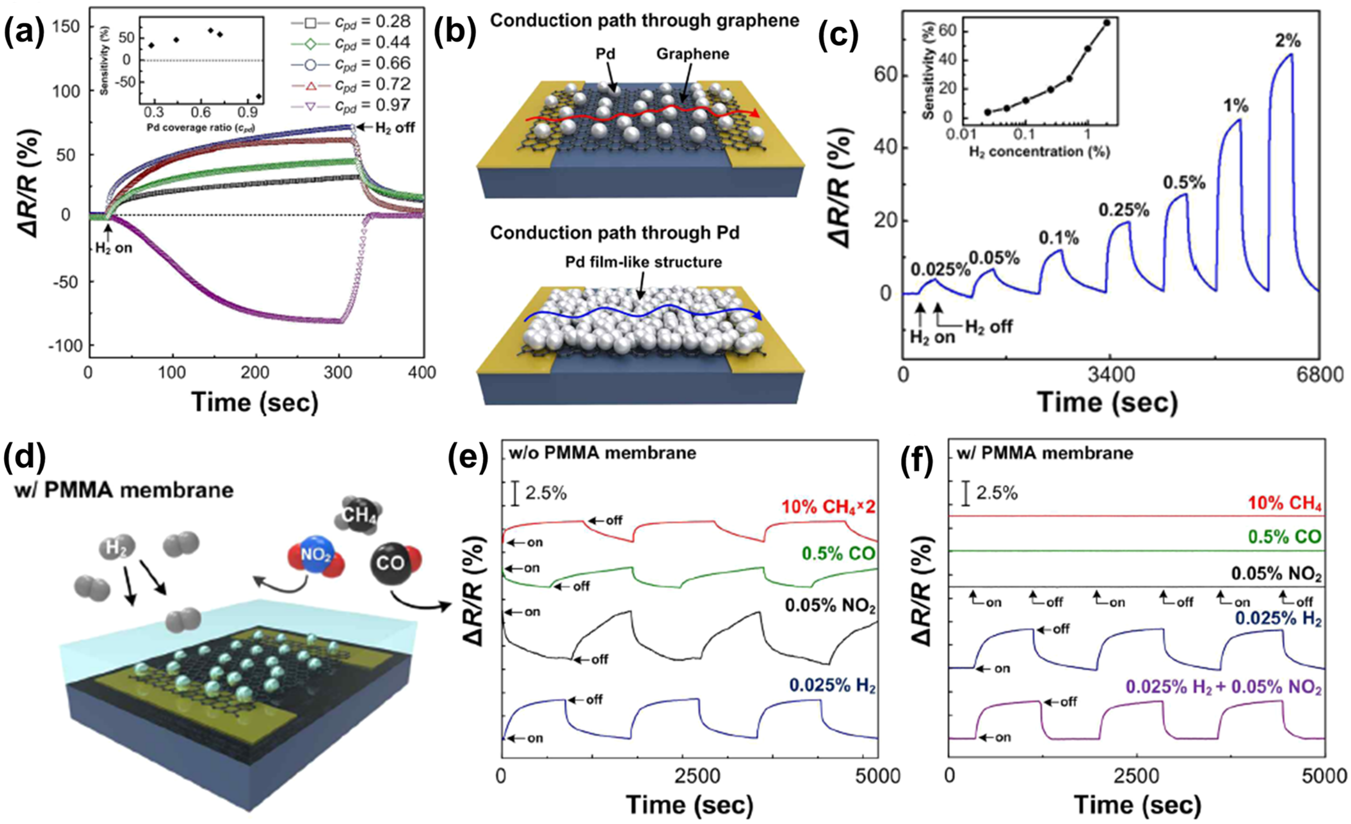

Figure 23. (a) Response traces of Pd/graphene composites when exposed to 2% H_2. (b) Schematic illustration of the conduction path in the Pd/graphene composites with the different coverage ratio of Pd to graphene. (c) Response traces of optimum Pd/graphene composites in response to 0.025−2% of H_2. (d) Schematic illustration of PMMA/Pd/graphene composites. (e) Responses of the Pd/graphene composites to various analytes (0.025% H_2, 0.05% NO_2, 0.5% CO, and 10% CH_4). (f) Responses of the PMMA/Pd/graphene composites to various analytes and mixtures (0.025% H_2 and 0.05% NO_2). Reproduced with permission from ref 230. Copyright 2015 American Chemical Society.

Table 3. Recent Studies on Carbon-Based H_2 Sensors Operated at RT in Air

material	measurement	reponse (H_2 1%)	response (t_{90}) and recovery time (t_{10}) (H_2 1%)	LOD[a] ([H_2])	ref[b]
Pd/SWCNT	conductance ($\Delta G_g/G_a$)	n.r.[c] (50% to H_2 400 ppm)	n.r.	40 ppm	212
Pd/SWCNT	resistance ($\Delta R/R_a$)	130%	1.5 and 60 s	30 ppm	219
Pd/SWCNT	resistance ($\Delta R/R_a$)	130%	3 s and n.r.	100 ppm	220
Pd/SWCNT	resistance ($\Delta R/R_a$)	600%	2 and 58 min	100 ppm	221
Pd/CNT	resistance ($\Delta R/R_a$)	65%	4 s and n.r.	500 ppm	222
Pd/SWCNT	resistance ($\Delta R/R_a$)	55%	3 and 3 s	10 ppm	223
Pd-contact SWCNT (FET)	conductance ($\Delta G_g/G_a$)	n.r. (50% to H_2 0.5%)	n.r.	n.r.	213
Pd-contact SWCNT (FET)	current ($\Delta I/I_a$)	n.r. (20% to H_2 0.1%)	n.r.	0.02%	227
Pd/graphene	resistance ($\Delta R/R_a$)	11%	n.r.	25 ppm	236
Pd/graphene	resistance ($\Delta R/R_a$)	50%	n.r.	n.r.	237
Pd/graphene	resistance ($\Delta R/R_a$)	n.r. (22.5% to H_2 0.1%)	1 min and n.r.	20 ppm	229
Pd/graphene	resistance ($\Delta R/R_a$)	48%	~108 s and ~331 s	250 ppm	230
Pt/graphene	resistance ($\Delta R/R_a$)	n.r. (17% to H_2 4%)	n.r.	n.r.	233
Pt/graphene	resistance ($\Delta R/R_a$)	18%	n.r.	n.r.	234
Au/graphene	resistance ($\Delta R/R_a$)	n.r. (6.9% to H_2 0.1%)	n.r.	1 ppm	235

[a]LOD is the limit of detection of the sensors demonstrated by experimental measurements. [b]Ref is the reference number. [c]n.r. indicates not reported.

0.025%, nitrogen dioxide (NO_2) 0.05%, carbon monoxide (CO) 0.5%, and methane (CH_4) 10% (Figure 23e). However, with the PMMA layer, the sensors exhibited ultrahigh H_2 selectivity (Figure 23f), because the permeability of H_2 in PPMA is much higher than other gas molecules due to the difference in the kinetic diameter (0.289 nm for H_2, 0.33 nm for CO, 0.38 nm for CH_4, and 0.4 nm for NO_2).[231,232]

On the other hand, there were few reports on other noble metal-functionalized graphene composites for H_2 sensors.[233−235] For example, Kaniyoor *et al.*[233] reported Pt-functionalized graphene oxides for H_2 sensors. Pt NPs were directly grown on the surface of graphene oxides using chemical reductions. Since Pt NPs can facilitate the catalytic oxidation of H_2, charge transfers occurred between Pt NPs and graphene oxides when exposed to H_2. Therefore, the

https://dx.doi.org/10.1021/acsnano.0c05307
ACS Nano 2020, 14, 14284−14322

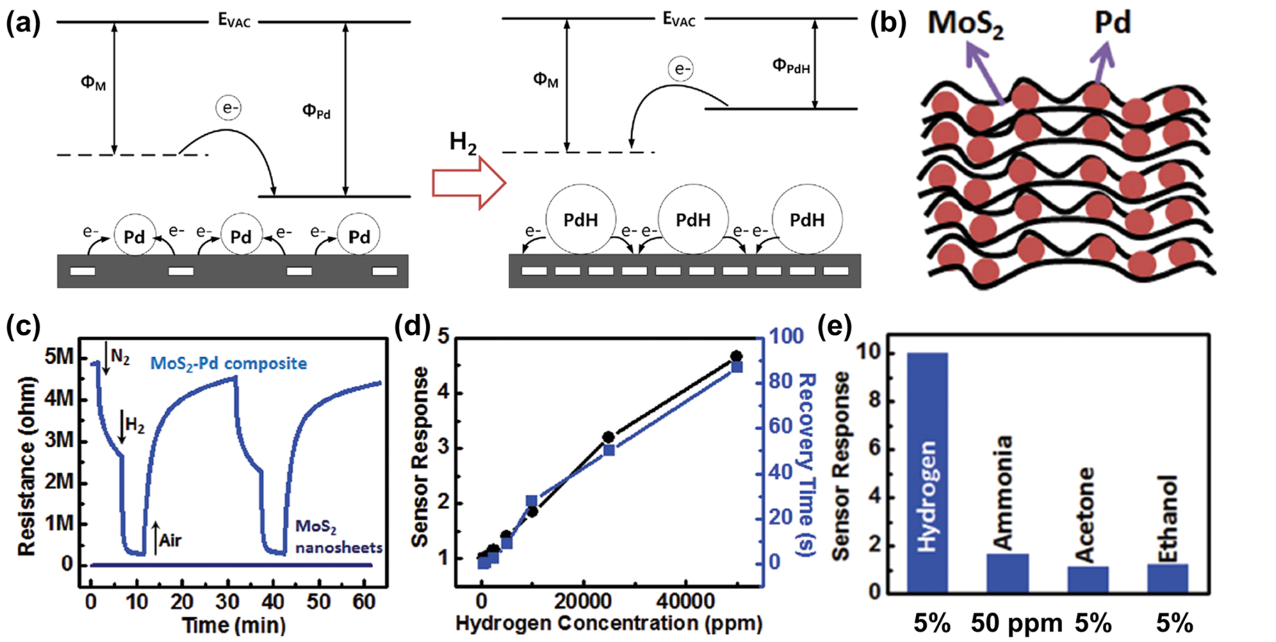

Figure 24. (a) Schematic illustrations for the sensing mechanisms of Pd/MoS_2 composites. Reprinted with permission from ref 249. Copyright 2017 Elsevier. (b) Schematic illustration of the structure of Pd NP/MoS_2 composites. (c) Response traces of Pd NP/MoS_2 composites and pristine MoS_2 nanosheets in response to H_2 5%. (d) Responses and recovery times of Pd NP/MoS_2 composites in the range of 500−50,000 ppm of H_2. (e) Selectivity of Pd NP/MoS_2 composite to various analytes. Sensor response was defined as R_0/R_g. Reprinted with permission from ref 254. Copyright 2015 Wiley-VCH.

composites exhibited H_2 sensing properties ($\Delta R_g/R_a$ = 16% to H_2 [4%]) at RT in air. However, since Pt NPs also promote the absorption of other analytes, the selectivity of Pt/graphene composite-based H_2 sensors should be further improved. In another case, Kim *et al.*[235] synthesized three layers of graphene functionalized with Au nanoclusters (NCs) for H_2 sensors. The Au NC/graphene composites showed 48.8-fold higher response (5.46% at a bias voltage of 60 V) toward H_2 gas (500 ppm) than that (0.09%) of pristine graphene. Through DFT calculations, it was revealed that the Au NCs in the Au NC/graphene composite structure accommodate good adsorption of H atoms, whereas pristine Au NCs or pristine graphene do not bind with H atoms. Hence, the heterostructures of metal nanocatalyst/graphene surely displayed interesting H_2 sensing properties.

Challenges of Carbon-Based Materials. Carbon-based nanomaterials, such as CNTs and graphene, have emerged as efficient sensing materials due to their operation at low temperatures. Even though they have no direct interaction with H_2, the decoration of catalysts enables the chemiresistive H_2 sensing behaviors of carbon-based materials. Table 3 presents the summary of the sensing properties of representative carbon-based H_2 sensors operated at RT in air.[212,213,219−223,227,229,230,233−237] In particular, their sensing properties highly depend on catalytic Pd NPs, and they exhibited efficient and fast H_2 sensing properties. The remaining challenges in carbon-based sensors are low selectivity, slow response speed to low [H_2], and poor reproducibility. First, carbon-based materials have a high reactivity to polar gas molecules, such as NO_2, NH_3, and H_2O, at low operating temperatures;[26] therefore, the sensors should have high H_2 selectivity against such polar gas molecules. Second, most of the carbon-based H_2 sensors exhibited a very slow sensing speed to low levels of H_2 because the phase transition of Pd to PdH_x is sluggish at low [H_2].[10] Last, carbon-based materials often exhibit poor reproducibility, however, for commercialization, the sensors should have high reliability and reproducibility with high yield.

OTHER MATERIALS

TMD-Based Materials. Recently, 2D TMDs have attracted much attention in various applications, due to their ultrahigh surface-to-volume ratio, 2D van der Waals structures, and tunable electrical properties.[27,238] In the field of chemical sensors, Li *et al.*[239] demonstrated MoS_2-based FET sensors for NO detection at RT, which is one of the early studies on TMD-based sensors. Since then, various TMD-based chemical sensors, including MoS_2,[240,241] $MoSe_2$,[242] WS_2,[243,244] and SnS_2,[245,246] have been developed for the detection of nitrogen oxide (NO_x), ammonia (NH_3), and humidity (H_2O). However, because TMDs have a high reactivity to such gases with high polarity,[28] it is difficult to develop highly sensitive and selective H_2 sensors using pure 2D TMDs. Although some pure TMD-based nanostructures were reported as efficient H_2 sensors,[247,248] the selectivity was not presented in the articles. Therefore, it is imperative to combine catalysts for H_2 sensing with TMDs, in order to develop TMD-based H_2 sensors with high H_2 selectivity against interfering gases.

Catalyst/TMD-Based Composites. One of the representative catalysts for TMD-based H_2 sensors is Pd NPs that have the phase transition from Pd to PdH_x.[15] This phase transition allows TMDs to have selective H_2 sensing properties. The basic sensing mechanisms for Pd/TMD composites are as follows (Figure 24a).[249] The deposition of Pd NPs on MoS_2 generates heterojunctions at the interfaces,[250] due to the difference in work functions (5.7 eV for Pd NPs[251] and 4.5 eV for MoS_2[252]). Upon H_2 exposure, the phase transition of Pd to PdH_x increases the Fermi levels of Pd NPs,[253] thereby changing the electronic band structure of Pd/MoS_2. Therefore, the reactions of Pd with H_2 are translated into chemiresistive

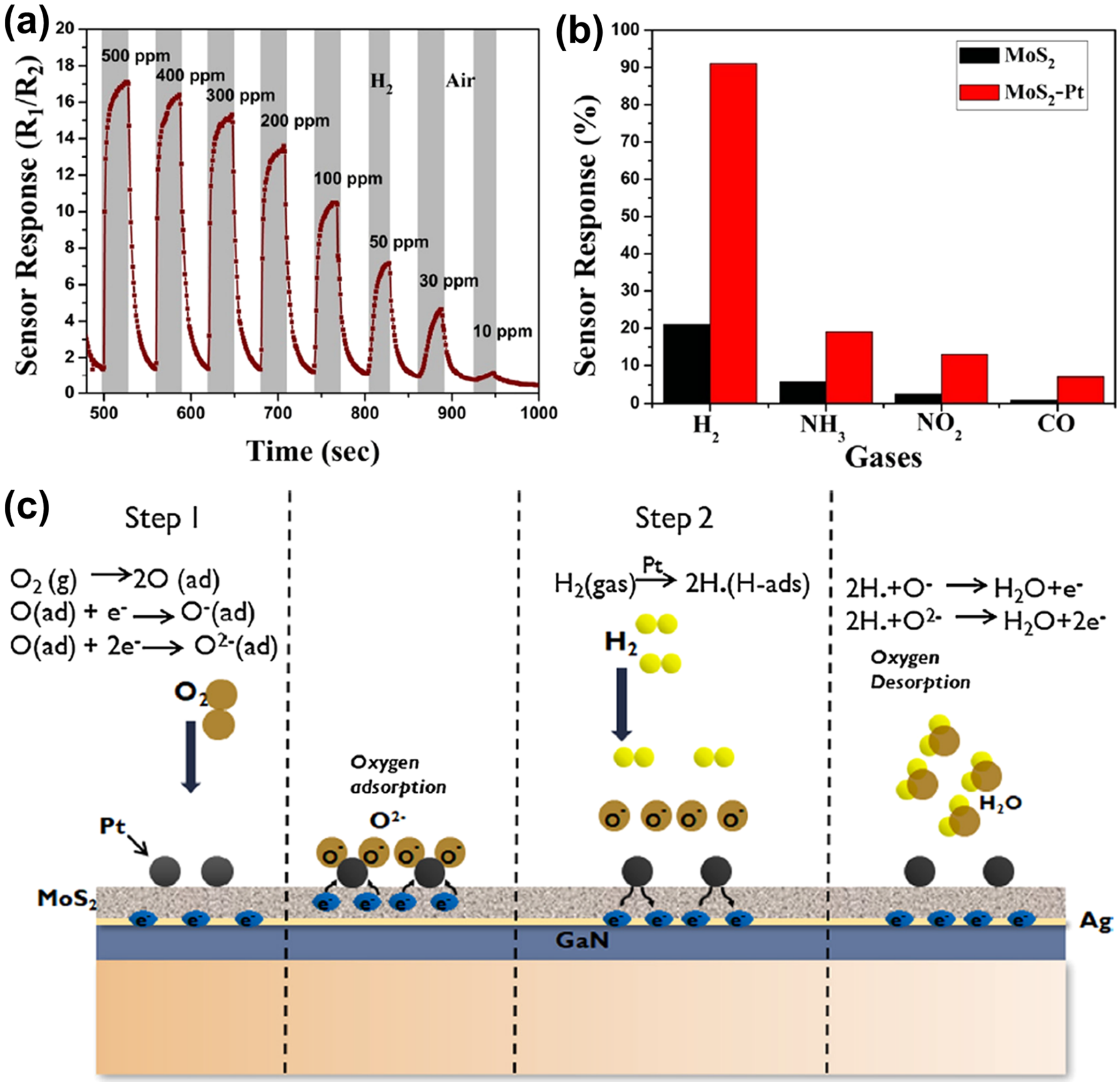

Figure 25. (a) Response (R_a/R_g) traces of Pt/MoS$_2$ composites in response to 10−500 ppm of H_2 at 150 °C. (b) Responses of the Pt/MoS$_2$ composites to 10 ppm of various analytes (H_2, NH_3, NO_2, and CO). (c) Schematic illustration of the sensing mechanisms of the Pt/MoS$_2$ composites. Reprinted with permission from ref 258. Copyright 2020 Elsevier.

sensing behaviors of MoS_2-based sensors. For instance, Kuru *et al.*[254] developed Pd/MoS$_2$ composites for H_2 sensors. They prepared Pd NP-loaded MoS_2 nanosheets (Pd NP/MoS$_2$) by the mixing of $PdCl_2$ and exfoliated MoS_2 and subsequent annealing at 400 °C in forming gas atmospheres (Figure 24b). The pristine MoS_2 nanosheets did not exhibit any response, however, Pd NP/MoS$_2$ composites showed huge resistance changes upon exposure to H_2 (R_0/R_g = 4.5 to H_2 5%) (Figure 24c). The Pd NP/MoS$_2$ composites were able to detect a wide range of H_2 from 500 ppm to 5% (Figure 24d). In addition, the Pd NP/MoS$_2$ composites showed a high H_2 selectivity against NH_3, acetone (CH_3COCH_3), and ethanol (C_2H_5OH) (Figure 24e), although the concentration of NH_3 (50 ppm) was different to other gas molecules (5%). This study demonstrated the feasibility of Pd/MoS$_2$ composites for H_2 sensors and stimulated the development of various Pd/TMD composites for H_2 sensors, such as Pd/MoS$_2$,[249,255] Pd/WS$_2$[256], and Pd/SnO$_2$/MoS$_2$[257]. These Pd/TMD composites showed interesting and efficient H_2 sensing properties.

In addition to Pd NPs, Pt NPs were incorporated in 2D TMDs for the development of H_2 sensors. Gottam *et al.*[258] reported Pt NP-deposited MoS_2 nanosheets using simple chemical reduction processes, as reported elsewhere.[259] The Pt NP/MoS$_2$ composites exhibited efficient H_2 sensing properties (R_a/R_g = 10 to H_2 100 ppm) at an elevated operating temperature (150 °C) (Figure 25a). The sensing range of the sensors was H_2 10−500 ppm with fast responses (t_{80} = 4 s to H_2 100 ppm) and recovery speed (t_{80} = 19 s), and the sensors displayed high H_2 selectivity against NH_3, NO_2, and CO (Figure 25b). They assumed that these sensing properties were attributed to the catalytic water formation reactions on Pt NPs. Because Pt NPs have the ability to dissociate oxygen molecules,[142] adsorbed oxygen species were generated on the surface Pt NPs (step 1 in Figure 25c). Then, when exposed to H_2, adsorbed oxygen species on Pt NPs were removed by catalytic water (H_2O) formation reactions (eq 8),[64,65] which can lead to the resistance changes in TMD-based sensors (step 2 in Figure 25c).

https://dx.doi.org/10.1021/acsnano.0c05307
ACS Nano 2020, 14, 14284−14322

Table 4. Recent Studies on 2D TMD-Based H_2 Sensors Operated at RT in Air

material	measurement	reponse (H_2 1%)	response (t_{90}) and recovery time (t_{10}) (H_2 1%)	LOD[a] ([H_2])	ref[b]
Pd/MoS_2	resistance ($\Delta R/R_a$)	35%	786 and 902 s	50 ppm	249
Pd/WS_2/Si	current (I_g/I_a)	9	170 and 34 s	0.1%	256
Pd/SnO_2/MoS_2	current ($\Delta I_g/I_a$)	n.r. (18% to H_2 0.5%)	n.r.	30 ppm	257
GaN/MoS_2	resistance ($\Delta R/R_a$)	16%	n.r.	0.1%	260
3D MoS_2	current ($\Delta R/R_a$)	1%	14 and 137 s	n.r.[c]	247
Pd/MoS_2/SiO_2	current ($I_a/\Delta I$)	1000%	30 and 29 s	0.5%	255
sericin/MoS_2	resistance ($\Delta R/R_a$)	n.r. (36.5% to H_2 0.01%)	n.r. (10 and 6 s to H_2 0.01%)	10 ppm	261
Pt/MoS_2	resistance ($\Delta R/R_a$)	8.7%	8.1 and 16 s	500 ppm	262

[a]LOD is the limit of detection of the sensors demonstrated by experimental measurements. [b]Ref is the reference number. [c]n.r. indicates not reported.

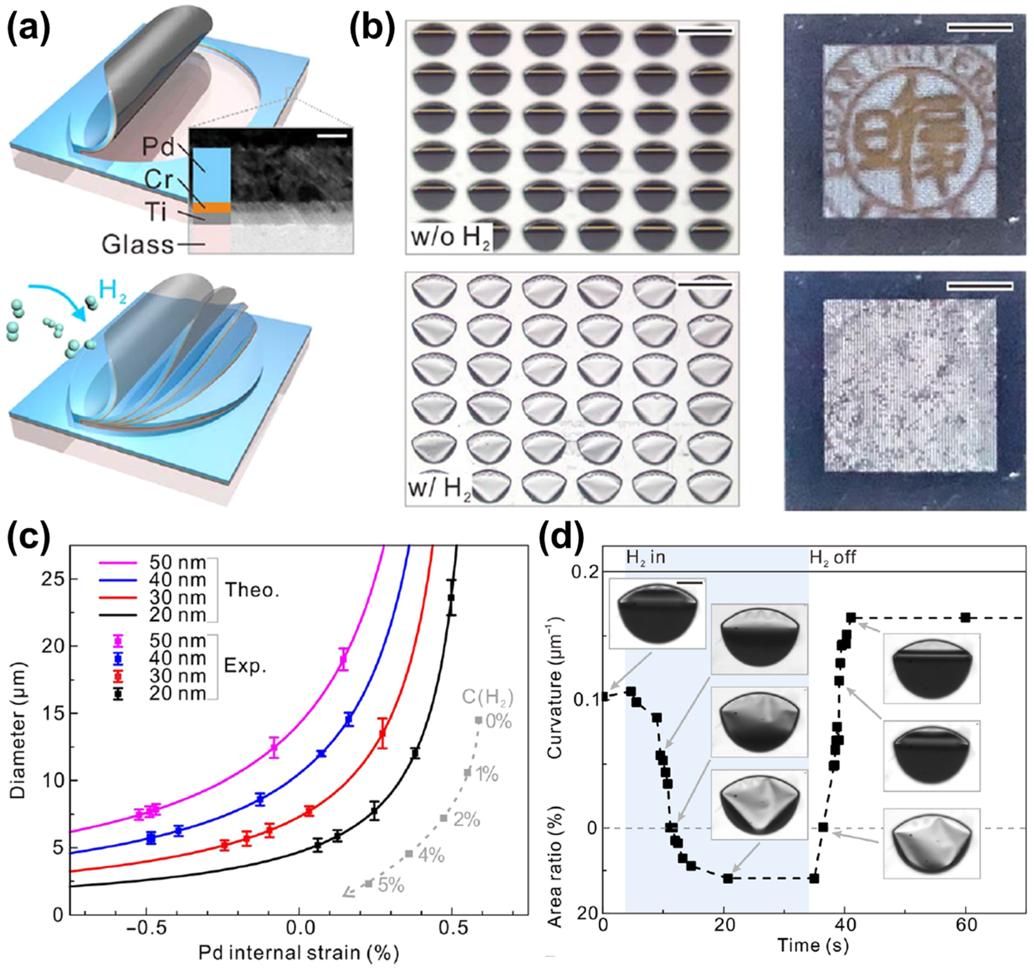

Figure 26. (a) Schematic illustration of stimuli-responsive nanomembrane microrolls that are responding to H_2. Scale bar, 25 nm. (b) Optical images of the nanomembrane microrolls without and with H_2. Scale bars, 100 mm for left images and 2 mm for right. (c) The calculated internal strain of Pd crystals upon H exposures. (d) The rolling of the nanomembrane microrolls in response to H_2 exposures. Insets are the optical images at the point. Scale bar, 25 mm. Reprinted with permission under a Creative Commons CC-BY license from ref 275. Copyright 2018 the American Association for the Advancement of Science.

Challenges of TMD-Based H_2 Sensors. Table 4 summarizes the sensing performances of TMD-based H_2 sensors operated at RT in air.[247,249,255−257,260−262] Their sensing properties are inferior to other sensing materials, such as Pd and metal oxides. However, since TMDs have various fascinating features as chemical sensors, such as high surface area, 2D structure, tunable electrical properties, and operation at RT,[27,238] we expect that the TMD-based H_2 sensors can grow rapidly in the future. The issues with TMD-based H_2 sensors are as follows. First, the sensing properties of TMD-based sensors should be further improved. In particular, excellent H_2 selectivity should be achieved because TMDs are known to have a high reactivity to NO_x, NH_3, and humidity at RT.[28] Second, TMD-based sensors are degraded during long-term operation in air, because the surface of TMDs can be severely affected by O_2 and humidity in air. For instance, TMDs can be partially oxidized in air,[263] degrading response and sensing speed. Third, 2D van der Waals structures of TMDs have large surface areas and high surface to volume ratios, but they can be easily agglomerated during device fabrication. To fully utilize the

https://dx.doi.org/10.1021/acsnano.0c05307
ACS Nano 2020, 14, 14284−14322

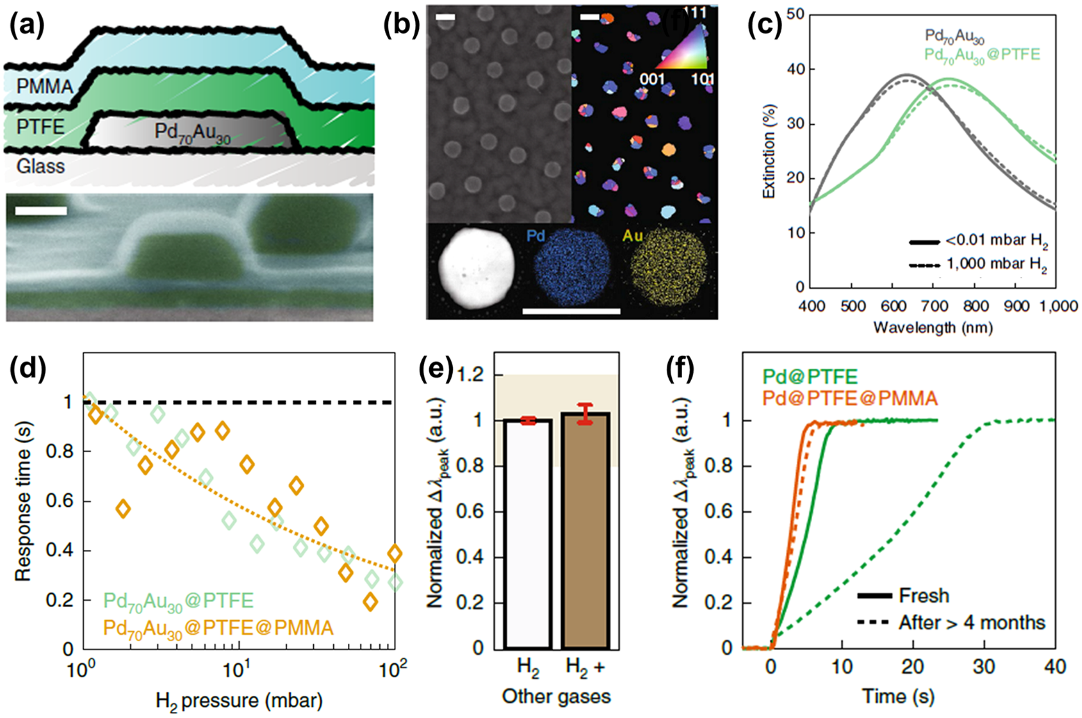

Figure 27. (a) Schematic illustration of $Pd_{70}Au_{30}$/PTFE/PMMA composites for plasmonic H_2 sensors. (b) SEM image (top left) and transmission Kikuchi diffraction micrograph (top right) of the $Pd_{70}Au_{30}$ NP array, and energy-dispersive X-ray elemental mapping images of a single $Pd_{70}Au_{30}$ NP (bottom). Scale bars, 200 nm. (c) Optical transmittance spectra of $Pd_{70}Au_{30}$ alloy NP array in vacuum (the straight line) and at 1000 mbar H_2 (the dashed line). (d) Response times of the composites *versus* H_2 pressures. (e) Normalized shifts in plasmonic peaks of the $Pd_{70}Au_{30}$/PTFE/PMMA composites when exposed to H_2 4% in air with and without other gases (CO_2 3%, CO 0.1%, and NO_2 0.01%). (f) Absorption kinetics of Pd/PTFE composites and Pd/PTFE/PMMA composites to 40 mbar H_2 at different aging states. Reprinted with permission from ref 279. Copyright 2019 Springer Nature Group.

advantages of TMDs, it is necessary to develop rational structures for TMD-based H_2 sensors.

MXenes. MXenes, which are a family of 2D transition-metal carbides and nitrides, gain enormous attention owing to their fascinating potentials in vaious applications.[264−266] MXenes as gas sensors offer an ultrahigh signal-to-noise ratio, which can lead to low detection limits.[267] Due to these intriguing propreties, MXenes were demonstrated as promising gas sensing materials for NH_3[268−271] and toluene.[272] However, there are only a few studies on MXene-based H_2 sensors. Recently, as one of the early studies, Lee *et al.*[273] have employed 2D vanadium carbide MXene (V_2CT_x) as a H_2 sensing layer. Single- or few-layer of V_2CT_x on a polyimide film exhibited ultralow detection limits (2 ppm) of H_2 at RT in air. In addition, Zhu *et al.*[274] synthesized a paper film based on 2D titanium carbide MXene ($Ti_3C_2T_x$) functionalized with Pd colloidal nanoclusters. The paper film exhibited a high response (23.0 ± 4.0%) to 4% [H_2] with a response time of 32 ± 7 s. These results demonstrated that MXenes can be considered as chemiresistors for H_2 sensing, and further optimization of MXenes can improve H_2 sensing abilities in the future.

Recent Key Advances in Other Types of H_2 Sensors. As mentioned in the Introduction, there are various types of H_2 sensors, such as chemiresistive, plasmonic, colorimetric, electrochemical, and mechanical sensors.[8] This review focuses on recent advances in chemiresistive H_2 sensors, but also there were significant advances in other types of H_2 sensors. In this section, we briefly introduce recent representative studies on other types of H_2 sensors.

Recently, Xu *et al.*[275] developed macroscopic visual H_2 sensors by using stimuli-responsive microrolls. Inspired by the fact that the phase transition of Pd from α-PdH_x to β-PdH_x induces volume expansion as well as internal lattice stress,[15] they hypothesized that this lattice stress leads to the structural changes in Pd-based composites. In brief, the bilayer structures of Pd (from 20 to 50 nm) and Cr (5 nm)/Ti (5 nm) were prepared by UV lithography and electron-beam evaporator, and the subsequent rolling of the bilayers generated by nanomembrane microrolls (Figure 26a). Interestingly, micro-roll arrays were unrolled when exposed to H_2 and were rolled up in the absence of H_2 (Figure 26b), thereby enabling the visual detection of H_2 using the naked eye. To elucidate the physical phenomena in this system, they calculated the internal strain in the Pd lattice by using elastic models.[276−278] The calculations revealed that there was a critical point to convert the compressive stress to tensile stress in the Pd crystals upon H_2 exposures (Figure 26c). In particular, the phase transition of Pd to β-PdH_x induces the tensile stress in Pd crystals, while the phase transition of β-PdH_x to Pd induces the compressive stress. Therefore, the microroll arrays were physically responsive to H_2 (Figure 26d). Although the sensing range of microroll arrays was limited to over H_2 1% due to their mechanisms relying on the formation of β-PdH_x, this system provided a simple method to detect H_2 using the naked eye.

In addition, there have been significant advances in plasmonic H_2 sensors. Nugroho *et al.*[279] demonstrated ultrafast plasmonic H_2 sensing by using PdAu/polymer composites. In particular, they achieved the response times of <1 s to the wide range of H_2 pressures. In detail, they fabricated the patterns of

Table 5. Representative Materials for Chemiresistive H_2 Sensors and the Comparison of Their Characteristics

material	typical example	sensing mechanisms	advantages	disadvantages
metal-based materials	Pd	•phase transition of Pd to PdH_x($Pd + 1/2H_2 \rightarrow PdH_x$)	•operation at RT	•poor sensing properties to low $[H_2]$
			•high selectivity	•poor stability during long-term operation for high $[H_2]$
		•decreased resistances by the volume expansion of β-PdH_x	•fast sensing speed to high $[H_2]$	•relatively high cost than other materials
			•high thermal/chemical stability	
SMO-based materials	SnO_2 and ZnO	•reaction of H_2 with chemisorbed oxygen species ($H_2 + O^- \rightarrow H_2O + e^-$)	•meso- or macroporous structure	•operation at high temperature
			•high response	•high-power consumption
		•metallization of metal oxides ($ZnO + H_2 \rightarrow Zn + H_2O$)	•low detection limit	•poor selectivity
			•high thermal/chemical stability	•vulnerability to humidity
carbon-based materials	Pd/CNTs	•charge transfers from Pd to CNT by the phase transition of Pd to PdH_x	•operation at RT	•limited strategies for the fabricaiton of H_2 sensors
			•high surface area	•slow sensing speed to low $[H_2]$
		•modulation of Schottky barriers between CNT and Pd electrode by the phase transition of Pd to PdH_x	•relatively low cost for the sensor fabrication	•poor selectivity
				•low reproducibility
				•vulnerability to humidity
TMD-based materials	Pd/MoS_2	•charge transfers from Pd to MoS_2 by the phase transition of Pd to PdH_x	•operation at RT	•limited strategies for the fabricaiton of H_2 sensors
			•high surface area	•poor response
			•relatively low cost for the sensor fabrication	•slow sensing speed
				•poor selectivity
				•low reproducibility
				•vulnerability to humidity and oxygen

PdAu alloy NPs with a size of 150 nm and then deposited a polytetrafluoroethylene (PTFE) and PMMA membrane on the PdAu NP patterns (Figure 27a,b). The pristine Pd NPs can change the height and position of plasmonic peaks in optical transmittance spectra in response to H_2, due to their phase transition from Pd to PdH_x upon H_2 exposures. However, they exhibited a large hysteresis in the optical signals, which hinders the reliable detection of H_2. On the other hand, alloying Pd with Au ($Pd_{70}Au_{30}$) reduced the hysteresis in optical transmittance spectra upon H_2 exposures (Figure 27c),[280,281] enabling plasmonic H_2 sensing by calculating plasmonic peak shifts. In addition, the PTFE membrane can accelerate the adsorption kinetics of H_2 on Pd,[282] and the PMMA membrane can improve high H_2 selectivity against other gas molecules by the molecular sieving effect.[230,232] Therefore, the deposition of PTFE and PMMA on $Pd_{70}Au_{30}$ NPs improved not only the kinetics of H_2 reactions but also the stability of the sensing systems. For these reasons, the $Pd_{70}Au_{30}$/PTFE/PMMA composites exhibited an ultrafast sensing speed (<1 s) in the range of 1−100 mbar H_2 (Figure 27d). In addition, the H_2 sensing properties to H_2 4% were not degraded even in the presence of interfering gas molecules (CO_2 3%, CO 0.1%, and NO_2 0.01% in air) (Figure 27e). They also revealed that the deposition of the PMMA layer effectively improved the long-term stability of the sensors over 4 months (Figure 27f). Although the response speed of the plasmonic sensors in ambient air was longer than 1 s, this study achieved ultrafast sensing speed (<1 s in H_2 pressures) that meets the criteria for H_2 sensing speed.

CONCLUSIONS AND OUTLOOK

Since the first H_2 sensing experiments involving Pd nanowires were conducted in 2000, nanoscaled materials, including nanowires, nanotubes, nanoparticles, and 2D nanomaterials, have played a prominent roll in the development of state-of-the-art H_2 sensors. In this review, we presented recent advances in chemiresistive H_2 sensors. Coupled with the huge growth of the H_2 economy, the field of chemiresistive H_2 sensors—that translate H_2 reactions on sensing materials into electrical signals—has rapidly grown. The H_2 chemiresistors can be classified into several materials: metal (Pd and Pt), metal oxides (pure metal oxides, catalyst/metal oxides, and metal-oxide-based composites), carbons (CNTs and graphenes), and 2D TMDs (MoS_2). In each material, various interesting synthetic methods have been developed to improve H_2 sensing properties. They include the design of nanostructures, the fusion with other elements or materials, the addition of active materials, and the use of catalysts. We did our best to highlight some of the recent representative studies in chemiresistive H_2 sensors and to discuss their underlying mechanisms and the correlation of structure, composition, and key parameters.

Table 5 summarizes the typical examples, sensing mechanisms, advantages, and disadvantages of each material. In brief, (1) Pd is a typical metallic chemiresistor for H_2 detection and is operated by the phase transition of Pd to PdH_x. Because Pd-based sensors are able to detect H_2 at RT with high selectivity, they are considered as the current state-of-the-art H_2 sensors. However, they displayed poor sensing properties, such as

https://dx.doi.org/10.1021/acsnano.0c05307
ACS Nano 2020, 14, 14284−14322

responses and response/recovery times, to low levels of H_2 (below H_2 0.1%). In addition, the cost of noble-metal-based sensors is more expensive than other materials, which can be a drawback for commercialization. (2) In the case of metal-oxide-based H_2 sensors, they do not only have ultrahigh H_2 response with good detection limits but also have high thermal and chemical stability. However, most metal oxide-based sensors are operated at high temperatures (over 200 °C) to induce H_2 reactions with chemisorbed oxygen species or metal oxides. Therefore, they inherently have some disadvantages, including high power consumption, low selectivity, and vulnerability to humidity. (3) The carbon-based materials, such as CNTs and graphenes, are one of the ideal materials for chemiresistors due to their high surface areas, low-temperature operation, low-cost, and high-efficiency, but pure carbon-based materials have no appreciable reactivity to H_2. Therefore, they highly depend on the use of catalysts (*i.e.*, Pd) in order to translate the phase transition of Pd to PdH_x into chemiresistive H_2 sensing behaviors of carbon-based materials. These Pd/carbon composites have efficient sensing properties at RT, but there remain some issues, such as poor sensing properties to low $[H_2]$ concentration, low selectivity against polar gas molecules (*e.g.*, NO_2, NH_3, and H_2O), and poor reproducibility. (4) The 2D TMD-based materials are one of the emerging materials in the field of chemical sensors due to their high surface to volume ratio and 2D van der Waals structures. However, for H_2 sensing, they also rely on the decoration of catalysts, and their sensing properties are inferior to other H_2 sensing materials. In addition, they are vulnerable to oxygen in air and have a high reactivity to polar gases, which are critical issues in TMD-based H_2 sensors.

Despite these successful innovations, there are unmet challenges in all materials for chemiresistive H_2 sensors. First, response and recovery speed should be further accelerated to below 1 s, particularly for $[H_2] \geq 1\%$, which is the criteria for H_2 sensors for safety. To the best of our knowledge, such ultrafast sensing speed has not yet achieved in the field of chemiresistive H_2 sensors. Second, sensing properties to low levels of H_2 should be further improved to detect H_2 leakages in the early stages. However, while many H_2 sensors are able to detect H_2 at ppm levels, sensing speed and selectivity are degraded for $[H_2] < 0.1\%$ in most cases. Third, the H_2 selectivity of sensors in various gas mixtures should be demonstrated because there are many interfering gas species in air, and these gas molecules can disturb the surface reaction of H_2 and sensing materials. Fourth, to realize the operation of H_2 sensors in ambient conditions, the reliability of H_2 sensors should be proven in various humidity levels (5−98%) and temperatures (−30 to 80 °C). Finally, H_2 sensors should stably operate with high reliability and without significant signal drift over 6 months because the long-term stability is one of the important parameters for commercialization. Since chemiresistive H_2 sensors have various fascinating features and there remain undeveloped or unexplored areas, we strongly believe that the field of chemiresistive H_2 sensors will further grow in the future and overcome the critical challenges of current H_2 sensors. We hope that this review inspires various scientific communities and industrial fields, and guides the way for the practical applications of chemiresistive H_2 sensors.

AUTHOR INFORMATION

Corresponding Authors

Reginald M. Penner − *Department of Chemistry, University of California, Irvine, California 92697-2025, United States;* orcid.org/0000-0003-2831-3028; Email: rmpenner@uci.edu

Il-Doo Kim − *Department of Materials Science and Engineering, Korea Advanced Institute of Science and Technology (KAIST), Daejeon 34141, Republic of Korea;* orcid.org/0000-0002-9970-2218; Email: idkim@kaist.ac.kr

Authors

Won-Tae Koo − *Department of Materials Science and Engineering, Korea Advanced Institute of Science and Technology (KAIST), Daejeon 34141, Republic of Korea*

Hee-Jin Cho − *Department of Materials Science and Engineering, Korea Advanced Institute of Science and Technology (KAIST), Daejeon 34141, Republic of Korea*

Dong-Ha Kim − *Department of Materials Science and Engineering, Korea Advanced Institute of Science and Technology (KAIST), Daejeon 34141, Republic of Korea*

Yoon Hwa Kim − *Department of Materials Science and Engineering, Korea Advanced Institute of Science and Technology (KAIST), Daejeon 34141, Republic of Korea*

Hamin Shin − *Department of Materials Science and Engineering, Korea Advanced Institute of Science and Technology (KAIST), Daejeon 34141, Republic of Korea*

Complete contact information is available at: https://pubs.acs.org/10.1021/acsnano.0c05307

Notes

The authors declare no competing financial interest.

ACKNOWLEDGMENTS

This work was supported by Korea Electric Power Corporation (KEPCO) Research Institute. This work was supported by Nano Convergence Foundation funded by the Ministry of Science and ICT (MSIT, Korea) and the Ministry of Trade, Industry, and Energy (MOTIE, Korea) (project no.: 20000230). This work was also supported by National Research Foundation (NRF) of the Korean Government (MSIT) (2020R1A2C301312711). R.M.P. gratefully acknowledges the financial support of this work by the U.S. National Science Foundation, through contract CBET-1803314.

VOCABULARY

Chemiresistors, sensors are able to detect chemicals by the transduction of chemical reactions into electrical signals; **responses**, sensor signals in response to analytes, which is usually defined as a relative ratio of resistance (or conductance) changes to baseline resistances (or conductance); **response and recovery times**, parameters for speed of sensors, which are generally defined as the time taken for from baseline to 90% of the maximum responses (t_{90}) and from maximum responses to 10% of maximum responses (t_{10}), respectively; **selectivity**, ability to screen target analytes against other interfering molecules; **limit of detection**, the lowest concentrations at which sensors are able to detect

REFERENCES

(1) Turner, J. A. Sustainable Hydrogen Production. *Science* **2004**, *305*, 972−974.

(2) Momirlan, M.; Veziroglu, T. Current Status of Hydrogen Energy. *Renewable Sustainable Energy Rev.* **2002**, *6*, 141−179.

(3) Winsche, W.; Hoffman, K. C.; Salzano, F. Hydrogen: Its Future Role in the Nation's Energy Economy. *Science* **1973**, *180*, 1325−1332.

(4) Trimm, D. L.; Önsan, Z. I. Onboard Fuel Conversion for Hydrogen-Fuel-Cell-Driven Vehicles. *Catal. Rev.: Sci. Eng.* **2001**, *43*, 31−84.

(5) Jacobson, M. Z.; Colella, W.; Golden, D. Cleaning the Air and Improving Health with Hydrogen Fuel-Cell Vehicles. *Science* **2005**, *308*, 1901−1905.

(6) Najjar, Y. S.; Mashareh, S. Hydrogen Leakage Sensing and Control. *Biomed. J. Sci. & Technol. Res.* **2019**, *21*, 16228−16240.

(7) *Multi-Year Research, Development, and Demonstration Plan, 576 2011−2020. Section 3.7 Hydrogen Safety, Codes and Standards*; Energy Efficiency and Renewable Energy (EERE), Department of Energy: Washington, DC, 2015.

(8) Hübert, T.; Boon-Brett, L.; Black, G.; Banach, U. Hydrogen Sensors−A Review. *Sens. Actuators, B* **2011**, *157*, 329−352.

(9) Korotcenkov, G.; Han, S. D.; Stetter, J. R. Review of Electrochemical Hydrogen Sensors. *Chem. Rev.* **2009**, *109*, 1402−1433.

(10) Penner, R. M. A Nose for Hydrogen Gas: Fast, Sensitive H_2 Sensors Using Electrodeposited Nanomaterials. *Acc. Chem. Res.* **2017**, *50*, 1902−1910.

(11) Nasir, M. E.; Dickson, W.; Wurtz, G. A.; Wardley, W. P.; Zayats, A. V. Hydrogen Detected by the Naked Eye: Optical Hydrogen Gas Sensors Based on Core/Shell Plasmonic Nanorod Metamaterials. *Adv. Mater.* **2014**, *26*, 3532−3537.

(12) Boon-Brett, L.; Bousek, J.; Black, G.; Moretto, P.; Castello, P.; Hübert, T.; Banach, U. Identifying Performance Gaps in Hydrogen Safety Sensor Technology for Automotive and Stationary Applications. *Int. J. Hydrogen Energy* **2010**, *35*, 373−384.

(13) Chiu, S.-W.; Tang, K.-T. Towards a Chemiresistive Sensor-Integrated Electronic Nose: A Review. *Sensors* **2013**, *13*, 14214−14247.

(14) Koo, W.-T.; Jang, J.-S.; Kim, I.-D. Metal-Organic Frameworks for Chemiresistive Sensors. *Chem.* **2019**, *5*, 1938−1963.

(15) Favier, F.; Walter, E. C.; Zach, M. P.; Benter, T.; Penner, R. M. Hydrogen Sensors and Switches from Electrodeposited Palladium Mesowire Arrays. *Science* **2001**, *293*, 2227−2231.

(16) Yang, F.; Kung, S.-C.; Cheng, M.; Hemminger, J. C.; Penner, R. M. Smaller Is Faster and More Sensitive: The Effect of Wire Size on the Detection of Hydrogen by Single Palladium Nanowires. *ACS Nano* **2010**, *4*, 5233−5244.

(17) Barsan, N.; Koziej, D.; Weimar, U. Metal Oxide-Based Gas Sensor Research: How To? *Sens. Actuators, B* **2007**, *121*, 18−35.

(18) Dey, A. Semiconductor Metal Oxide Gas Sensors: A Review. *Mater. Sci. Eng., B* **2018**, *229*, 206−217.

(19) Lee, J.-H. Gas Sensors Using Hierarchical and Hollow Oxide Nanostructures: Overview. *Sens. Actuators, B* **2009**, *140*, 319−336.

(20) Kim, H.-J.; Lee, J.-H. Highly Sensitive and Selective Gas Sensors Using p-Type Oxide Semiconductors: Overview. *Sens. Actuators, B* **2014**, *192*, 607−627.

(21) Kim, I.-D.; Rothschild, A.; Tuller, H. L. Advances and New Directions in Gas-Sensing Devices. *Acta Mater.* **2013**, *61*, 974−1000.

(22) Wang, C.; Yin, L.; Zhang, L.; Xiang, D.; Gao, R. Metal Oxide Gas Sensors: Sensitivity and Influencing Factors. *Sensors* **2010**, *10*, 2088−2106.

(23) Miller, D. R.; Akbar, S. A.; Morris, P. A. Nanoscale Metal Oxide-Based Heterojunctions for Gas Sensing: A Review. *Sens. Actuators, B* **2014**, *204*, 250−272.

(24) Ndaya, C. C.; Javahiraly, N.; Brioude, A. Recent Advances in Palladium Nanoparticles-Based Hydrogen Sensors for Leak Detection. *Sensors* **2019**, *19*, 4478.

(25) Sharma, B.; Sharma, A.; Kim, J.-S. Recent Advances on H_2 Sensor Technologies Based on Mox and Fet Devices: A Review. *Sens. Actuators, B* **2018**, *262*, 758−770.

(26) Schroeder, V.; Savagatrup, S.; He, M.; Lin, S.; Swager, T. M. Carbon Nanotube Chemical Sensors. *Chem. Rev.* **2019**, *119*, 599−663.

(27) Anichini, C.; Czepa, W.; Pakulski, D.; Aliprandi, A.; Ciesielski, A.; Samorì, P. Chemical Sensing with 2D Materials. *Chem. Soc. Rev.* **2018**, *47*, 4860−4908.

(28) Meng, Z.; Stolz, R. M.; Mendecki, L.; Mirica, K. A. Electrically-Transduced Chemical Sensors Based on Two-Dimensional Nanomaterials. *Chem. Rev.* **2019**, *119*, 478−598.

(29) Li, X.; Liu, Y.; Hemminger, J. C.; Penner, R. M. Catalytically Activated Palladium@Platinum Nanowires for Accelerated Hydrogen Gas Detection. *ACS Nano* **2015**, *9*, 3215−3225.

(30) Jung, W. B.; Cho, S. Y.; Suh, B. L.; Yoo, H. W.; Jeon, H. J.; Kim, J.; Jung, H. T. Polyelemental Nanolithography *via* Plasma Ion Bombardment: From Fabrication to Superior H_2 Sensing Application. *Adv. Mater.* **2018**, *31*, 1805343.

(31) Koo, W.-T.; Qiao, S.; Ogata, A. F.; Jha, G.; Jang, J.-S.; Chen, V. T.; Kim, I.-D.; Penner, R. M. Accelerating Palladium Nanowire H_2 Sensors Using Engineered Nanofiltration. *ACS Nano* **2017**, *11*, 9276−9285.

(32) Fahad, H. M.; Gupta, N.; Han, R.; Desai, S. B.; Javey, A. Highly Sensitive Bulk Silicon Chemical Sensors with Sub-5 Nm Thin Charge Inversion Layers. *ACS Nano* **2018**, *12*, 2948−2954.

(33) Fahad, H. M.; Shiraki, H.; Amani, M.; Zhang, C.; Hebbar, V. S.; Gao, W.; Ota, H.; Hettick, M.; Kiriya, D.; Chen, Y.-Z. Room Temperature Multiplexed Gas Sensing Using Chemical-Sensitive 3.5 nm-Thin Silicon Transistors. *Sci. Adv.* **2017**, *3*, e1602557.

(34) Yang, F.; Donavan, K. C.; Kung, S.-C.; Penner, R. M. The Surface Scattering-Based Detection of Hydrogen in Air Using a Platinum Nanowire. *Nano Lett.* **2012**, *12*, 2924−2930.

(35) Yoo, H.-W.; Cho, S.-Y.; Jeon, H.-J.; Jung, H.-T. Well-Defined and High Resolution Pt Nanowire Arrays for a High Performance Hydrogen Sensor by a Surface Scattering Phenomenon. *Anal. Chem.* **2015**, *87*, 1480−1484.

(36) Adams, B. D.; Chen, A. The Role of Palladium in a Hydrogen Economy. *Mater. Today* **2011**, *14*, 282−289.

(37) Li, G.; Kobayashi, H.; Dekura, S.; Ikeda, R.; Kubota, Y.; Kato, K.; Takata, M.; Yamamoto, T.; Matsumura, S.; Kitagawa, H. Shape-Dependent Hydrogen-Storage Properties in Pd Nanocrystals: Which Does Hydrogen Prefer, Octahedron (111) or Cube (100)? *J. Am. Chem. Soc.* **2014**, *136*, 10222−10225.

(38) Konda, S. K.; Chen, A. Palladium Based Nanomaterials for Enhanced Hydrogen Spillover and Storage. *Mater. Today* **2016**, *19*, 100−108.

(39) Bardhan, R.; Ruminski, A. M.; Brand, A.; Urban, J. J. Magnesium Nanocrystal-Polymer Composites: A New Platform for Designer Hydrogen Storage Materials. *Energy Environ. Sci.* **2011**, *4*, 4882−4895.

(40) Flanagan, T. B.; Oates, W. The Palladium-Hydrogen System. *Annu. Rev. Mater. Sci.* **1991**, *21*, 269−304.

(41) Yang, F.; Taggart, D. K.; Penner, R. M. Fast, Sensitive Hydrogen Gas Detection Using Single Palladium Nanowires That Resist Fracture. *Nano Lett.* **2009**, *9*, 2177−2182.

(42) Wagner, S.; Uchida, H.; Burlaka, V.; Vlach, M.; Vlcek, M.; Lukac, F.; Cizek, J.; Baehtz, C.; Bell, A.; Pundt, A. Achieving Coherent Phase Transition in Palladium−Hydrogen Thin Films. *Scr. Mater.* **2011**, *64*, 978−981.

(43) Pak, Y.; Lim, N.; Kumaresan, Y.; Lee, R.; Kim, K.; Kim, T. H.; Kim, S. M.; Kim, J. T.; Lee, H.; Ham, M. H.; et al. Palladium Nanoribbon Array for Fast Hydrogen Gas Sensing with Ultrahigh Sensitivity. *Adv. Mater.* **2015**, *27*, 6945−6952.

(44) Pak, Y.; Jeong, Y.; Alaal, N.; Kim, H.; Chae, J.; Min, J. W.; Devi, A. A. S.; Mitra, S.; Lee, D. H.; Kumaresan, Y.; et al. Highly Stable and Ultrafast Hydrogen Gas Sensor Based on 15 nm Nanogaps Switching in a Palladium−Gold Nanoribbons Array. *Adv. Mater. Interfaces* **2019**, *6*, 1801442.

(45) Lee, J.; Shim, W.; Lee, E.; Noh, J. S.; Lee, W. Highly Mobile Palladium Thin Films on an Elastomeric Substrate: Nanogap-Based Hydrogen Gas Sensors. *Angew. Chem., Int. Ed.* **2011**, *50*, 5301−5305.

(46) Shim, Y.-S.; Jang, B.; Suh, J. M.; Noh, M. S.; Kim, S.; Han, S. D.; Song, Y. G.; Kang, C.-Y.; Jang, H. W.; Lee, W. Nanogap-Controlled Pd Coating for Hydrogen Sensitive Switches and Hydrogen Sensors. *Sens. Actuators, B* **2018**, *255*, 1841−1848.
(47) Xu, T.; Zach, M.; Xiao, Z.; Rosenmann, D.; Welp, U.; Kwok, W.; Crabtree, G. Self-Assembled Monolayer-Enhanced Hydrogen Sensing with Ultrathin Palladium Films. *Appl. Phys. Lett.* **2005**, *86*, 203104.
(48) Hughes, R.; Schubert, W. Thin Films of Pd/Ni Alloys for Detection of High Hydrogen Concentrations. *J. Appl. Phys.* **1992**, *71*, 542−544.
(49) Offermans, P.; Tong, H.; Van Rijn, C.; Merken, P.; Brongersma, S.; Crego-Calama, M. Ultralow-Power Hydrogen Sensing with Single Palladium Nanowires. *Appl. Phys. Lett.* **2009**, *94*, 223110.
(50) Yu, S.; Welp, U.; Hua, L. Z.; Rydh, A.; Kwok, W. K.; Wang, H. H. Fabrication of Palladium Nanotubes and Their Application in Hydrogen Sensing. *Chem. Mater.* **2005**, *17*, 3445−3450.
(51) Lim, M. A.; Kim, D. H.; Park, C.-O.; Lee, Y. W.; Han, S. W.; Li, Z.; Williams, R. S.; Park, I. A New Route toward Ultrasensitive, Flexible Chemical Sensors: Metal Nanotubes by Wet-Chemical Synthesis Along Sacrificial Nanowire Templates. *ACS Nano* **2012**, *6*, 598−608.
(52) Zeng, X.-Q.; Wang, Y.-L.; Deng, H.; Latimer, M. L.; Xiao, Z.-L.; Pearson, J.; Xu, T.; Wang, H.-H.; Welp, U.; Crabtree, G. W.; et al. Networks of Ultrasmall Pd/Cr Nanowires as High Performance Hydrogen Sensors. *ACS Nano* **2011**, *5*, 7443−7452.
(53) Menke, E.; Thompson, M.; Xiang, C.; Yang, L.; Penner, R. Lithographically Patterned Nanowire Electrodeposition. *Nat. Mater.* **2006**, *5*, 914−919.
(54) Yang, F.; Taggart, D. K.; Penner, R. M. Joule Heating a Palladium Nanowire Sensor for Accelerated Response and Recovery to Hydrogen Gas. *Small* **2010**, *6*, 1422−1429.
(55) Grosse, K. L.; Bae, M.-H.; Lian, F.; Pop, E.; King, W. P. Nanoscale Joule Heating, Peltier Cooling and Current Crowding at Graphene−Metal Contacts. *Nat. Nanotechnol.* **2011**, *6*, 287−290.
(56) Perrin, N.; Budd, H. Photon Generation by Joule Heating in Metal Films. *Phys. Rev. Lett.* **1972**, *28*, 1701.
(57) Nyberg, C.; TengstÅl, C. Adsorption and Reaction of Water, Oxygen, and Hydrogen on Pd (100): Identification of Adsorbed Hydroxyl and Implications for the Catalytic H_2-O_2 Reaction. *J. Chem. Phys.* **1984**, *80*, 3463−3468.
(58) Gao, M.; Cho, M.; Han, H. J.; Jung, Y. S.; Park, I. Palladium-Decorated Silicon Nanomesh Fabricated by Nanosphere Lithography for High Performance, Room Temperature Hydrogen Sensing. *Small* **2018**, *14*, 1703691.
(59) Ahn, J.-H.; Yun, J.; Moon, D.-I.; Choi, Y.-K.; Park, I. Self-Heated Silicon Nanowires for High Performance Hydrogen Gas Detection. *Nanotechnology* **2015**, *26*, 095501.
(60) Hughes, R.; Schubert, W.; Zipperian, T.; Rodriguez, J.; Plut, T. Thin-Film Palladium and Silver Alloys and Layers for Metal-Insulator-Semiconductor Sensors. *J. Appl. Phys.* **1987**, *62*, 1074−1083.
(61) Jang, J.-S.; Qiao, S.; Choi, S.-J.; Jha, G.; Ogata, A. F.; Koo, W.-T.; Kim, D.-H.; Kim, I.-D.; Penner, R. M. Hollow Pd−Ag Composite Nanowires for Fast Responding and Transparent Hydrogen Sensors. *ACS Appl. Mater. Interfaces* **2017**, *9*, 39464−39474.
(62) Sonwane, C. G.; Wilcox, J.; Ma, Y. H. Achieving Optimum Hydrogen Permeability in PdAg and PdAu Alloys. *J. Chem. Phys.* **2006**, *125*, 184714.
(63) Alfonso, D. R.; Cugini, A. V.; Sholl, D. S. Density Functional Theory Studies of Sulfur Binding on Pd, Cu and Ag and Their Alloys. *Surf. Sci.* **2003**, *546*, 12−26.
(64) Johansson, M.; Ekedahl, L.-G. Hydrogen Adsorbed on Palladium during Water Formation Studied with Palladium Membranes. *Appl. Surf. Sci.* **2001**, *173*, 122−133.
(65) Fisher, G. B.; Gland, J. L. The Interaction of Water with the Pt (111) Surface. *Surf. Sci.* **1980**, *94*, 446−455.
(66) Ogle, K.; White, J.-M. The Low Temperature Water Formation Reaction on Pt (111): A Static SIMS and TDS Study. *Surf. Sci.* **1984**, *139*, 43−62.
(67) Jung, W. B.; Jang, S.; Cho, S. Y.; Jeon, H. J.; Jung, H. T. Recent Progress in Simple and Cost-Effective Top-Down Lithography for ≈10 nm Scale Nanopatterns: From Edge Lithography to Secondary Sputtering Lithography. *Adv. Mater.* **2020**, *32*, 1907101.
(68) Kobayashi, H.; Yamauchi, M.; Kitagawa, H.; Kubota, Y.; Kato, K.; Takata, M. Atomic-Level Pd−Pt Alloying and Largely Enhanced Hydrogen-Storage Capacity in Bimetallic Nanoparticles Reconstructed from Core/Shell Structure by a Process of Hydrogen Absorption/Desorption. *J. Am. Chem. Soc.* **2010**, *132*, 5576−5577.
(69) Huang, A.; Liu, Q.; Wang, N.; Zhu, Y.; Caro, J. Bicontinuous Zeolitic Imidazolate Framework ZIF-8@GO Membrane with Enhanced Hydrogen Selectivity. *J. Am. Chem. Soc.* **2014**, *136*, 14686−14689.
(70) Pan, Y.; Wang, B.; Lai, Z. Synthesis of Ceramic Hollow Fiber Supported Zeolitic Imidazolate Framework-8 (ZIF-8) Membranes with High Hydrogen Permeability. *J. Membr. Sci.* **2012**, *421*, 292−298.
(71) Kim, D.-H.; Kim, S.-J.; Shin, H.; Koo, W.-T.; Jang, J.-S.; Kang, J.-Y.; Jeong, Y. J.; Kim, I.-D. High-Resolution, Fast, and Shape-Conformable Hydrogen Sensor Platform: Polymer Nanofiber Yarn Coupled with Nanograined Pd@Pt. *ACS Nano* **2019**, *13*, 6071−6082.
(72) Wu, S.-H.; Qin, X.-H. Uniaxially Aligned Polyacrylonitrile Nanofiber Yarns Prepared by a Novel Modified Electrospinning Method. *Mater. Lett.* **2013**, *106*, 204−207.
(73) Gland, J. L.; Sexton, B. A.; Fisher, G. B. Oxygen Interactions with the Pt(111) Surface. *Surf. Sci.* **1980**, *95*, 587−602.
(74) Wißmann, P. The Electrical Resistivity of Pure and Gas Covered Metal Films; *Surface Physics*; Springer: Berlin, 1975; Vol. *77*, pp 1−96.
(75) Cho, S.-Y.; Ahn, H.; Park, K.; Choi, J.; Kang, H.; Jung, H.-T. Ultrasmall Grained Pd Nanopattern H_2 Sensor. *ACS Sens.* **2018**, *3*, 1876−1883.
(76) Hassan, K.; Chung, G.-S. Fast and Reversible Hydrogen Sensing Properties of Pd-Capped Mg Ultra-Thin Films Modified by Hydrophobic Alumina Substrates. *Sens. Actuators, B* **2017**, *242*, 450−460.
(77) Koo, W.-T.; Kim, Y.; Kim, S.; Suh, B. L.; Savagatrup, S.; Kim, J.; Lee, S.-J.; Swager, T. M.; Kim, I.-D. Hydrogen Sensors from Composites of Ultra-Small Bimetallic Nanoparticles and Porous Ion-Exchange Polymers. *Chem.* **2020**, DOI: 10.1016/j.chempr.2020.07.015.
(78) Yamazoe, N. New Approaches for Improving Semiconductor Gas Sensors. *Sens. Actuators, B* **1991**, *5*, 7−19.
(79) Luo, Y.; Zhang, C.; Zheng, B.; Geng, X.; Debliquy, M. Hydrogen Sensors Based on Noble Metal Doped Metal-Oxide Semiconductor: A Review. *Int. J. Hydrogen Energy* **2017**, *42*, 20386−20397.
(80) Jang, J.-S.; Lee, J.; Koo, W.-T.; Kim, D.-H.; Cho, H.-J.; Shin, H.; Kim, I.-D. Pore-Size-Tuned Graphene Oxide Membrane as a Selective Molecular Sieving Layer: Toward Ultraselective Chemiresistors. *Anal. Chem.* **2020**, *92*, 957−965.
(81) Aswal, D. K.; Gupta, S. K. *Science and Technology of Chemiresistor Gas Sensors*; Nova Science Publishers: New York, 2007.
(82) Conner, W. C.; Falconer, J. L. Spillover in Heterogeneous Catalysis. *Chem. Rev.* **1995**, *95*, 759−788.
(83) Li, Z.; Yan, S.; Wu, Z.; Li, H.; Wang, J.; Shen, W.; Wang, Z.; Fu, Y. Hydrogen Gas Sensor Based on Mesoporous In_2O_3 with Fast Response/Recovery and ppb Level Detection Limit. *Int. J. Hydrogen Energy* **2018**, *43*, 22746−22755.
(84) Chiang, Y.-J.; Li, K.-C.; Lin, Y.-C.; Pan, F.-M. A Mechanistic Study of Hydrogen Gas Sensing by PdO Nanoflake Thin Films at Temperatures below 250°C. *Phys. Chem. Chem. Phys.* **2015**, *17*, 3039−3049.
(85) Lee, Y. T.; Lee, J. M.; Kim, Y. J.; Joe, J. H.; Lee, W. Hydrogen Gas Sensing Properties of PdO Thin Films with Nano-Sized Cracks. *Nanotechnology* **2010**, *21*, 165503.

(86) Soleimanpour, A. M.; Khare, S. V.; Jayatissa, A. H. Enhancement of Hydrogen Gas Sensing of Nanocrystalline Nickel Oxide by Pulsed-Laser Irradiation. *ACS Appl. Mater. Interfaces* **2012**, *4*, 4651−4657.
(87) Steinebach, H.; Kannan, S.; Rieth, L.; Solzbacher, F. H_2 Gas Sensor Performance of NiO at High Temperatures in Gas Mixtures. *Sens. Actuators, B* **2010**, *151*, 162−168.
(88) Soleimanpour, A. M.; Jayatissa, A. H. Preparation of Nanocrystalline Nickel Oxide Thin Films by Sol−Gel Process for Hydrogen Sensor Applications. *Mater. Sci. Eng., C* **2012**, *32*, 2230−2234.
(89) Stamataki, M.; Tsamakis, D.; Brilis, N.; Fasaki, I.; Giannoudakos, A.; Kompitsas, M. Hydrogen Gas Sensors Based on PLD Grown NiO Thin Film Structures. *Phys. Status Solidi A* **2008**, *205*, 2064−2068.
(90) Nakate, U. T.; Ahmad, R.; Patil, P.; Yu, Y. T.; Hahn, Y.-B. Ultra Thin NiO Nanosheets for High Performance Hydrogen Gas Sensor Device. *Appl. Surf. Sci.* **2020**, *506*, 144971.
(91) Govindhan, M.; Sidhureddy, B.; Chen, A. High-Temperature Hydrogen Gas Sensor Based on Three-Dimensional Hierarchical-Nanostructured Nickel−Cobalt Oxide. *ACS Appl. Nano Mater.* **2018**, *1*, 6005−6014.
(92) Xiao, J.; Liu, P.; Liang, Y.; Li, H. B.; Yang, G. W. High Aspect Ratio β-MnO_2 Nanowires and Sensor Performance for Explosive Gases. *J. Appl. Phys.* **2013**, *114*, 073513.
(93) Tian, X.; Yang, L.; Qing, X.; Yu, K.; Wang, X. Trace Level Detection of Hydrogen Gas Using Birnessite-Type Manganese Oxide. *Sens. Actuators, B* **2015**, *207*, 34−42.
(94) Volanti, D. P.; Felix, A. A.; Orlandi, M. O.; Whitfield, G.; Yang, D.-J.; Longo, E.; Tuller, H. L.; Varela, J. A. The Role of Hierarchical Morphologies in the Superior Gas Sensing Performance of CuO-Based Chemiresistors. *Adv. Funct. Mater.* **2013**, *23*, 1759−1766.
(95) Lupan, O.; Postica, V.; Ababii, N.; Hoppe, M.; Cretu, V.; Tiginyanu, I.; Sontea, V.; Pauporté, T.; Viana, B.; Adelung, R. Influence of CuO Nanostructures Morphology on Hydrogen Gas Sensing Performances. *Microelectron. Eng.* **2016**, *164*, 63−70.
(96) Nakate, U. T.; Lee, G. H.; Ahmad, R.; Patil, P.; Hahn, Y.-B.; Yu, Y. T.; Suh, E.-k. Nano-Bitter Gourd Like Structured CuO for Enhanced Hydrogen Gas Sensor Application. *Int. J. Hydrogen Energy* **2018**, *43*, 22705−22714.
(97) Xu, H.; Fan, W.; Rosa, A.; Zhang, R.; Frauenheim, T. Hydrogen and Oxygen Adsorption on ZnO Nanowires: A First-Principles Study. *Phys. Rev. B: Condens. Matter Mater. Phys.* **2009**, *79*, 073402.
(98) Wang, C.; Zhou, G.; Li, J.; Yan, B.; Duan, W. Hydrogen-Induced Metallization of Zinc Oxide (2110) Surface and Nanowires: The Effect of Curvature. *Phys. Rev. B: Condens. Matter Mater. Phys.* **2008**, *77*, 245303.
(99) Varghese, O. K.; Gong, D.; Paulose, M.; Ong, K. G.; Grimes, C. A. Hydrogen Sensing Using Titania Nanotubes. *Sens. Actuators, B* **2003**, *93*, 338−344.
(100) Gu, H.; Wang, Z.; Hu, Y. Hydrogen Gas Sensors Based on Semiconductor Oxide Nanostructures. *Sensors* **2012**, *12*, 5517−5550.
(101) Xu, C.; Tamaki, J.; Miura, N.; Yamazoe, N. Grain Size Effects on Gas Sensitivity of Porous SnO_2-Based Elements. *Sens. Actuators, B* **1991**, *3*, 147−155.
(102) Rothschild, A.; Komem, Y. The Effect of Grain Size on the Sensitivity of Nanocrystalline Metal-Oxide Gas Sensors. *J. Appl. Phys.* **2004**, *95*, 6374−6380.
(103) Kwon, O. S.; Hong, J.-Y.; Park, S. J.; Jang, Y.; Jang, J. Resistive Gas Sensors Based on Precisely Size-Controlled Polypyrrole Nanoparticles: Effects of Particle Size and Deposition Method. *J. Phys. Chem. C* **2010**, *114*, 18874−18879.
(104) Roso, S.; Bittencourt, C.; Umek, P.; González, O.; Güell, F.; Urakawa, A.; Llobet, E. Synthesis of Single Crystalline In_2O_3 Octahedra for the Selective Detection of NO_2 and H_2 at Trace Levels. *J. Mater. Chem. C* **2016**, *4*, 9418−9427.
(105) Nakate, U. T.; Ahmad, R.; Patil, P.; Bhat, K. S.; Wang, Y.; Mahmoudi, T.; Yu, Y. T.; Suh, E.-k.; Hahn, Y.-B. High Response and Low Concentration Hydrogen Gas Sensing Properties Using Hollow ZnO Particles Transformed from Polystyrene@ZnO Core-Shell Structures. *Int. J. Hydrogen Energy* **2019**, *44*, 15677−15688.
(106) Zhu, L.; Zeng, W.; Li, Y. A Non-Oxygen Adsorption Mechanism for Hydrogen Detection of Nanostructured SnO_2 Based Sensors. *Mater. Res. Bull.* **2019**, *109*, 108−116.
(107) Ab Kadir, R.; Li, Z.; Sadek, A. Z.; Abdul Rani, R.; Zoolfakar, A. S.; Field, M. R.; Ou, J. Z.; Chrimes, A. F.; Kalantar-zadeh, K. Electrospun Granular Hollow SnO_2 Nanofibers Hydrogen Gas Sensors Operating at Low Temperatures. *J. Phys. Chem. C* **2014**, *118*, 3129−3139.
(108) Chuang, C.-C.; Prasannan, A.; Huang, B.-R.; Hong, P.-D.; Chiang, M.-Y. Simple Synthesis of Eco-Friendly Multifunctional Silk-Sericin Capped Zinc Oxide Nanorods and Their Potential for Fabrication of Hydrogen Sensors and UV Photodetectors. *ACS Sustainable Chem. Eng.* **2017**, *5*, 4002−4010.
(109) Lu, X.; Yin, L. Porous Indium Oxide Nanorods: Synthesis, Characterization and Gas Sensing Properties. *J. Mater. Sci. Technol.* **2011**, *27*, 680−684.
(110) Wang, B.; Zhu, L. F.; Yang, Y. H.; Xu, N. S.; Yang, G. W. Fabrication of a SnO_2 Nanowire Gas Sensor and Sensor Performance for Hydrogen. *J. Phys. Chem. C* **2008**, *112*, 6643−6647.
(111) Ra, H.-W.; Choi, K.-S.; Kim, J.-H.; Hahn, Y.-B.; Im, Y.-H. Fabrication of ZnO Nanowires Using Nanoscale Spacer Lithography for Gas Sensors. *Small* **2008**, *4*, 1105−1109.
(112) Qurashi, A.; El-Maghraby, E. M.; Yamazaki, T.; Kikuta, T. Catalyst Supported Growth of In_2O_3 Nanostructures and Their Hydrogen Gas Sensing Properties. *Sens. Actuators, B* **2010**, *147*, 48−54.
(113) Luo, X.; You, K.; Hu, Y.; Yang, S.; Pan, X.; Wang, Z.; Chen, W.; Gu, H. Rapid Hydrogen Sensing Response and Aging of α-MoO_3 Nanowires Paper Sensor. *Int. J. Hydrogen Energy* **2017**, *42*, 8399−8405.
(114) Lee, J.; Kim, D. H.; Hong, S.-H.; Jho, J. Y. A Hydrogen Gas Sensor Employing Vertically Aligned TiO_2 Nanotube Arrays Prepared by Template-Assisted Method. *Sens. Actuators, B* **2011**, *160*, 1494−1498.
(115) Chen, J.; Xu, L.; Li, W.; Gou, X. α-Fe_2O_3 Nanotubes in Gas Sensor and Lithium-Ion Battery Applications. *Adv. Mater.* **2005**, *17*, 582−586.
(116) Sinha, M.; Mahapatra, R.; Mondal, B.; Maruyama, T.; Ghosh, R. Ultrafast and Reversible Gas-Sensing Properties of ZnO Nanowire Arrays Grown by Hydrothermal Technique. *J. Phys. Chem. C* **2016**, *120*, 3019−3025.
(117) Ahmad, M. Z.; Kang, J. H.; Sadek, A. Z.; Moafi, A.; Sberveglieri, G.; Wlodarski, W. Synthesis of WO_3 Nanorod Based Thin Films for Ethanol and H_2 Sensing. *Procedia Eng.* **2012**, *47*, 358−361.
(118) Schneider, K.; Lubecka, M.; Czapla, A. V_2O_5 Thin Films for Gas Sensor Applications. *Sens. Actuators, B* **2016**, *236*, 970−977.
(119) Tonezzer, M.; Iannotta, S. H_2 Sensing Properties of Two-Dimensional Zinc Oxide Nanostructures. *Talanta* **2014**, *122*, 201−208.
(120) Zuruzi, A. S.; MacDonald, N. C.; Moskovits, M.; Kolmakov, A. Metal Oxide "Nanosponges" as Chemical Sensors: Highly Sensitive Detection of Hydrogen with Nanosponge Titania. *Angew. Chem., Int. Ed.* **2007**, *46*, 4298−4301.
(121) Liu, L.; Liu, C.; Li, S.; Wang, L.; Shan, H.; Zhang, X.; Guan, H.; Liu, Z. Honeycombed SnO_2 with Ultra Sensitive Properties to H_2. *Sens. Actuators, B* **2013**, *177*, 893−897.
(122) Zhang, Y.; Zeng, W.; Li, Y. NO_2 and H_2 Sensing Properties for Urchin-Like Hexagonal WO_3 Based on Experimental and First-Principle Investigations. *Ceram. Int.* **2019**, *45*, 6043−6050.
(123) Zhang, Y.; Zeng, W.; Li, Y. Theoretical and Experimental Investigations on H_2 Sensing Properties of Flower-Like Titanium Dioxide. *Mater. Res. Bull.* **2018**, *107*, 139−146.
(124) Qurashi, A.; Yamazaki, T.; El-Maghraby, E. M.; Kikuta, T. Fabrication and Gas Sensing Properties of In_2O_3 Nanopushpins. *Appl. Phys. Lett.* **2009**, *95*, 153109.

(125) Zhang, C.; Luo, Y.; Xu, J.; Debliquy, M. Room Temperature Conductive Type Metal Oxide Semiconductor Gas Sensors for NO_2 Detection. *Sens. Actuators, A* **2019**, *289*, 118−133.
(126) Xia, X.; Wu, W.; Wang, Z.; Bao, Y.; Huang, Z.; Gao, Y. A Hydrogen Sensor Based on Orientation Aligned TiO_2 Thin Films with Low Concentration Detecting Limit and Short Response Time. *Sens. Actuators, B* **2016**, *234*, 192−200.
(127) Fields, L. L.; Zheng, J. P.; Cheng, Y.; Xiong, P. Room-Temperature Low-Power Hydrogen Sensor Based on a Single Tin Dioxide Nanobelt. *Appl. Phys. Lett.* **2006**, *88*, 263102.
(128) Rout, C. S.; Kulkarni, G. U.; Rao, C. N. R. Room Temperature Hydrogen and Hydrocarbon Sensors Based on Single Nanowires of Metal Oxides. *J. Phys. D: Appl. Phys.* **2007**, *40*, 2777−2782.
(129) Haidry, A. A.; Xie, L.; Wang, Z.; Li, Z. Hydrogen Sensing and Adsorption Kinetics on Ordered Mesoporous Anatase TiO_2 Surface. *Appl. Surf. Sci.* **2020**, *500*, 144219.
(130) Mor, G. K.; Varghese, O. K.; Paulose, M.; Ong, K. G.; Grimes, C. A. Fabrication of Hydrogen Sensors with Transparent Titanium Oxide Nanotube-Array Thin Films as Sensing Elements. *Thin Solid Films* **2006**, *496*, 42−48.
(131) Wang, Y.-T.; Whang, W.-T.; Chen, C.-H. Hollow V_2O_5 Nanoassemblies for High-Performance Room-Temperature Hydrogen Sensors. *ACS Appl. Mater. Interfaces* **2015**, *7*, 8480−8487.
(132) Yang, S.; Wang, Z.; Hu, Y.; Luo, X.; Lei, J.; Zhou, D.; Fei, L.; Wang, Y.; Gu, H. Highly Responsive Room-Temperature Hydrogen Sensing of α-MoO_3 Nanoribbon Membranes. *ACS Appl. Mater. Interfaces* **2015**, *7*, 9247−9253.
(133) Kim, J.-H.; Mirzaei, A.; Kim, H. W.; Kim, S. S. Improving the Hydrogen Sensing Properties of SnO_2 Nanowire-Based Conductometric Sensors by Pd-Decoration. *Sens. Actuators, B* **2019**, *285*, 358−367.
(134) Sanger, A.; Kumar, A.; Kumar, A.; Chandra, R. Highly Sensitive and Selective Hydrogen Gas Sensor Using Sputtered Grown Pd Decorated MnO_2 Nanowalls. *Sens. Actuators, B* **2016**, *234*, 8−14.
(135) Cho, H.-J.; Chen, V. T.; Qiao, S.; Koo, W.-T.; Penner, R. M.; Kim, I.-D. Pt-Functionalized PdO Nanowires for Room Temperature Hydrogen Gas Sensors. *ACS Sens.* **2018**, *3*, 2152−2158.
(136) Mattoni, G.; de Jong, B.; Manca, N.; Tomellini, M.; Caviglia, A. D. Single-Crystal Pt-Decorated WO_3 Ultrathin Films: A Platform for Sub-ppm Hydrogen Sensing at Room Temperature. *ACS Appl. Nano Mater.* **2018**, *1*, 3446−3452.
(137) Lupan, O.; Cretu, V.; Postica, V.; Ahmadi, M.; Cuenya, B. R.; Chow, L.; Tiginyanu, I.; Viana, B.; Pauporté, T.; Adelung, R. Silver-Doped Zinc Oxide Single Nanowire Multifunctional Nanosensor with a Significant Enhancement in Response. *Sens. Actuators, B* **2016**, *223*, 893−903.
(138) Chava, R. K.; Oh, S.-Y.; Yu, Y.-T. Enhanced H_2 Gas Sensing Properties of Au@In_2O_3 Core−Shell Hybrid Metal−Semiconductor Heteronanostructures. *CrystEngComm* **2016**, *18*, 3655−3666.
(139) Choi, U.-S.; Sakai, G.; Shimanoe, K.; Yamazoe, N. Sensing Properties of Au-Loaded SnO_2−Co_3O_4 Composites to CO and H_2. *Sens. Actuators, B* **2005**, *107*, 397−401.
(140) Yamazoe, N.; Sakai, G.; Shimanoe, K. Oxide Semiconductor Gas Sensors. *Catal. Surv. Asia* **2003**, *7*, 63−75.
(141) Liu, C.; Kuang, Q.; Xie, Z.; Zheng, L. The Effect of Noble Metal (Au, Pd and Pt) Nanoparticles on the Gas Sensing Performance of SnO_2-Based Sensors: A Case Study on the {221} High-Index Faceted SnO_2 Octahedra. *CrystEngComm* **2015**, *17*, 6308−6313.
(142) Karim, W.; Spreafico, C.; Kleibert, A.; Gobrecht, J.; VandeVondele, J.; Ekinci, Y.; van Bokhoven, J. A. Catalyst Support Effects on Hydrogen Spillover. *Nature* **2017**, *541*, 68−71.
(143) Lupan, O.; Postica, V.; Hoppe, M.; Wolff, N.; Polonskyi, O.; Pauporté, T.; Viana, B.; Majérus, O.; Kienle, L.; Faupel, F.; et al. PdO/PdO_2 Functionalized ZnO: Pd Films for Lower Operating Temperature H_2 Gas Sensing. *Nanoscale* **2018**, *10*, 14107−14127.
(144) Wang, H.; Kang, B.; Ren, F.; Tien, L.; Sadik, P.; Norton, D.; Pearton, S.; Lin, J. Detection of Hydrogen at Room Temperature with Catalyst-Coated Multiple ZnO Nanorods. *Appl. Phys. A: Mater. Sci. Process.* **2005**, *81*, 1117−1119.
(145) Li, X. S.; Li, W. Z.; Chen, Y. X.; Wang, H. L. Enhancement of Hydrogen Spillover by Surface Labile Oxygen Species on Oxidized Pt/TiO_2 Catalyst. *Catal. Lett.* **1995**, *32*, 31−42.
(146) Tsang, S. C.; Bulpitt, C. D.; Mitchell, P. C.; Ramirez-Cuesta, A. J. Some New Insights into the Sensing Mechanism of Palladium Promoted Tin(iv) Oxide Sensor. *J. Phys. Chem. B* **2001**, *105*, 5737−5742.
(147) Liewhiran, C.; Tamaekong, N.; Wisitsoraat, A.; Tuantranont, A.; Phanichphant, S. Ultra-Sensitive H_2 Sensors Based on Flame-Spray-Made Pd-Loaded SnO_2 Sensing Films. *Sens. Actuators, B* **2013**, *176*, 893−905.
(148) Lee, S.; Lee, W. S.; Lee, J. K.; Hyun, S. K.; Lee, C.; Choi, S. Effects of Annealing Temperature on the H_2-Sensing Properties of Pd-Decorated WO_3 Nanorods. *Appl. Phys. A: Mater. Sci. Process.* **2018**, *124*, 232.
(149) Tang, Z.; Zhang, Y.; Deng, X.; Dai, Y.; Zhang, W.; Fan, F.; Qing, B.; Zhu, C.; Fan, J.; Shi, Y. The H_2 Sensing Properties of Facets-Dependent Pd Nanoparticles-Supported ZnO Nanorods. *Dalton Trans* **2018**, *47*, 15331−15337.
(150) Hwang, I.-S.; Choi, J.-K.; Woo, H.-S.; Kim, S.-J.; Jung, S.-Y.; Seong, T.-Y.; Kim, I.-D.; Lee, J.-H. Facile Control of C_2H_5OH Sensing Characteristics by Decorating Discrete Ag Nanoclusters on SnO_2 Nanowire Networks. *ACS Appl. Mater. Interfaces* **2011**, *3*, 3140−3145.
(151) Kolmakov, A.; Klenov, D.; Lilach, Y.; Stemmer, S.; Moskovits, M. Enhanced Gas Sensing by Individual SnO_2 Nanowires and Nanobelts Functionalized with Pd Catalyst Particles. *Nano Lett.* **2005**, *5*, 667−673.
(152) Inyawilert, K.; Wisitsoraat, A.; Liewhiran, C.; Tuantranont, A.; Phanichphant, S. H_2 Gas Sensor Based on PdO_x-Doped In_2O_3 Nanoparticles Synthesized by Flame Spray Pyrolysis. *Appl. Surf. Sci.* **2019**, *475*, 191−203.
(153) Wang, Z.; Li, Z.; Jiang, T.; Xu, X.; Wang, C. Ultrasensitive Hydrogen Sensor Based on Pd^0-Loaded SnO_2 Electrospun Nanofibers at Room Temperature. *ACS Appl. Mater. Interfaces* **2013**, *5*, 2013−2021.
(154) Choi, S.-J.; Chattopadhyay, S.; Kim, J. J.; Kim, S.-J.; Tuller, H. L.; Rutledge, G. C.; Kim, I.-D. Coaxial Electrospinning of WO_3 Nanotubes Functionalized with Bio-Inspired Pd Catalysts and Their Superior Hydrogen Sensing Performance. *Nanoscale* **2016**, *8*, 9159−9166.
(155) Heger, Z.; Skalickova, S.; Zitka, O.; Adam, V.; Kizek, R. Apoferritin Applications in Nanomedicine. *Nanomedicine* **2014**, *9*, 2233−2245.
(156) Kim, S. J.; Choi, S. J.; Jang, J. S.; Cho, H. J.; Koo, W. T.; Tuller, H. L.; Kim, I. D. Exceptional High-Performance of Pt-Based Bimetallic Catalysts for Exclusive Detection of Exhaled Biomarkers. *Adv. Mater.* **2017**, *29*, 1700737.
(157) Kim, S.-J.; Choi, S.-J.; Jang, J.-S.; Cho, H.-J.; Kim, I.-D. Innovative Nanosensor for Disease Diagnosis. *Acc. Chem. Res.* **2017**, *50*, 1587−1596.
(158) Kim, S.-J.; Choi, S.-J.; Jang, J.-S.; Kim, N.-H.; Hakim, M.; Tuller, H. L.; Kim, I.-D. Mesoporous WO_3 Nanofibers with Protein-Templated Nanoscale Catalysts for Detection of Trace Biomarkers in Exhaled Breath. *ACS Nano* **2016**, *10*, 5891−5899.
(159) Ahn, J.-H.; Yun, J.; Choi, Y.-K.; Park, I. Palladium Nanoparticle Decorated Silicon Nanowire Field-Effect Transistor with Side-Gates for Hydrogen Gas Detection. *Appl. Phys. Lett.* **2014**, *104*, 013508.
(160) Choi, S. J.; Choi, C.; Kim, S.-J.; Cho, H.-J.; Hakim, M.; Jeon, S.; Kim, I. D. Highly Efficient Electronic Sensitization of Non-Oxidized Graphene Flakes on Controlled Pore-Loaded WO_3 Nanofibers for Selective Detection of H_2S Molecules. *Sci. Rep.* **2015**, *5*, 8067.
(161) Zhang, Z.; Zou, X.; Xu, L.; Liao, L.; Liu, W.; Ho, J.; Xiao, X.; Jiang, C.; Li, J. Hydrogen Gas Sensor Based on Metal Oxide Nanoparticles Decorated Graphene Transistor. *Nanoscale* **2015**, *7*, 10078−10084.

(162) Wang, Y.; Liu, B.; Xiao, S.; Li, H.; Wang, L.; Cai, D.; Wang, D.; Liu, Y.; Li, Q.; Wang, T. High Performance and Negative Temperature Coefficient of Low Temperature Hydrogen Gas Sensors Using Palladium Decorated Tungsten Oxide. *J. Mater. Chem. A* **2015**, *3*, 1317−1324.
(163) Zhou, R.; Lin, X.; Xue, D.; Zong, F.; Zhang, J.; Duan, X.; Li, Q.; Wang, T. Enhanced H_2 Gas Sensing Properties by Pd-Loaded Urchin-Like $W_{18}O_{49}$ Hierarchical Nanostructures. *Sens. Actuators, B* **2018**, *260*, 900−907.
(164) Chang, C.-H.; Chou, T.-C.; Chen, W.-C.; Niu, J.-S.; Lin, K.-W.; Cheng, S.-Y.; Tsai, J.-H.; Liu, W.-C. Study of a WO_3 Thin Film Based Hydrogen Gas Sensor Decorated with Platinum Nanoparticles. *Sens. Actuators, B* **2020**, *317*, 128145.
(165) Zappa, D.; Galstyan, V.; Kaur, N.; Arachchige, H. M. M.; Sisman, O.; Comini, E. Metal Oxide-Based Heterostructures for Gas Sensors"- A Review. *Anal. Chim. Acta* **2018**, *1039*, 1−23.
(166) Esfandiar, A.; Irajizad, A.; Akhavan, O.; Ghasemi, S.; Gholami, M. R. Pd−WO_3/Reduced Graphene Oxide Hierarchical Nanostructures as Efficient Hydrogen Gas Sensors. *Int. J. Hydrogen Energy* **2014**, *39*, 8169−8179.
(167) Sun, Y.; Zhang, D.; Chang, H.; Zhang, Y. Fabrication of Palladium−Zinc Oxide−Reduced Graphene Oxide Hybrid for Hydrogen Gas Detection at Low Working Temperature. *J. Mater. Sci.: Mater. Electron.* **2017**, *28*, 1667−1673.
(168) Anand, K.; Singh, O.; Singh, M. P.; Kaur, J.; Singh, R. C. Hydrogen Sensor Based on Graphene/ZnO Nanocomposite. *Sens. Actuators, B* **2014**, *195*, 409−415.
(169) Bhangare, B.; Ramgir, N. S.; Pathak, A.; Sinju, K.; Debnath, A.; Jagtap, S.; Suzuki, N.; Muthe, K.; Terashima, C.; Aswal, D.; et al. Role of Sensitizers in Imparting the Selective Response of SnO_2/RGO Based Nanohybrids towards H_2S, NO_2 and H_2. *Mater. Sci. Semicond. Process.* **2020**, *105*, 104726.
(170) Bux, H.; Liang, F.; Li, Y.; Cravillon, J.; Wiebcke, M.; Caro, J. Zeolitic Imidazolate Framework Membrane with Molecular Sieving Properties by Microwave-Assisted Solvothermal Synthesis. *J. Am. Chem. Soc.* **2009**, *131*, 16000−16001.
(171) Shao, F.; Hoffmann, M. W.; Prades, J. D.; Zamani, R.; Arbiol, J.; Morante, J. R.; Varechkina, E.; Rumyantseva, M.; Gaskov, A.; Giebelhaus, I.; et al. Heterostructured p-CuO (Nanoparticle)/n-SnO_2 (Nanowire) Devices for Selective H_2S Detection. *Sens. Actuators, B* **2013**, *181*, 130−135.
(172) Khoang, N. D.; Trung, D. D.; Van Duy, N.; Hoa, N. D.; Van Hieu, N. Design of SnO_2/ZnO Hierarchical Nanostructures for Enhanced Ethanol Gas-Sensing Performance. *Sens. Actuators, B* **2012**, *174*, 594−601.
(173) Qin, Y.; Zhang, X.; Liu, Y.; Xie, W. Highly Aligned Array of $W_{18}O_{49}$/CuO Core−Shell Nanorods and Its Promising NO_2 Sensing Properties. *J. Alloys Compd.* **2016**, *673*, 364−371.
(174) Chen, A.; Huang, X.; Tong, Z.; Bai, S.; Luo, R.; Liu, C. C. Preparation, Characterization and Gas-Sensing Properties of SnO_2−In_2O_3 Nanocomposite Oxides. *Sens. Actuators, B* **2006**, *115*, 316−321.
(175) Chen, A.; Bai, S.; Shi, B.; Liu, Z.; Li, D.; Liu, C. C. Methane Gas-Sensing and Catalytic Oxidation Activity of SnO_2−In_2O_3 Nanocomposites Incorporating TiO_2. *Sens. Actuators, B* **2008**, *135*, 7−12.
(176) Bai, S.; Li, D.; Han, D.; Luo, R.; Chen, A.; Chung, C. L. Preparation, Characterization of WO_3−SnO_2 Nanocomposites and Their Sensing Properties for NO_2. *Sens. Actuators, B* **2010**, *150*, 749−755.
(177) Reddy, C. G.; Manorama, S. Room Temperature Hydrogen Sensor Based on SnO_2:La_2O_3. *J. Electrochem. Soc.* **2000**, *147*, 390.
(178) Shafiei, M.; Yu, J.; Chen, G.; Lai, P.; Motta, N.; Wlodarski, W.; Kalantar-zadeh, K. Improving the Hydrogen Gas Sensing Performance of Pt/MoO_3 Nanoplatelets Using a Nano Thick Layer of La_2O_3. *Sens. Actuators, B* **2013**, *187*, 267−273.
(179) Chaudhari, G.; Bende, A.; Bodade, A.; Patil, S.; Sapkal, V. Structural and Gas Sensing Properties of Nanocrystalline TiO_2:WO_3-Based Hydrogen Sensors. *Sens. Actuators, B* **2006**, *115*, 297−302.
(180) Park, W. J.; Choi, K. J.; Kim, M. H.; Koo, B. H.; Lee, J.-L.; Baik, J. M. Self-Assembled and Highly Selective Sensors Based on Air-Bridge-Structured Nanowire Junction Arrays. *ACS Appl. Mater. Interfaces* **2013**, *5*, 6802−6807.
(181) Choi, U.-S.; Sakai, G.; Shimanoe, K.; Yamazoe, N. Sensing Properties of SnO_2−Co_3O_4 Composites to CO and H_2. *Sens. Actuators, B* **2004**, *98*, 166−173.
(182) Shaposhnik, D.; Pavelko, R.; Llobet, E.; Gispert-Guirado, F.; Vilanova, X. Hydrogen Sensors on the Basis of SnO_2-TiO_2 Systems. *Procedia Eng.* **2011**, *25*, 1133−1136.
(183) Huang, H.; Gong, H.; Chow, C. L.; Guo, J.; White, T. J.; Tse, M. S.; Tan, O. K. Low-Temperature Growth of SnO_2 Nanorod Arrays and Tunable $n-p-n$ Sensing Response of a ZnO/SnO_2 Heterojunction for Exclusive Hydrogen Sensors. *Adv. Funct. Mater.* **2011**, *21*, 2680−2686.
(184) Katoch, A.; Kim, J.-H.; Kwon, Y. J.; Kim, H. W.; Kim, S. S. Bifunctional Sensing Mechanism of SnO_2−ZnO Composite Nanofibers for Drastically Enhancing the Sensing Behavior in H_2 Gas. *ACS Appl. Mater. Interfaces* **2015**, *7*, 11351−11358.
(185) Wang, Y.; Meyer, B.; Yin, X.; Kunat, M.; Langenberg, D.; Traeger, F.; Birkner, A.; Wöll, C. Hydrogen Induced Metallicity on the ZnO (1010) Surface. *Phys. Rev. Lett.* **2005**, *95*, 266104.
(186) Zheng, L.; Zheng, Y.; Chen, C.; Zhan, Y.; Lin, X.; Zheng, Q.; Wei, K.; Zhu, J. Network Structured SnO_2/ZnO Heterojunction Nanocatalyst with High Photocatalytic Activity. *Inorg. Chem.* **2009**, *48*, 1819−1825.
(187) Choi, S.-W.; Katoch, A.; Sun, G.-J.; Kim, J.-H.; Kim, S.-H.; Kim, S. S. Dual Functional Sensing Mechanism in SnO_2−ZnO Core−Shell Nanowires. *ACS Appl. Mater. Interfaces* **2014**, *6*, 8281−8287.
(188) Kathiravan, D.; Huang, B.-R.; Saravanan, A. Self-Assembled Hierarchical Interfaces of ZnO Nanotubes/Graphene Heterostructures for Efficient Room Temperature Hydrogen Sensors. *ACS Appl. Mater. Interfaces* **2017**, *9*, 12064−12072.
(189) Galstyan, V.; Ponzoni, A.; Kholmanov, I.; Natile, M. M.; Comini, E.; Nematov, S.; Sberveglieri, G. Reduced Graphene Oxide−TiO_2 Nanotube Composite: Comprehensive Study for Gas-Sensing Applications. *ACS Appl. Nano Mater.* **2018**, *1*, 7098−7105.
(190) Yang, S.; Wang, Z.; Zou, Y.; Luo, X.; Pan, X.; Zhang, X.; Hu, Y.; Chen, K.; Huang, Z.; Wang, S.; et al. Remarkably Accelerated Room-Temperature Hydrogen Sensing of MoO_3 Nanoribbon/Graphene Composites by Suppressing the Nanojunction Effects. *Sens. Actuators, B* **2017**, *248*, 160−168.
(191) Khan, M.; Tahir, M. N.; Adil, S. F.; Khan, H. U.; Siddiqui, M. R. H.; Al-warthan, A. A.; Tremel, W. Graphene Based Metal and Metal Oxide Nanocomposites: Synthesis, Properties and Their Applications. *J. Mater. Chem. A* **2015**, *3*, 18753−18808.
(192) Wang, T.; Huang, D.; Yang, Z.; Xu, S.; He, G.; Li, X.; Hu, N.; Yin, G.; He, D.; Zhang, L. A Review on Graphene-Based Gas/Vapor Sensors with Unique Properties and Potential Applications. *Nano-Micro Lett.* **2016**, *8*, 95−119.
(193) Zhang, Z.; Xue, Q.; Du, Y.; Ling, C.; Xing, W. Highly Enhanced Sensitivity of Hydrogen Sensors Using Novel Palladium-Decorated Graphene Nanoribbon Film/SiO_2/Si Structures. *J. Mater. Chem. A* **2014**, *2*, 15931−15937.
(194) Lu, G.; Hupp, J. T. Metal−Organic Frameworks as Sensors: A ZIF-8 Based Fabry−Pérot Device as a Selective Sensor for Chemical Vapors and Gases. *J. Am. Chem. Soc.* **2010**, *132*, 7832−7833.
(195) Liu, D.; Lu, K.; Poon, C.; Lin, W. Metal−Organic Frameworks as Sensory Materials and Imaging Agents. *Inorg. Chem.* **2014**, *53*, 1916−1924.
(196) Liu, Y.; Li, S.; Zhang, X.; Liu, H.; Qiu, J.; Li, Y.; Yeung, K. L. New Membrane Architecture: ZnO@ZIF-8 Mixed Matrix Membrane Exhibiting Superb H_2 Permselectivity and Excellent Stability. *Inorg. Chem. Commun.* **2014**, *48*, 77−80.
(197) Drobek, M.; Kim, J.-H.; Bechelany, M.; Vallicari, C.; Julbe, A.; Kim, S. S. MOF-Based Membrane Encapsulated ZnO Nanowires for Enhanced Gas Sensor Selectivity. *ACS Appl. Mater. Interfaces* **2016**, *8*, 8323−8328.

https://dx.doi.org/10.1021/acsnano.0c05307
ACS Nano 2020, 14, 14284−14322

(198) Ji, P.; Hu, X.; Tian, R.; Zheng, H.; Sun, J.; Zhang, W.; Peng, J. Atom-Economical Synthesis of ZnO@ZIF-8 Core−Shell Heterostructure by Dry Gel Conversion (DGC) Method for Enhanced H_2 Sensing Selectivity. *J. Mater. Chem. C* **2020**, *8*, 2927−2936.
(199) Wu, X.; Xiong, S.; Mao, Z.; Hu, S.; Long, X. A Designed ZnO@ ZIF-8 Core−Shell Nanorod Film as a Gas Sensor with Excellent Selectivity for H_2 over CO. *Chem. - Eur. J.* **2017**, *23*, 7969−7975.
(200) Deng, S.-Z.; Fan, H.-M.; Wang, M.; Zheng, M.-R.; Yi, J.-B.; Wu, R.-Q.; Tan, H.-R.; Sow, C.-H.; Ding, J.; Feng, Y.-P.; et al. Thiol-Capped ZnO Nanowire/Nanotube Arrays with Tunable Magnetic Properties at Room Temperature. *ACS Nano* **2010**, *4*, 495−505.
(201) Wang, J.; Li, X.; Xia, Y.; Komarneni, S.; Chen, H.; Xu, J.; Xiang, L.; Xie, D. Hierarchical Zno Nanosheet-Nanorod Architectures for Fabrication of Poly (3-Hexylthiophene)/ZnO Hybrid NO_2 Sensor. *ACS Appl. Mater. Interfaces* **2016**, *8*, 8600−8607.
(202) Vanheusden, K.; Seager, C.; Warren, W. t.; Tallant, D.; Voigt, J. Correlation between Photoluminescence and Oxygen Vacancies in ZnO Phosphors. *Appl. Phys. Lett.* **1996**, *68*, 403−405.
(203) Duan, J.; Higuchi, M.; Krishna, R.; Kiyonaga, T.; Tsutsumi, Y.; Sato, Y.; Kubota, Y.; Takata, M.; Kitagawa, S. High $CO_2/N_2/O_2/CO$ Separation in a Chemically Robust Porous Coordination Polymer with Low Binding Energy. *Chem. Sci.* **2014**, *5*, 660−666.
(204) Zhang, L.; Hu, Z.; Jiang, J. Sorption-Induced Structural Transition of Zeolitic Imidazolate Framework-8: A Hybrid Molecular Simulation Study. *J. Am. Chem. Soc.* **2013**, *135*, 3722−3728.
(205) Lin, R.-B.; Xiang, S.; Zhou, W.; Chen, B. Microporous Metal-Organic Framework Materials for Gas Separation. *Chem.* **2020**, *6*, 337−363.
(206) Huo, L.; Yang, X.; Liu, Z.; Tian, X.; Qi, T.; Wang, X.; Yu, K.; Sun, J.; Fan, M. Modulation of Potential Barrier Heights in Co_3O_4/SnO_2 Heterojunctions for Highly H_2-Selective Sensors. *Sens. Actuators, B* **2017**, *244*, 694−700.
(207) Dai, H. Carbon Nanotubes: Opportunities and Challenges. *Surf. Sci.* **2002**, *500*, 218−241.
(208) Llobet, E. Gas Sensors Using Carbon Nanomaterials: A Review. *Sens. Actuators, B* **2013**, *179*, 32−45.
(209) Chatterjee, S. G.; Chatterjee, S.; Ray, A. K.; Chakraborty, A. K. Graphene−Metal Oxide Nanohybrids for Toxic Gas Sensor: A Review. *Sens. Actuators, B* **2015**, *221*, 1170−1181.
(210) Toda, K.; Furue, R.; Hayami, S. Recent Progress in Applications of Graphene Oxide for Gas Sensing: A Review. *Anal. Chim. Acta* **2015**, *878*, 43−53.
(211) Kauffman, D. R.; Star, A. Carbon Nanotube Gas and Vapor Sensors. *Angew. Chem., Int. Ed.* **2008**, *47*, 6550−6570.
(212) Kong, J.; Chapline, M. G.; Dai, H. Functionalized Carbon Nanotubes for Molecular Hydrogen Sensors. *Adv. Mater.* **2001**, *13*, 1384−1386.
(213) Javey, A.; Guo, J.; Wang, Q.; Lundstrom, M.; Dai, H. Ballistic Carbon Nanotube Field-Effect Transistors. *Nature* **2003**, *424*, 654−657.
(214) Kumar, M. K.; Ramaprabhu, S. Nanostructured Pt Functionlized Multiwalled Carbon Nanotube Based Hydrogen Sensor. *J. Phys. Chem. B* **2006**, *110*, 11291−11298.
(215) Santangelo, S.; Faggio, G.; Messina, G.; Fazio, E.; Neri, F.; Neri, G. On the Hydrogen Sensing Mechanism of Pt/TiO_2/CNTs Based Devices. *Sens. Actuators, B* **2013**, *178*, 473−484.
(216) Liu, R.; Ding, H.; Lin, J.; Shen, F.; Cui, Z.; Zhang, T. Fabrication of Platinum-Decorated Single-Walled Carbon Nanotube Based Hydrogen Sensors by Aerosol Jet Printing. *Nanotechnology* **2012**, *23*, 505301.
(217) Jung, D.; Han, M.; Lee, G. S. Fast-Response Room Temperature Hydrogen Gas Sensors Using Platinum-Coated Spin-Capable Carbon Nanotubes. *ACS Appl. Mater. Interfaces* **2015**, *7*, 3050−3057.
(218) Mandelis, A.; Christofides, C. Interactions of Gases with Surfaces: The H_2 Cases. *Physics, Chemistry and Technology of Solid State Gas Sensor Devices*; John Wiley & Sons: Hoboken, NJ, 1993; Vol. *174*, pp 5−17.
(219) Sun, Y.; Wang, H. H. High-Performance, Flexible Hydrogen Sensors That Use Carbon Nanotubes Decorated with Palladium Nanoparticles. *Adv. Mater.* **2007**, *19*, 2818−2823.
(220) Sun, Y.; Wang, H. H. Electrodeposition of Pd Nanoparticles on Single-Walled Carbon Nanotubes for Flexible Hydrogen Sensors. *Appl. Phys. Lett.* **2007**, *90*, 213107.
(221) Mubeen, S.; Zhang, T.; Yoo, B.; Deshusses, M. A.; Myung, N. V. Palladium Nanoparticles Decorated Single-Walled Carbon Nanotube Hydrogen Sensor. *J. Phys. Chem. C* **2007**, *111*, 6321−6327.
(222) Rumiche, F.; Wang, H.; Indacochea, J. Development of a Fast-Response/High-Sensitivity Double Wall Carbon Nanotube Nanostructured Hydrogen Sensor. *Sens. Actuators, B* **2012**, *163*, 97−106.
(223) Li, X.; Le Thai, M.; Dutta, R. K.; Qiao, S.; Chandran, G. T.; Penner, R. M. Sub-6 nm Palladium Nanoparticles for Faster, More Sensitive H_2 Detection Using Carbon Nanotube Ropes. *ACS Sens.* **2017**, *2*, 282−289.
(224) Sayago, I.; Terrado, E.; Lafuente, E.; Horrillo, M.; Maser, W. K.; Benito, A.; Navarro, R.; Urriolabeitia, E.; Martinez, M.; Gutierrez, J. Hydrogen Sensors Based on Carbon Nanotubes Thin Films. *Synth. Met.* **2005**, *148*, 15−19.
(225) Khalap, V. R.; Sheps, T.; Kane, A. A.; Collins, P. G. Hydrogen Sensing and Sensitivity of Palladium-Decorated Single-Walled Carbon Nanotubes with Defects. *Nano Lett.* **2010**, *10*, 896−901.
(226) Pundt, A.; Kirchheim, R. Hydrogen in Metals: Microstructural Aspects. *Annu. Rev. Mater. Res.* **2006**, *36*, 555−608.
(227) Choi, B.; Lee, D.; Ahn, J.-H.; Yoon, J.; Lee, J.; Jeon, M.; Kim, D. M.; Kim, D. H.; Park, I.; Choi, Y.-K.; et al. Investigation of Optimal Hydrogen Sensing Performance in Semiconducting Carbon Nanotube Network Transistors with Palladium Electrodes. *Appl. Phys. Lett.* **2015**, *107*, 193108.
(228) Johnson, J. L.; Behnam, A.; Pearton, S.; Ural, A. Hydrogen Sensing Using Pd-Functionalized Multi-Layer Graphene Nanoribbon Networks. *Adv. Mater.* **2010**, *22*, 4877−4880.
(229) Chung, M. G.; Kim, D.-H.; Seo, D. K.; Kim, T.; Im, H. U.; Lee, H. M.; Yoo, J.-B.; Hong, S.-H.; Kang, T. J.; Kim, Y. H. Flexible Hydrogen Sensors Using Graphene with Palladium Nanoparticle Decoration. *Sens. Actuators, B* **2012**, *169*, 387−392.
(230) Hong, J.; Lee, S.; Seo, J.; Pyo, S.; Kim, J.; Lee, T. A Highly Sensitive Hydrogen Sensor with Gas Selectivity Using a Pmma Membrane-Coated Pd Nanoparticle/Single-Layer Graphene Hybrid. *ACS Appl. Mater. Interfaces* **2015**, *7*, 3554−3561.
(231) Tung, K.-L.; Lu, K.-T. Effect of Tacticity of PMMA on Gas Transport through Membranes: MD and MC Simulation Studies. *J. Membr. Sci.* **2006**, *272*, 37−49.
(232) Jeon, K.-J.; Moon, H. R.; Ruminski, A. M.; Jiang, B.; Kisielowski, C.; Bardhan, R.; Urban, J. J. Air-Stable Magnesium Nanocomposites Provide Rapid and High-Capacity Hydrogen Storage without Using Heavy-Metal Catalysts. *Nat. Mater.* **2011**, *10*, 286−290.
(233) Kaniyoor, A.; Jafri, R. I.; Arockiadoss, T.; Ramaprabhu, S. Nanostructured Pt Decorated Graphene and Multi Walled Carbon Nanotube Based Room Temperature Hydrogen Gas Sensor. *Nanoscale* **2009**, *1*, 382−386.
(234) Lu, X.; Song, X.; Gu, C.; Ren, H.; Sun, Y.; Huang, J. Freeze Drying-Assisted Synthesis of Pt@Reduced Graphene Oxide Nanocomposites as Excellent Hydrogen Sensor. *J. Phys. Chem. Solids* **2018**, *116*, 324−330.
(235) Kim, Y.; Choi, Y. S.; Park, S. Y.; Kim, T.; Hong, S.-P.; Lee, T. H.; Moon, C. W.; Lee, J.-H.; Lee, D.; Hong, B. H.; Jang, H. W. Au Decoration of a Graphene Microchannel for Self-Activated Chemoresistive Flexible Gas Sensors with Substantially Enhanced Response to Hydrogen. *Nanoscale* **2019**, *11*, 2966−2973.
(236) Wu, W.; Liu, Z.; Jauregui, L. A.; Yu, Q.; Pillai, R.; Cao, H.; Bao, J.; Chen, Y. P.; Pei, S.-S. Wafer-Scale Synthesis of Graphene by Chemical Vapor Deposition and Its Application in Hydrogen Sensing. *Sens. Actuators, B* **2010**, *150*, 296−300.
(237) Lange, U.; Hirsch, T.; Mirsky, V. M.; Wolfbeis, O. S. Hydrogen Sensor Based on a Graphene−Palladium Nanocomposite. *Electrochim. Acta* **2011**, *56*, 3707−3712.

https://dx.doi.org/10.1021/acsnano.0c05307
ACS Nano 2020, 14, 14284−14322

(238) Chhowalla, M.; Shin, H. S.; Eda, G.; Li, L.-J.; Loh, K. P.; Zhang, H. The Chemistry of Two-Dimensional Layered Transition Metal Dichalcogenide Nanosheets. *Nat. Chem.* **2013**, *5*, 263.

(239) Li, H.; Yin, Z.; He, Q.; Li, H.; Huang, X.; Lu, G.; Fam, D. W. H.; Tok, A. I. Y.; Zhang, Q.; Zhang, H. Fabrication of Single-and Multilayer MoS_2 Film-Based Field-Effect Transistors for Sensing NO at Room Temperature. *Small* **2012**, *8*, 63−67.

(240) Lee, K.; Gatensby, R.; McEvoy, N.; Hallam, T.; Duesberg, G. S. High-Performance Sensors Based on Molybdenum Disulfide Thin Films. *Adv. Mater.* **2013**, *25*, 6699−6702.

(241) Liu, B.; Chen, L.; Liu, G.; Abbas, A. N.; Fathi, M.; Zhou, C. High-Performance Chemical Sensing Using Schottky-Contacted Chemical Vapor Deposition Grown Monolayer MoS_2 Transistors. *ACS Nano* **2014**, *8*, 5304−5314.

(242) Late, D. J.; Doneux, T.; Bougouma, M. Single-Layer $MoSe_2$ Based NH_3 Gas Sensor. *Appl. Phys. Lett.* **2014**, *105*, 233103.

(243) Koo, W. T.; Cha, J. H.; Jung, J. W.; Choi, S. J.; Jang, J. S.; Kim, D. H.; Kim, I. D. Few-Layered WS_2 Nanoplates Confined in Co, N-Doped Hollow Carbon Nanocages: Abundant WS_2 Edges for Highly Sensitive Gas Sensors. *Adv. Funct. Mater.* **2018**, *28*, 1802575.

(244) Cha, J.-H.; Choi, S.-J.; Yu, S.; Kim, I.-D. 2d Ws 2-Edge Functionalized Multi-Channel Carbon Nanofibers: Effect of WS_2 Edge-Abundant Structure on Room Temperature NO_2 Sensing. *J. Mater. Chem. A* **2017**, *5*, 8725−8732.

(245) Ou, J. Z.; Ge, W.; Carey, B.; Daeneke, T.; Rotbart, A.; Shan, W.; Wang, Y.; Fu, Z.; Chrimes, A. F.; Wlodarski, W.; et al. Physisorption-Based Charge Transfer in Two-Dimensional SnS_2 for Selective and Reversible NO_2 Gas Sensing. *ACS Nano* **2015**, *9*, 10313−10323.

(246) Chen, H.; Chen, Y.; Zhang, H.; Zhang, D. W.; Zhou, P.; Huang, J. Suspended SnS_2 Layers by Light Assistance for Ultra-sensitive Ammonia Detection at Room Temperature. *Adv. Funct. Mater.* **2018**, *28*, 1801035.

(247) Agrawal, A.; Kumar, R.; Venkatesan, S.; Zakhidov, A.; Zhu, Z.; Bao, J.; Kumar, M.; Kumar, M. Fast Detection and Low Power Hydrogen Sensor Using Edge-Oriented Vertically Aligned 3-D Network of MoS_2 Flakes at Room Temperature. *Appl. Phys. Lett.* **2017**, *111*, 093102.

(248) Agrawal, A. V.; Kumar, R.; Yang, G.; Bao, J.; Kumar, M.; Kumar, M. Enhanced Adsorption Sites in Monolayer MoS_2 Pyramid Structures for Highly Sensitive and Fast Hydrogen Sensor. *Int. J. Hydrogen Energy* **2020**, *45*, 9268−9277.

(249) Baek, D.-H.; Kim, J. MoS_2 Gas Sensor Functionalized by Pd for the Detection of Hydrogen. *Sens. Actuators, B* **2017**, *250*, 686−691.

(250) Sarkar, D.; Xie, X.; Kang, J.; Zhang, H.; Liu, W.; Navarrete, J.; Moskovits, M.; Banerjee, K. Functionalization of Transition Metal Dichalcogenides with Metallic Nanoparticles: Implications for Doping and Gas-Sensing. *Nano Lett.* **2015**, *15*, 2852−2862.

(251) Murata, Y.; Nie, S.; Ebnonnasir, A.; Starodub, E.; Kappes, B.; McCarty, K.; Ciobanu, C.; Kodambaka, S. Growth Structure and Work Function of Bilayer Graphene on Pd (111). *Phys. Rev. B: Condens. Matter Mater. Phys.* **2012**, *85*, 205443.

(252) Lee, S. Y.; Kim, U. J.; Chung, J.; Nam, H.; Jeong, H. Y.; Han, G. H.; Kim, H.; Oh, H. M.; Lee, H.; Kim, H.; et al. Large Work Function Modulation of Monolayer MoS_2 by Ambient Gases. *ACS Nano* **2016**, *10*, 6100−6107.

(253) Khanuja, M.; Varandani, D.; Mehta, B. R. Pulse Like Hydrogen Sensing Response in Pd Nanoparticle Layers. *Appl. Phys. Lett.* **2007**, *91*, 253121.

(254) Kuru, C.; Choi, C.; Kargar, A.; Choi, D.; Kim, Y. J.; Liu, C. H.; Yavuz, S.; Jin, S. MoS_2 Nanosheet−Pd Nanoparticle Composite for Highly Sensitive Room Temperature Detection of Hydrogen. *Adv. Sci.* **2015**, *2*, 1500004.

(255) Hao, L.; Liu, Y.; Du, Y.; Chen, Z.; Han, Z.; Xu, Z.; Zhu, J. Highly Enhanced H_2 Sensing Performance of Few-Layer MoS_2/SiO_2/Si Heterojunctions by Surface Decoration of Pd Nanoparticles. *Nanoscale Res. Lett.* **2017**, *12*, 567.

(256) Hao, L.; Liu, H.; Xu, H.; Dong, S.; Du, Y.; Wu, Y.; Zeng, H.; Zhu, J.; Liu, Y. Flexible Pd-WS_2/Si Heterojunction Sensors for Highly Sensitive Detection of Hydrogen at Room Temperature. *Sens. Actuators, B* **2019**, *283*, 740−748.

(257) Zhang, D.; Sun, Y.; Jiang, C.; Zhang, Y. Room Temperature Hydrogen Gas Sensor Based on Palladium Decorated Tin Oxide/Molybdenum Disulfide Ternary Hybrid *via* Hydrothermal Route. *Sens. Actuators, B* **2017**, *242*, 15−24.

(258) Gottam, S. R.; Tsai, C.-T.; Wang, L.-W.; Wang, C.-T.; Lin, C.-C.; Chu, S.-Y. Highly Sensitive Hydrogen Gas Sensor Based on a MoS_2-Pt Nanoparticle Composite. *Appl. Surf. Sci.* **2020**, *506*, 144981.

(259) Huang, K.-C.; Wang, Y.-C.; Chen, P.-Y.; Lai, Y.-H.; Huang, J.-H.; Chen, Y.-H.; Dong, R.-X.; Chu, C.-W.; Lin, J.-J.; Ho, K.-C. High Performance Dye-Sensitized Solar Cells Based on Platinum Nano-particle/Multi-Wall Carbon Nanotube Counter Electrodes: The Role of Annealing. *J. Power Sources* **2012**, *203*, 274−281.

(260) Goel, N.; Kumar, R.; Jain, S. K.; Rajamani, S.; Roul, B.; Gupta, G.; Kumar, M.; Krupanidhi, S. A High-Performance Hydrogen Sensor Based on a Reverse-Biased MoS_2/GaN Heterojunction. *Nano-technology* **2019**, *30*, 314001.

(261) Kathiravan, D.; Huang, B.-R.; Saravanan, A.; Prasannan, A.; Hong, P.-D. Highly Enhanced Hydrogen Sensing Properties of Sericin-Induced Exfoliated MoS_2 Nanosheets at Room Temperature. *Sens. Actuators, B* **2019**, *279*, 138−147.

(262) Park, C. H.; Koo, W.-T.; Lee, Y. J.; Kim, Y.-H.; Lee, J.; Jang, J.-S.; Yun, H.; Kim, I.-D.; Kim, B. J. Hydrogen Sensors Based on MoS_2 Hollow Architectures Assembled by Pickering Emulsion. *ACS Nano* **2020**, *14*, 9652−9661.

(263) Zhu, C. R.; Gao, D.; Ding, J.; Chao, D.; Wang, J. Tmd-Based Highly Efficient Electrocatalysts Developed by Combined Computa-tional and Experimental Approaches. *Chem. Soc. Rev.* **2018**, *47*, 4332−4356.

(264) Naguib, M.; Kurtoglu, M.; Presser, V.; Lu, J.; Niu, J.; Heon, M.; Hultman, L.; Gogotsi, Y.; Barsoum, M. W. Two-Dimensional Nanocrystals Produced by Exfoliation of Ti_3AlC_2. *Adv. Mater.* **2011**, *23*, 4248−4253.

(265) Lukatskaya, M. R.; Mashtalir, O.; Ren, C. E.; Dall'Agnese, Y.; Rozier, P.; Taberna, P. L.; Naguib, M.; Simon, P.; Barsoum, M. W.; Gogotsi, Y. Cation Intercalation and High Volumetric Capacitance of Two-Dimensional Titanium Carbide. *Science* **2013**, *341*, 1502−1505.

(266) Gogotsi, Y.; Anasori, B. The Rise of MXenes. *ACS Nano* **2019**, *13*, 8491−8494.

(267) Kim, S. J.; Koh, H.-J.; Ren, C. E.; Kwon, O.; Maleski, K.; Cho, S.-Y.; Anasori, B.; Kim, C.-K.; Choi, Y.-K.; Kim, J.; Gogotsi, Y.; Jung, H.-T. Metallic $Ti_3C_2T_x$ MXene Gas Sensors with Ultrahigh Signal-to-Noise Ratio. *ACS Nano* **2018**, *12*, 986−993.

(268) Xiao, B.; Li, Y.-c.; Yu, X.-f.; Cheng, J.-B. MXenes: Reusable Materials for NH_3 Sensor or Capturer by Controlling the Charge Injection. *Sens. Actuators, B* **2016**, *235*, 103−109.

(269) Yu, X.-F.; Li, Y.-C.; Cheng, J.-B.; Liu, Z.-B.; Li, Q.-Z.; Li, W.-Z.; Yang, X.; Xiao, B. Monolayer Ti_2CO_2: A Promising Candidate for NH_3 Sensor or Capturer with High Sensitivity and Selectivity. *ACS Appl. Mater. Interfaces* **2015**, *7*, 13707−13713.

(270) Khazaei, M.; Ranjbar, A.; Arai, M.; Sasaki, T.; Yunoki, S. Electronic Properties and Applications of MXenes: A Theoretical Review. *J. Mater. Chem. C* **2017**, *5*, 2488−2503.

(271) Lee, E.; VahidMohammadi, A.; Prorok, B. C.; Yoon, Y. S.; Beidaghi, M.; Kim, D.-J. Room Temperature Gas Sensing of Two-Dimensional Titanium Carbide (MXene). *ACS Appl. Mater. Interfaces* **2017**, *9*, 37184−37190.

(272) Hermawan, A.; Zhang, B.; Taufik, A.; Asakura, Y.; Hasegawa, T.; Zhu, J.; Shi, P.; Yin, S. CuO Nanoparticles/$Ti_3C_2T_x$ MXene Hybrid Nanocomposites for Detection of Toluene Gas. *ACS Appl. Nano Mater.* **2020**, *3*, 4755−4766.

(273) Lee, E.; VahidMohammadi, A.; Yoon, Y. S.; Beidaghi, M.; Kim, D.-J. Two-Dimensional Vanadium Carbide MXene for Gas Sensors with Ultrahigh Sensitivity toward Nonpolar Gases. *ACS Sens.* **2019**, *4*, 1603−1611.

https://dx.doi.org/10.1021/acsnano.0c05307
ACS Nano 2020, 14, 14284−14322

(274) Zhu, Z.; Liu, C.; Jiang, F.; Liu, J.; Ma, X.; Liu, P.; Xu, J.; Wang, L.; Huang, R. Flexible and Lightweight $Ti_3C_2T_x$ MXene@Pd Colloidal Nanoclusters Paper Film as Novel H_2 Sensor. *J. Hazard. Mater.* **2020**, *399*, 123054.

(275) Xu, B.; Tian, Z.; Wang, J.; Han, H.; Lee, T.; Mei, Y. Stimuli-Responsive and On-Chip Nanomembrane Micro-Rolls for Enhanced Macroscopic Visual Hydrogen Detection. *Sci. Adv.* **2018**, *4*, eaap8203.

(276) Cendula, P.; Kiravittaya, S.; Mei, Y.; Deneke, C.; Schmidt, O. Bending and Wrinkling as Competing Relaxation Pathways for Strained Free-Hanging Films. *Phys. Rev. B: Condens. Matter Mater. Phys.* **2009**, *79*, 085429.

(277) Nikishkov, G. P. Curvature Estimation for Multilayer Hinged Structures with Initial Strains. *J. Appl. Phys.* **2003**, *94*, 5333−5336.

(278) Chen, Z.; Huang, G.; Trase, I.; Han, X.; Mei, Y. Mechanical Self-Assembly of a Strain-Engineered Flexible Layer: Wrinkling, Rolling, and Twisting. *Phys. Rev. Appl.* **2016**, *5*, 017001.

(279) Nugroho, F. A.; Darmadi, I.; Cusinato, L.; Susarrey-Arce, A.; Schreuders, H.; Bannenberg, L. J.; da Silva Fanta, A. B.; Kadkhodazadeh, S.; Wagner, J. B.; Antosiewicz, T. J.; et al. Metal−Polymer Hybrid Nanomaterials for Plasmonic Ultrafast Hydrogen Detection. *Nat. Mater.* **2019**, *18*, 489−495.

(280) Luo, S.; Wang, D.; Flanagan, T. B. Thermodynamics of Hydrogen in fcc Pd−Au Alloys. *J. Phys. Chem. B* **2010**, *114*, 6117−6125.

(281) Nugroho, F. A.; Iandolo, B.; Wagner, J. B.; Langhammer, C. Bottom-Up Nanofabrication of Supported Noble Metal Alloy Nanoparticle Arrays for Plasmonics. *ACS Nano* **2016**, *10*, 2871−2879.

(282) Ngene, P.; Westerwaal, R. J.; Sachdeva, S.; Haije, W.; de Smet, L. C.; Dam, B. Polymer-Induced Surface Modifications of Pd-Based Thin Films Leading to Improved Kinetics in Hydrogen Sensing and Energy Storage Applications. *Angew. Chem., Int. Ed.* **2014**, *53*, 12081−12085.

(283) Katoch, A.; Choi, S.-W.; Kim, H. W.; Kim, S. S. Highly Sensitive and Selective H_2 Sensing by ZnO Nanofibers and the Underlying Sensing Mechanism. *J. Hazard. Mater.* **2015**, *286*, 229−235.

(284) Yoo, I.-H.; Kalanur, S. S.; Seo, H. Deposition of Pd Nanoparticles on MWCNTs: Green Approach and Application to Hydrogen Sensing. *J. Alloys Compd.* **2019**, *788*, 936−943.

https://dx.doi.org/10.1021/acsnano.0c05307
ACS Nano 2020, 14, 14284−14322